Chemical Characterization of Native and Extracted Pectins with Confocal Raman Microspectroscopy

MASTER THESIS

in Partial Fulfillment of the Requirements for the Degree

Master of Science   and   Magistr

in the Master's Study

Joint Master Program Biological Chemistry

Author:
Sophie Füchtner

Submission:
Institute of Polymer Science, JKU

Supervisor:
Univ.-Prof. Dr^{in} Sabine Hild

Linz, February 2016

Declaration

I hereby declare under oath that the submitted Master thesis has been written solely by me without any third-party assistance, information other than provided sources or aids have not been used and those used have been fully documented. Sources for literal, paraphrased and cited quotes have been accurately credited. The submitted document here present is identical to the electronically submitted text document

I hereby declare that, in accordance with Article 47b of Act No. 111/1998 in the valid wording, I agree with the publication of my master, in full / in shortened form resulting from deletion of indicated parts to be kept in the Faculty of Science archive, in electronic form in publicly accessible part of the STAG database operated by the University of South Bohemia in České Budějovice accessible through its web pages.

Further, I agree to the electronic publication of the comments of my supervisor and thesis opponents and the record of the proceedings and results of the thesis defence in accordance with aforementioned Act No. 111/1998. I also agree to the comparison of the text of my thesis with the Theses.cz thesis database operated by the National Registry of University Theses and a plagerism detection system.

Eidesstattliche Erklärung

Ich erkläre an Eides statt, dass ich die vorliegende Masterarbeit selbstständig und ohne fremde Hilfe verfasst, andere als die angegebenen Quellen und Hilfsmittel nicht benutzt bzw. die wörtlich oder sinngemäß entnommenen Stellen als solche kenntlich gemacht habe. Die vorliegende Arbeit ist mit dem elektronisch übermittelten Textdokument identisch.

Linz on February 14, 2016

....
Sophie Füchtner

Acknowledgement

Contents

List of Figures

List of Tables

List of Abbreviations and Symbols

α molecular polarizability

$\bar{\nu}$ wavenumber in cm^{-1}

δ bending vibrational mode

δ_{ip} in-plane bending vibration

δ_{oop} out-of-plane bending vibration

λ wavelength

μ contextually reduced mass of two atoms or dipole moment

ν contextually stretching vibrational mode or quantum mechanical vibronic level

ν_{as} asymmetric stretching mode

ν_s symmetrical stretching mode

E electric field

I_0 intensity of incident light

'fingerprint region'   the term is incorrectly used as the spectral range of 300-1800 rel. 1/cm

E_{pot} potential Energy

c speed of light in vacuum

h Planck's constant - 6.6256×10^{-27} erg sec

k force constant of an atomic bond

v classical vibrational frequency

x internuclear distance

CH vibrations   spectral range 2750-3050 rel. 1/cm

DB   Degree of Blockiness

DE   Degree of Esterification

DF   Degrees of Freedom

DM   Degree of Methoxylation

g/mm   grooves per millimeter

GalA   Galacturonic Acid

HG   HomoGalacturonan

HM(P)   High Methoxyl (Pectin)

IR   InfraRed

KMCA   K-Means Cluster Analysis

LM(P)   Low Methoxyl (Pectin)

PCR   Principal Component Analysis

PCs   Principal Components

PGA   PolyGalacturonic Acid

PME   Pectin-Methyl-Esterase

Poly x,y   Polynomial of order x and noise threshold y

PSFs   Point Spread Functions

Q   normal coordinate

RG I   RhamnoGalacturonan I

RG II   RhamnoGalacturonan II

sh   shoulder

Abstract

The properties of plant cell walls are mainly determined by the local modifications of the individual materials constituting it. Pectin is a complex polysaccharide, capable of gel formation and the major component of lily pollen tubes. Pectin can be methyl-esterified to different degrees, changing its mechanical properties. A key point to deduce the mechanisms underlying the growth process is to investigate the spatial distribution of the methoxyl groups along the cell wall. Using Confocal Raman Microspectroscopy, the pollen tubes of *Lilium longiflorum* were imaged in the hydrated state. As a model to understand the spectral signatures, extracted pectins of different degrees of methoxylation, in solution and cross-linking were used. K-Means Cluster Analysis (KMCA) differentiated vesicles and cell wall, but not the tip and the shaft. Spectral differences were found between all different compartments, especially regarding the water content and the intensity of the C-H stretchings, which were also confirmed with Principal Component Analysis (PCA). The spectra of the extracted pectins did not prove to be a straightforward indicator for the state of the pectin in the pollen tubes, but the cross-linking experiments revealed interesting changes, relating to the pollen. Although the results showed that native and extracted pectins do show spectral differences, more detailed calibration series of extracted pectins in combination with chemometric analysis and modelling tools could provide a good system for more in depth investigations.

Chapter 1 – Introduction

During the germination process of *Lilium longiflorum* pollen, long tubes are formed by the pollen cell. The cell wall of the tube mainly consists of pectin, especially at the tip. This complex polysaccharide is integrated into the wall at the tip of the tube, where it is delivered by vesicles in its methyl-esterified form. During the growth process, enzymes de-methoxylate pectin, allowing for complexation with mainly calcium ions, which leads to gel formation. This process alters the rheological properties of the cell wall and thus strongly influences the growth process. The exact mechanism of growth is yet unclear, but arguably the chemical background of the physical properties of the cell wall play an important role [4, 22, 35, 36, 65, 66, and others].

Using Raman spectroscopy and a confocal microscope setup in combination, the molecular composition and distribution of matter can be monitored with high spatial resolution. The characteristic spectral signature that each molecule has, provides a mean to discriminate many different substances and their derivatives. It has been shown in several studies that also biological samples like plant tissue can be analyzed *in situ* in a non-destructive way and the distribution of the various materials constituting it monitored. Hence, confocal Raman microspectroscopy can be used as a tool to the better understanding of the structural organization of plant tissues, i.e. lily pollen tubes [19–21, 43].

In order to understand the spectral signatures of the pollen tubes, extracted pectins with different degrees of esterification and cross-linking have potential to serve as a model system. This can be done because the Raman signal is proportional to the abundance of a molecule, and can thus be used in a (semi-)quantitative way. Furthermore, small changes in chemical structure and orientation can be detected and quantified [43, 57, 64]. This is generally handy for the implementation of (confocal) Raman microscopy in basic science, but also in industrial quality assurance, which can be another application for pectin, also having industrial applications, such as gelling agent for jam, but also in biomedical science as a gel. No matter the ultimate application, using appropriate algorithms even very complex spectra, as those arising from biological samples like pectin, can be analyzed.

The aim of this thesis was to assert whether and how it is possible to record high resolution images of the lily pollen tubes in the hydrated state. In order to identify signals informative about the state of the pectin in the pollen tube, spectra of extracted pectin of various degrees of methoxylation and in the calcium cross-linked state should be recorded. Finally, the spectral signatures of native and extracted pectin should be compared using appropriate analysis tools.

This thesis can thus be divided into three main parts, namely the imaging of lily pollen tubes, investigation of the extracted pectins and the analysis of the data.

For the lily pollen following tasks should be fulfilled:

1. Germinate the pollen of *Lilium longiflorum* in nutrient solution in order to promote tip growth.

2. Shock the pollen osmotically to stop them from growing, to make imaging possible.

3. Imaging of the tip of pollen tubes under .

4. Analyze the images to find differences in the composition of the apex (the tip) and the subapex (the side) and other eventually occurring compartments.

The second big part of the thesis involved the extracted pectins and following aims were set:

1. Dissolve pectins with different degrees of esterification, extraction sources and concentrations.

2. Prepare pectin gels with different calcium concentrations.

3. Record Raman spectra of the latter two.

4. Analyze the data to find differences between the spectra at different concentrations, but also pectin sources and degrees of esterification if possible, as well as changes occurring upon crosslinking.

Last but not least, the data analysis required finding a chain of calculations that would allow the answering of the above questions. This involves methods for the correction of the background and noise reduction. Pre-selection of data in the case of the extracted pectins, and the use of multivariate analysis tools for clustering of the pollen images (k-means cluster analysis) and basic exploratory data analysis (principal component analysis).

1.1 Pollen Tubes of Lilium

Plant cells, as opposed to animal cells, have a primary cell wall built around their cell membranes. The cell wall of higher plants mainly consists of cellulose, hemicellulose and pectin and provides stability to prevent the membrane's bursting under load, communication with surrounding cells, and contributes to the growth process of the plant by expanding into the right direction and rate [27]. Thus it is a crucial player in the plants shape and structure [28]. The expansion of the cell wall is driven either by turgor pressure or mechanically by modification of the cell wall constituents [28]. The rheological properties of the cell wall, especially during growth, are very interesting for material
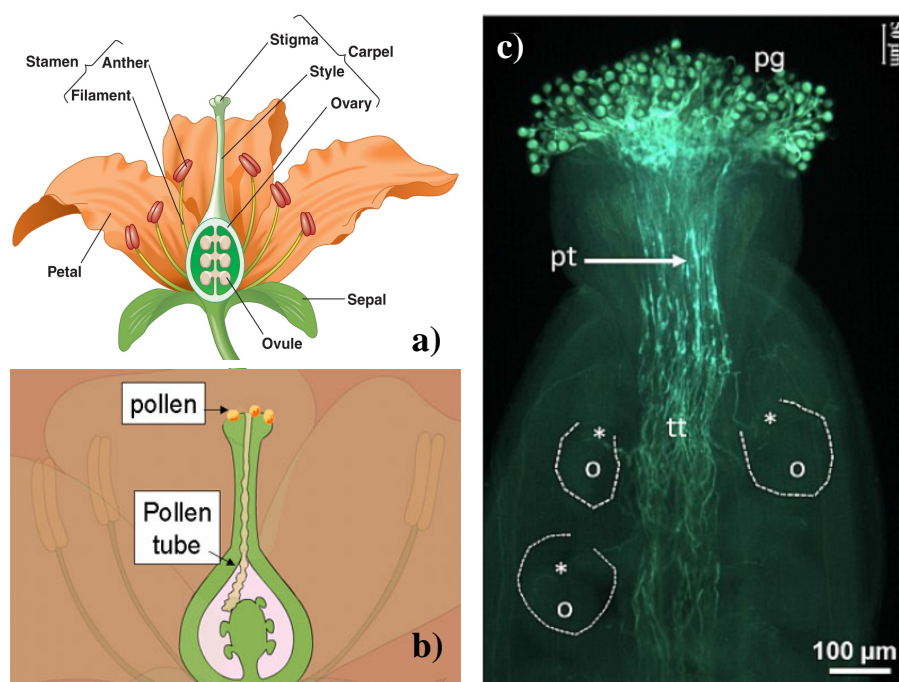
Figure 1.1: a) Schematic representation of the anatomy of a lily flower, extracted from [7]. **b)** Zoom on pistil and ovary of a flower and a growing pollen tube [26]. **c)** Fluorescence micrograph of a pollinated *Arabidopsis thaliana*. The pollen grains (pg) are visible on top, the pollen tubes (pt) grow through the transmitting tract (tt) to the outlined ovaries (o) - dashed line [36].

science, and hence a lot of research is done to find out how and where the polymers constituting the wall are modified i.e. in chemical terms, as well as how this is best detected [27, 28, 48].

A good model system to study the cell wall dynamics during a growth process is a germinating pollen. Angiosperms (flowering plants) and gymnosperms (conifers) have developed a sophisticated mechanism to ensure fertilization - pollen tube growth. Upon pollination, the pollen of an angiosperm, like lilies are, adheres to the stigma of a flower. If it is a compatible flower, the pollen is re-hydrated and starts to germinate. It grows a tube that penetrates the stigma and grows down the style to reach the ovaries, where it delivers two sperm cells to one of the ovules by exploding at the tip [47]. In lilies the stigma is wet and the style hollow, while in other plants, like *Arabidopsis thaliana*, the stigma is dry and the style solid. In lilies the transmitting tract of the hollow style is filled with gas and the specialized stylar cells guide the pollen tube to the ovule by molecular signals [36, 65].

For successful fertilization, a pollen tube must accomplish following tasks: it must grow fast and under potentially variable micro-environmental conditions to out-compete other pollen [24, 65]. Thus, polar elongation must be held up requiring a delicate balance between elongation and material delivery, while steadily reorienting the growth direction (following the chemical gradients), in order to find the shortest way to the ovule [65]. This implies mechanisms to sense the gradients and to react accordingly. The pollen tube cell wall must, furthermore, protect the sperm cells until delivery and resist to the tensile stresses exerted by turgor pressure inside the cell to prevent premature bursting.
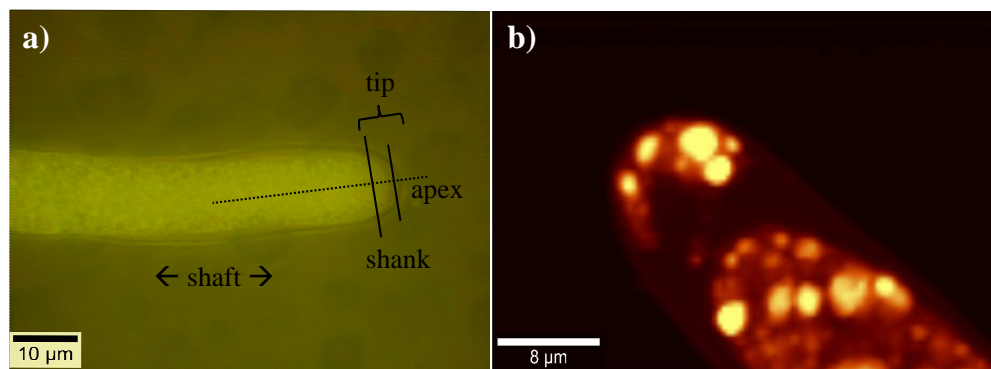
Figure 1.2: a) Bright field photgraph of a lily pollen tube with labeled regions - the shaft and the tip comprised of shank and apex. The dashed line represents the axis of symmetry. **b)** Raman image of a germinated lily pollen tube generated from the CH vibrations. The bright circles are vesicles being transported to the membrane. At the apex they are integrated.

The polymeric cell wall of the pollen is also crucial for the shape of the cell [36].

Pollen cells are tip growing cells, as are root hair, fungal hyphae and some algae [35] and expansion happens only at the apex of the pollen tube. It has thus to be plastic enough at the tip to allow expansion, but be rigid at the shaft to prevent bursting (see Fig. 1.2a). New wall material is delivered by actin-myosin transport [35] through the tube while packed inside of vesicles originating from the Golgi apparatus [36]. Figure1.2b) shows this process via a Raman image (CH vibrations) of an osmotically shocked pollen tube. Exocytosis of the vesicles provides the material needed for the expansion of plasma membrane and the cell wall [35, 44, 65]. Also, a calcium gradient is maintained, increasing towards the tip [44]. The tubes have an approximate diameter of 10 μm [47] and a wall thickness around 1 μm. The growth rate of pollen tubes can be steady or oscillatory, with rates around 12 μm min^{-1} in *Lilium longiflorum* [24], but able to show over 6-fold rate changes within 10 - 25 s during oscillatory growth [65]. The mean turgor pressure in *Lilium longiflorum* was assessed to be 0.21 MPa [65], which roughly corresponds to up to two times the atmospheric pressure.

Up to now, it is not known what exact mechanisms underlie these remarkable properties of pollen tubes, namely fast and stable growth. It requires the temporal and quantitative coordination of many complex processes: from sensing extracellular signals, to gene activation, protein, lipid and saccharide synthesis, to vesicle transport, membrane and cell wall integration and expansion, including enzyme regulation [4, 28, 36, 46, 49, 65, a.o.]. Although it is recognized that the cell wall expansion is a turgor driven process, given its constancy, the mechanical properties of the cell wall, and therefore its chemical composition, must be one of the keys to the observed growth patterns [28, 44, 65].

Pollen tubes, with their tip-polarized growth, provide a good model system for investigation of the distribution and changes of different cell wall materials in higher plants [49]. Additionally, pollen are

isolated, unadhered cells that can easily be germinated *in vitro* [35].

1.1.1 The cell wall of pollen tubes

The polymers making up the pollen tube wall are almost exclusively polysaccharides. Cellulose $[\beta\text{-(1,4')-D-glucose}]_n$, although present in low concentrations, is present in the whole tube and is an important stabilizer of the tip by supporting the flanking regions of the apex with its microfibrilar structure [16, 27]. According to Mollet et al. [36] it is only weakly detected at the tip, controversially other authors have shown otherwise [16]. Callose ($\beta\text{-(1,3')-D-glucose}$) is found in the cell wall and in callose plugs, which keep the tube cell, containing the DNA, in the apical region of the growing pollen tube. Callose is the major component of the rear shaft and controls the pore size of the wall [16, 36, 49]. The hemicellulose type Xyloglucan is another important component of the shaft's wall, contributing to its rigidity together with the above mentioned glucans [36].

These materials are embedded in what seems to be the key component in the dynamic growth process - a pectin network. Pectin, or rather pectic substances, are a multidomain polysaccharide exhibiting compositional and structural variations between and within species, tissues and developmental stages of the plant [22, 28, 49]. It is found throughout the pollen tube, but is the main cell wall polymer present at the apex of the pollen tube. The characteristic feature of pectin is the backbone composed of $\alpha\text{-(1,4')}$-linked D-galacturonic acid residues, short Polygalacturonic acid (PGA), that can be methyl-esterified to various degrees [27] on the C-6 position [38]. Free carboxylic acid units provide a binding site for calcium ions, resulting in cross-linking and gel formation of pectin, which in turn renders the material more rigid and resistant to load (see section 1.2).

It has been shown that pectin is integrated at the tip in its strongly methyl-esterified form, while it is gradually de-methoxylated towards the shank by the membrane-bound enzyme pectin-methyl-esterase (PME) [4, 16, 44]. This reaction releases protons and methanol [4]. There are several iso-forms of PME which are differentially expressed and are regulated by different mechanisms (see [4] or [36] for a review). A known feature of PMEs is block-wise versus nonblock-wise de-methoxylation, which affects the gelling properties of pectin. For instance, the affinity for Ca^{2+} ions increases with the number of consecutive binding sites, as well as the resulting mechanical properties, like swelling behavior and plasticity [32, 39, 40, 55, 69]. There are of course several other pectin-modifying/ -degrading enzymes, but these are not relevant here and can be reviewed in [36] and others. The chemical and macromolecular structure, as well as other properties of pectin will be discussed in the next section.

1.2   Pectin - Properties and Uses

As already mentioned in the previous chapter, pectin shows several interesting physical properties, that can at least partly be derived from its chemical structure. In order to understand how this properties arise, the study of the structure and patterns found in pectin are of great importance and often extracted pectins, with defined chemical properties are used as a model. Nevertheless, one should be aware that the properties of native pectins cannot be directly inferred from findings from extracted pectins. This is due to unknown parameters of native pectin like for example the nature and amount of covalent cross-links [49].

1.2.1   Structure and Chemical Properties

Pectin, as mentioned earlier, is a very complex molecule. Not only does native pectin consist of many different monosaccharides, but it also is a poldisperse substance [56]. The PGA domain described in the previous section is termed the homogalacturonan (HG) and builds the linear backbone for a number of covalent modifications and ramifications. In addition to methoxylation on C-6, the PGA subunits can also be acetylated on O-2 and/or O-3 positions [49], although the role of this modification has not been investigated in depth. The degree of acetylation (DA) can also be defined[36]. In native pectins the most abundant domain (besides HG) is the Rhamnogalacturonan I (RG I), which has a backbone of alternating rhamnose and galacturonic acid units ([1,4-α-D-GalpA-1,2-α-1-Rhap-]$_n$= [38], to which the neutral sugars arabinose and galactose are attached [27, 49]. Another domain, the Rhamnogalacturonan II (RG II), is a very conserved structure throughout the plant kingdom [36, 49] and has a PGA backbone like the HG, but with side chains constructed from 12 different glycosyl residues, some of which are very rare, like xylofuranose and aceric acid [22, 49]. At least 22 different glycosidic linkages are known for RG II [22]. RG II has the ability to bind borate ions, but the role of this type of cross-link is not clear to date [22, 49]. RG I and II, together with the arabinan and arabinogalactan (I & II) domains, comprise the hairy regions of a pectic molecule. Other segments are comprised of the xylogalacturonan and the apiogalacturonan which are part of the smooth regions together with the HG [49]. One pectin unit can contain up to 1000 monosaccharides, corresponding to a molecular weight of 50 - 200 kDa [49, 56].

The situation looks quite different for extracted pectin [49, 56]. Depending on the source and method of extraction, the degree of esterification and chain length can be altered [38]. Also, a significant part of the neutral sugars is lost during extraction. For the same reason the galacturonic acid content is higher than in native pectin and can constitute up to 70 % w/w [49]. Typical raw materials for extraction of pectin are apple pomace and citrus peel from the juice and cider industry. Hot, acidic or basic water extraction are the most prominent methods of extraction. Other industrially applied methods include the use of chelating agents, extracting the calcium from pectin, or enzymatic digestion, rup-
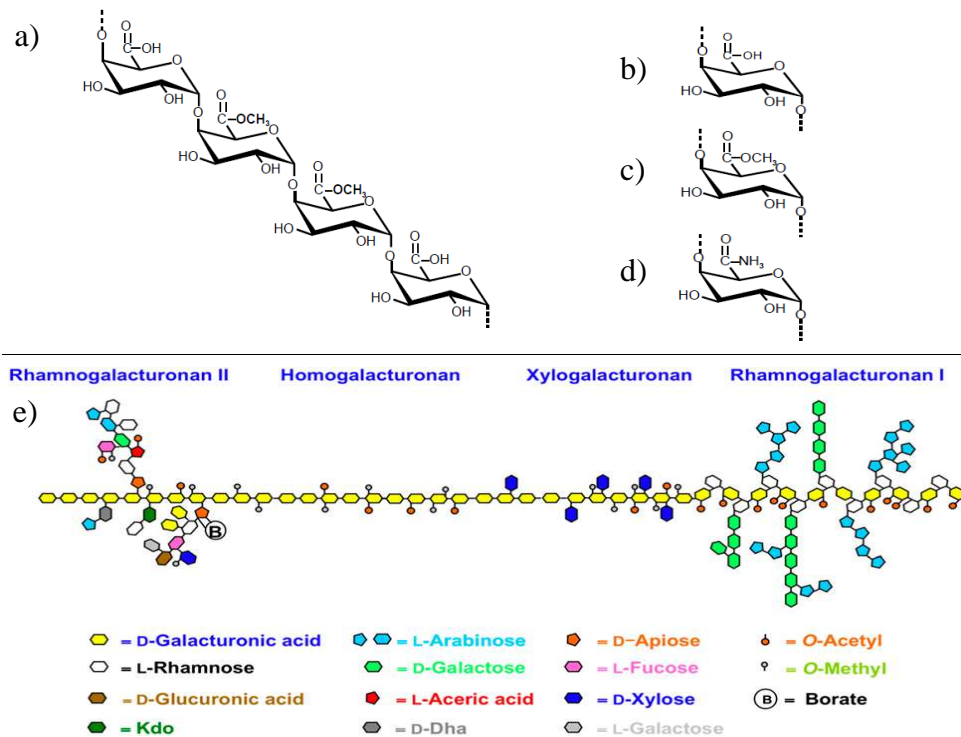
Figure 1.3: Structure of the pectin. **a)** Short segment of the Homogalacturonan, showing methylated and free carboxylic acid residues [56]. **b-d)** Free, methyl-esterified and amidated forms of a GalA residue, respectively [56]. **e)** Scheme of a pectic molecule with some of its domains HG, RG I & II and Xylogalacturonan. Kdo, 3-Deoxy-D-manno-2-octulosonic acid; D-Dha, 3-deoxy-D-lyxo-2-heptulosaric acid [22]

turing of chains using pectinases. After extraction, pectins are standardized for a variety of industrial application [49, 56]. Its most known industrial application is the production of jam due to its gelling properties. Pectin is also used as a stabilizer for milk-containing drinks and other emulsions, as well as a fat-replacement for low-calorie foods. Pharmaceutical uses include wound bandages, due to its water-swelling properties and as neutralizing agent during irritations of the esophagus [49]. Pectin is also a potential agent for drug delivery to mucous tissues or the colon [11, 34, 38]. Furthermore, there are reports that pectin is able to reduce blood cholesterol levels and that it can be applied against metal poisoning [56].

Pectins are classified according to their degree of esterification (DE), which is often used interchangeably with degree of methoxylation (DM). If more than 50 % of the carboxyl groups of the HG are occupied with methoxy groups, the pectin is called 'high methoxyl' (HM) pectin (HMP), otherwise 'low methoxyl' (LM) pectin (LMP) [49, 56]. LM pectins have a much higher charge density than HM pectins [38] at the same pH due to unprotonated carboxylate residues. Apart from naturally occurring methoxylation and acetylation, modification by amidation is possible by addition of ammonia [49, 56]. Acetylation is known to occur in apple pectin [49]. These parameters alter the solution and gelling properties (see section 1.2.2).

Another structural feature distinguishing pectins and their gelling properties is their 'degree of block-

iness' (DB). This quantity describes the distribution of the esterification pattern - the percentage of mono-, di- and trimers of galacturonic acid (GalA) obtained from enzymatic digestion, divided by the total amount of free GalA residues [55, 63]. PMEs from different sources produce different esterification patterns, that is, different blocksize and distribution. Plant-PME tend to give a more block-wise distribution, while fungal PME and chemical de-esterification results in a more random distribution [32, 38, 64].

Being a weak polyprotic acid, the pK of pectin varies with its charge density. The apparent pK_a ranges from 3.5 to 4.5 [49]. Pectins are principally soluble in water, but tend to form clumps due to rapid hydration; the core of the clumps are only semi-hydrated [49, 56]. Mostly pectin is heated to 70 - 80 °C to ensure full hydration. A more subtle way is the use of alcohol. Although insoluble in the latter, pectin solutions can be prepared by moistening the powder with iso-propanol and adding water under stirring [31, 49]. Pectate salts of monovalent cations like potassium are more readily soluble [56], while salts formed from divalent or trivalent ions are insoluble [49]. As a comparison, polygalacturonic acid (containing no side chains) is sparingly soluble in water, but readily soluble in phosphate buffer at increased pH (see 2.2.2) [54].

Care should be taken when adjusting the pH and temperature of pectins. While the polymer shows good stability in the pH range 3-4, HMPs are prone to β-elimination at pH above 5, except the temperature is kept below room temperature. LMPs on the other hand are more tolerant to this condition. At low pH hydrolysis can cause de-polymerization of the pectic chains and de-esterification, especially at elevated temperatures, which in turn is more of concern with LMPs [49, 56]. All the above mentioned factors have an influence on macromolecular properties of pectin, which will be discussed below.

1.2.2   Physico-chemical Properties

The viscosity of the solutions increases with decreasing pH, where LMP solutions are more viscous than HMP solutions at the same concentration. Conversely, in the presence of Ca^{2+} the viscosity of an LM solution increases with pH in the range of 2.5 < pH < 4.5 [49]. As has been observed in the laboratory, the HMPs should be stirred at lower speed ($\sim$ 300 rpm) than LMPs ($\sim$500 rpm) to avoid foaming. Due to the high viscosity of the solutions, it is not possible to produce pectin solutions at concentrations higher than 12 % (w/v), which requires dispersion at high temperature and high shear forces. It should be noted that handling such a "solution" is almost impossible. At 4 % w/w some LMPs are so viscous that the beaker needs to be fixed in order for the solution to be stirred (observed in the laboratory). It has been found, that dilute pectin solutions show Newtonian behavior, while more concentrated ones show non-Newtonian characteristics [56]. In the solution state and at slightly basic to neutral pH the negative charges along the backbone cause the backbone to be rather stretched due to coulombic repulsions, this conformation being further stabilized by a hydration shell. As the

pH is lowered protonation causes de-hydration of the chain and drives chain association, as will be discussed below.

As indicated earlier, pectin has the ability to form a gel, which is an interesting feature for various industrial applications. A gel is a three-dimensional cross-linked polymer network that is able to enclose water and possibly other soluble solids [49, 56]. The cross-links may be covalent or non-covalent [49]. A gel does not dissolve in water, but has the ability to take it up and swell [38], due to its poly-ionic character (often as a monovalent salt), which drives osmotic water uptake [49]. Principally, thickening and gelling of pectin solutions depend on the molecular size, the DE, the DB, the nature of the substituents, pH, ionic strength, presence of soluble solids and metal ions, concentration and temperature. The influence of some of these factors is introduced below.

For both HM and LM pectins the gelling temperature and firmness of the gels increase with decreasing pH. Nonetheless, there are substantial differences between HM and LM gelling mechanisms. Because HMPs do not have as many free carboxyl groups for cross-linking, they require the addition of about 55 % soluble solids (i.e. monosaccharides) below pH 3.5 and elevated temperature ($\sim 70\,°C$) in order to from a gel [38, 49]. The additional sugars apparently compete with water, thereby facilitating hydrogen bonding and hydrophobic interactions between the carboxyl and hydroxyl groups of pectin chains [56]. The ingredients are mixed above the gelling temperature, and gelling occurs upon cooling. Gels formed from HMPs are thermally reversible but do show hysteresis - the melting and setting temperatures differ and are positively correlated with DE [49].

LMPs can gel via two different mechanisms: by di- or trivalent metal ion chelation, or by acid gelation. Also, they do not require soluble solids in order to do so [49]. The acid gelation mechanism does not require Ca^{2+} ions, but a pH below 3.3. The reduction of the charge density promotes chain aggregation, allowing hydrogen bonding and hydrophobic interactions to occur, although such gels are weak [9].
Gelation via non-covalent cross-linking requires appropriate metal ion concentrations (in plants typically Ca^{2+}) and can be achieved at a wider pH range (acidic to neutral) [49]. According to the 'egg-box model', describing the cross-link formation mechanism, a calcium ion first dimerizes two pectin chains by electrostatic attraction to the carboxylate residues, thereby facilitating reorientation of the chains. This promotes cooperative binding of further ions. It is known that several consecutive carboxyl residues must be present for strong gel formation, although reports do not agree on the amount, which ranges from 6 - 20 free carboxylate residues [38]. The amount of calcium needed relative to the amount of free carboxyl groups can be calculated from Equation 1.1 [10]. The structure of a calcium-gel involves segments providing chain aggregation via the ion chelation and chain agreggation and segments that are free, as can be seen in figure 1.4. Viewed normal to the gel axis, the free segments span an area of up to 10 nm^2. Mg^{2+}, although a divalent ion is not able to gel a pectin solution due to its weak binding, while ions like Pb^{2+} and Cu^{2+} bind even more tightly than
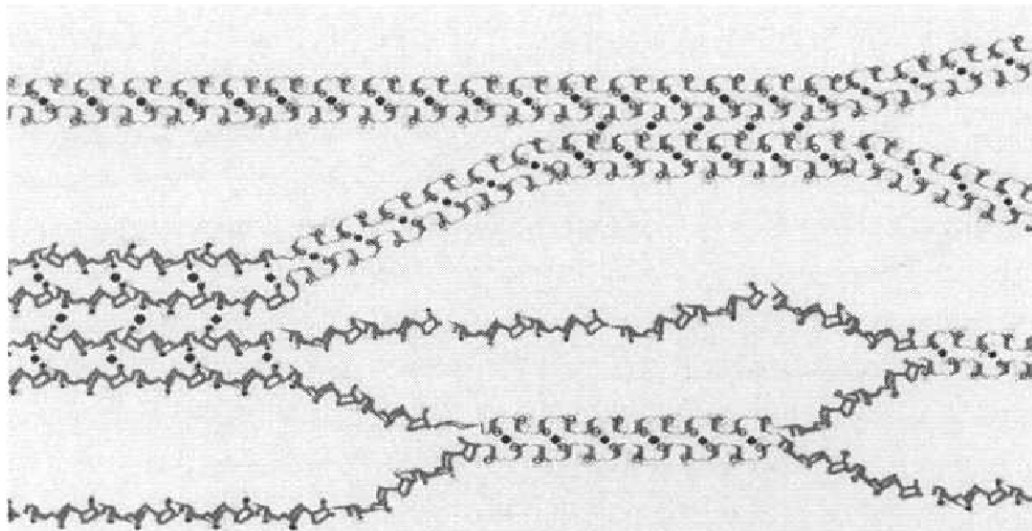
Figure 1.4: The egg-box model according to Goldberg *et al.*, 1996. Souce: [49]

calcium ions [49], although pectin has a higher specificity for the latter [10, 54].

$$R = 2[Ca^{2+}]/[COO^-] \qquad (1.1)$$

The cooperative binding of Ca^{2+} poses some practical issues. At room temperature the high affinity and cooperative binding of the ions causes instant gelation of the interface, and it takes time for the calcium to diffuse. As with HMPs, the solutions can be mixed at elevated temperature and will gel as the temperature is decreased, but as opposed to HMPs, LMPs do not show hysteresis. Another possibility to induce gelation is the use of a calcium sequestrant that slowly releases the Ca-ions, thereby facilitating the mixing of the calcium and pectin solutions before the gel sets [49].

Biological Pectin gels under load

Since pectin has important structural roles in plant tissues, many studies have been made on its mechanical properties [10, 17, 32, 55, 60, a.o.] . It has been shown that pectin chains in hydrated cell walls undergo reversible deformation under load, suggesting a potential load-bearing function. There are several deformation mechanisms and more detailed information can be found in [33, 49]:

Osmotic water uptake puts the individual chains under stress, although being hard to quantify because the negative charge density of the pectic chains is balanced by Ca^{2+}, partly reducing the osmotic swelling. As a result the structure becomes more rigid upon application of an external tensile stress [49]. A loose chain segment between two junction zones can straighten upon application of an external force, causing a decrease of entropy. When the tension is released entropy drives the restoration of the random-coil conformation (if the free chain segment is long enough). Due to steric effects pectin chains have a helical conformation. If the force is further increased, the axis of the helix can stretch. Because in pectin two helical conformations are possible, the monomers themselves may stretch by

a conformational change, thereby leaving the lowest enthalpy state [49]. The chains can thus act as enthalpic or entropic springs, or as both. The junction zones are another part of a pectin gel that play a role in the mechanics of deformation or breakage. While covalent bonds are not likely to break at forces that have been shown to break a pectin gel, non-covalent ones are. The size of the aggregate, binding force and interaction type of the monomers, as well as the rigidity of single chains (depending on conformation and composition) will affect the force needed to initiate its disruption [49].

1.3 Theory of Confocal Raman Spectroscopy

Confocal Raman Spectroscopy is a combination of two already powerful techniques per se. It allows the high resolution imaging of a waste variety of specimen using appropriate microscopy optics to gather the information about specific patterns found in the interactions of light an matter, in this case Raman interactions.

The Raman effect, together with a confocal microscope setup, leads to several advantages for many applications. In the first place, sample preparation is very easy in most cases and minimal amounts of sample are needed [30]. Because of the chemical sensibility of Raman scattering, multi-component analysis of mixtures is possible using suitable algorithms [30]. Additionally, 3D imaging is possible with the confocal microscope in combination with the displacement of the sample by a scan stage and/or a step motor [14]. This also enables the analysis of samples inside containers such as plastic and glass [53], for example for industrial online-analysis. Inorganic materials can be analyzed due to polarization filters, and thus orientation can be monitored and crystallinity calculated. Because water gives a relatively small Raman signal, biological samples can be easily imaged in the native, hydrated state, without major interference.

In the following chapter the necessary theoretical background of the above mentioned technique will be given.

1.3.1 Vibrational Spectroscopy

When a molecule interacts with photons, the latter can be scattered, absorbed or just pass through [53]. Which of these processes is activated depends on the energy of the photons, which will cause either the electronic, rotational or vibrational energy of the bonds of molecule to change. For vibrational spectroscopy only the processes that alter the vibrational energy of the molecule are considered[30]. The two techniques that deal with vibrational spectra, namely Raman and InfraRed (IR) spectroscopy, have long since been used as complementary techniques, since they show different vibrational modes of the same molecule. The difference between them is that while Raman is a scattering effect, IR is an absorption effect. More details about this difference will be given in section 1.3.2. In general, when a molecule interacts with electromagnetic radiation in order to absorb or create a photon, it must at least

temporarily have an oscillating dipole moment with the same frequency as the absorbed or created photon. The process of absorption or emission/scattering involves a transition up or down from one energetic state to the next [2].

Molecular Motion

Molecules, although often not apparent, are always in motion. The degrees of motional freedom describe in how many ways a molecule can move, whereas the internal degrees of freedom specifically describe vibrational movements (also termed normal modes) of the molecule. The rule-of-thumb for a non-linear molecule is $3n$-6 degrees of freedom (DF), and for a linear molecule $3n$-5 DF, with n the number of atoms in the molecule. The $3n$ term arises from a possible movement of every atom into the X, Y and Z directions [30]. For non-linear molecules the '-6' term accounts for translational and rotational motion in X, Y and Z, while for linear molecules the '-5' term accounts for the fact that a rotation around the own axis does not involve displacement of the atoms [12].

The normal modes describe types of vibrations with different frequencies that alter bond lengths and/or angles. A schematic representation of these can be seen in Fig.1.5. The bond length is altered by stretching (abbreviated ν), which can be in-phase (symmetrical), or out-of-phase (asymmetrical) (ν_s and ν_{as}, respectively) . A change of bond angles is designated as a bend or deformation (δ) . There are several possible deformations, that have different energies: scissoring and rocking are in-plane bendings (δ_{ip}) , while wagging and twisting are out-of-plane bendings (δ_{oop}) [50, 51]. Sometimes vibrations are degenerate, that is, they have the same energy although the movement itself is not the same [12].

It should be noted, that a normal mode is rarely a pure stretch or bend, but rather a combination [12]. When a molecule is in the normal mode of vibration, all its atoms displacements are independent [12] and sinusoidal when plotted as the Cartesian coordinate against time. Their frequency and phase are the same, although the amplitude is mostly different. Hence, all the atoms go through the equilibrium position at the same time, and the center of mass does not move, nor is the molecule in rotation [30] or translation [12], at least in the higher pressure state of liquids [62]. In practice, normal coordinates, Q , are used to describe the nuclear displacement and can be regarded as the amplitude of the vibration [30].

Classical and Quantum mechanical description

The frequency or wavenumber of a vibration can be approximated with the classical model of the harmonic oscillator represented by two masses linked by a massless spring [30]. By application of Hooke's law equation 1.2 is obtained. It gives the relationship of vibrational frequency, v, the reduced
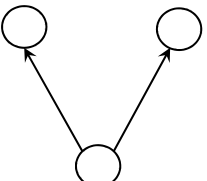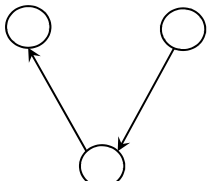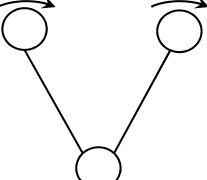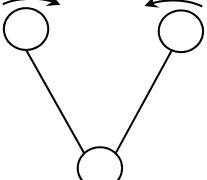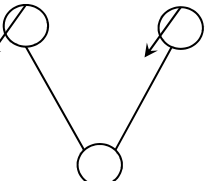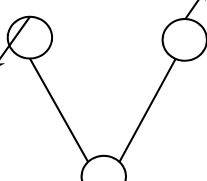
	Symmetric	Assymetric
Stretching	ν_{ip}	ν_{op}
Bending in-plane δ_{ip}	Rocking	Scissoring
Bending out-of-plane δ_{oop}	Wagging	Twisting

Figure 1.5: Schematic representation of possible vibrational modes

masses of the atoms involved, $\mu = \frac{m_1 \times m_2}{m_1 + m_2}$, and the force constant k of their bond [53].

$$v = \frac{1}{2\pi c} \times \sqrt{\frac{k}{\mu}} \tag{1.2}$$

where c is the speed of light in vacuum. This equation also indicates that the lighter the atoms involved in the bond, the higher the frequency of vibration.

The potential energy, E_{pot} , at a given internuclear distance, x , is given by Equation 1.3 [30]. The proportionality factor k is again the force constant between the masses [12].

$$E_{pot} = \frac{1}{2}kx^2 \tag{1.3}$$

For more accurate calculations, the quantum mechanical model of the harmonic oscillator can be used. One fundamental difference to classical mechanics is that energy is quantized, that is, has discrete, non-continuous, values. Therefore, also the vibrational energies can only exist in quantized portions, and differ from each other by integer numbers. Because of the wave-particle dualism, any molecular vibration can be described as a wave, and its energy calculated using:

$$E = (\nu_i + 1/2)h\nu \tag{1.4}$$
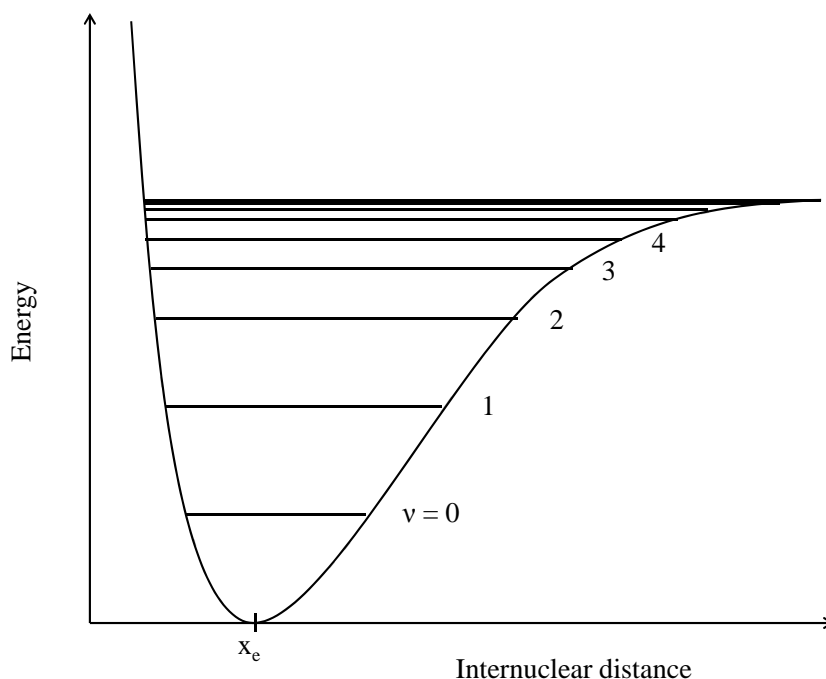
Figure 1.6: The unharmonic Oscillator.

where $\nu_i(= 0, 1, 2, ...)$ is the vibronic level, v is the classical vibrational frequency and h is Planck's constant (6.6256×10^{-27} erg sec) [30].

The quantum mechanical harmonic oscillator of a diatomic system is described by a parabola when the energy is plotted against the internuclear distance. The energy zero-point is reached at the vibrational ground level ν_0. By insertion into equation 1.4 above, it can be seen that the remaining energy is $E = 1/2\ hv$, which implies that there is no state were the molecule is not at least in minimal motion [30].

In reality most, if not all, systems should be described as unharmonic oscillators, the main difference being that the vibronic levels are not equidistant from each other, their spacing becoming smaller with increasing energy level, as depicted in Figure 1.6. The Morse potential explains this effect by considering the fact that the restoring force is not proportional to the displacement of the nuclei [12]. This explains the fact that at a certain vibrational energy, and therefore internuclear distance, the bond will simply break. This model explains the existence of fundamental state transitions ($\Delta\nu = \pm 1$), as well as overtones ($\Delta\nu = \pm 2$) and combination bands, of which the latter two are not allowed within the harmonic framework [30].

Electromagnetic Radiation

Light is a form of electromagnetic radiation. It consists of an electric and a perpendicular magnetic part that each oscillates in a sinusoidal fashion, and is classically regarded as a wave. In the field of

vibrational spectroscopy only the electrical field component is considered [30]. The field is characterized by its wavelength λ (length of one oscillatory cycle), its frequency v (cycles per unit time) and its wavenumber $\bar{\nu}$ (cycles per unit length in cm^{-1}), and their relation is given by Equation 1.5:

$$\bar{\nu} = v/c = 1/\lambda \qquad (1.5)$$

where c is the speed of light [62].

In the quantum world, light is also quantized and as such is called a photon - a 'portion' of light, with its energy given from relation 1.6 [30, 53].

$$E = hv \qquad (1.6)$$

1.3.2 The Raman Effect

In Raman Spectroscopy a monochromatic, linearly polarized light source - a laser - is used to irradiate the sample, and the frequency shift of the scattered light is detected.

The process of light scattering involves two photons and is an off-resonance effect. In simple terms: when a photon interacts with a molecule it can associate with it to create a 'virtual', higher energy level (ν^*). Upon relaxation, a photon is emitted and the molecule returns to a lower vibrational level. Most photons are elastically scattered and have the same energy as the incident photon, giving rise to the predominant Rayleigh scattering. Some photons have more, respectively less, energy and gives rise to Raman scattering, which is inelastic scattering. If the photon has more energy than the incident photon, then this is called anti-Stokes shift, while the opposite is called Stokes shift [30]. This basic difference is represented in Fig. 1.7. The shift refers to the fact, that the wavelength of the scattered light is shifted in relation to the incident light (see equation 1.6).

No matter, if the molecule has an inherent dipole or if the dipole is solemnly induced by the electric field, it will oscillate at the same frequency as the incident field (v_0). The induced dipole moment is in fact a charge re-distribution, where the electron cloud is distorted from the nucleus by the external electric field. The amplitude of that oscillation depends on the polarizability α, which determines how much the electron cloud can be distorted and is a time dependent phenomenon. As a consequence, the dipole moment is amplitude-modulated by the changing polarizability of the bond, and the photon that is emitted gains or loses part of its energy when colliding with a molecule. Equation 1.7 shows the relation of the dipole moment μ, the molecular polarizability and the electric field, E.

$$\mu = \alpha E \qquad (1.7)$$

The amplitude modulated signal can be mathematically resolved into three frequency modulated components with steady amplitudes: $v, v_0 + v_m$ and $v_0 - v_m$ as shown in Fig. 1.7 and 1.8 [30]. The loss
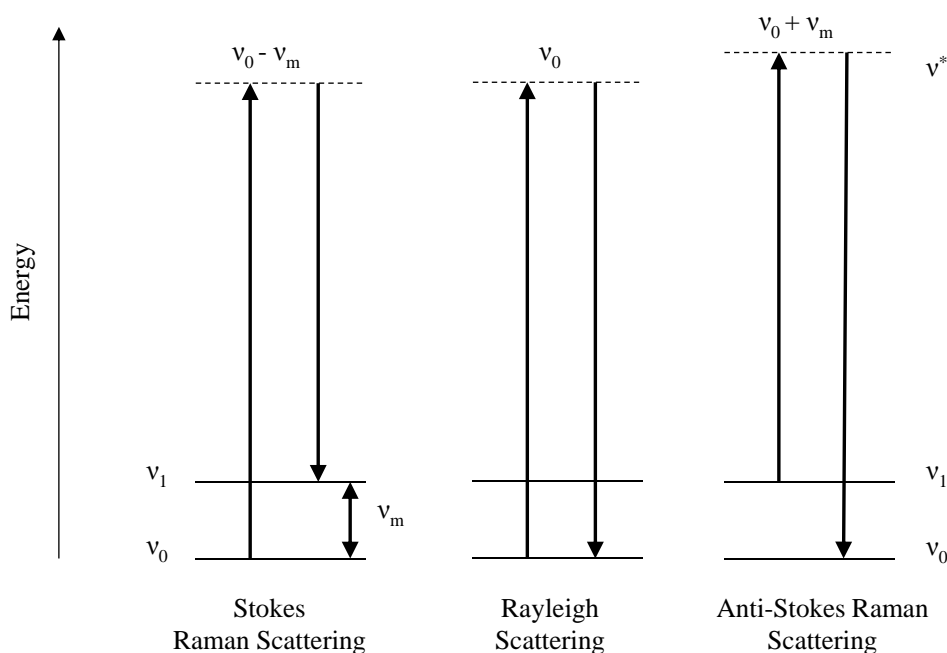
Figure 1.7: The basic difference between anti-Stokes, Rayleigh and Stokes scattering is the energy change before and after the excitation ν_m. Note that the virtual state (ν^*) of the anti-stokes scattering is higher in energy.

or gain of energy depends on the initial and final vibrational level. ν_m is the difference in frequency between the ground vibrational level and the first excited state, which in turn is characteristic for the type of bond [30].

In a Raman spectrum the frequency difference between the incident and detected light is plotted in wavenumbers. This is the reason why the Rayleigh peak is the zero point $\bar{\nu}_0$, and the Raman peaks are at $\bar{\nu}_0 \pm \bar{\nu}_m$, as can be seen in Fig.1.9 [67]. According to the Boltzmann distribution, most molecules are in the ground vibrational level at room temperature. Therefore, the more likely event is the more intense Stokes scattering, where the molecule is exited from the ground vibrational level and returns to the first vibrational level upon relaxation, thereby gaining some energy [30]. This is why the photon loses some energy and oscillates at frequency $v_0 - v_m$. At higher temperature anti-Stokes scattering gains intensity [12].

Because Rayleigh scattering is the most likely event, its intensity is only about 10^{-3} weaker than that of the incident light, while Raman scattering is weaker by a factor of 10^{-6} [62]. The intensity of a specific, observed anti-Stokes signal is, among others, dependent on the fourth power of the incident
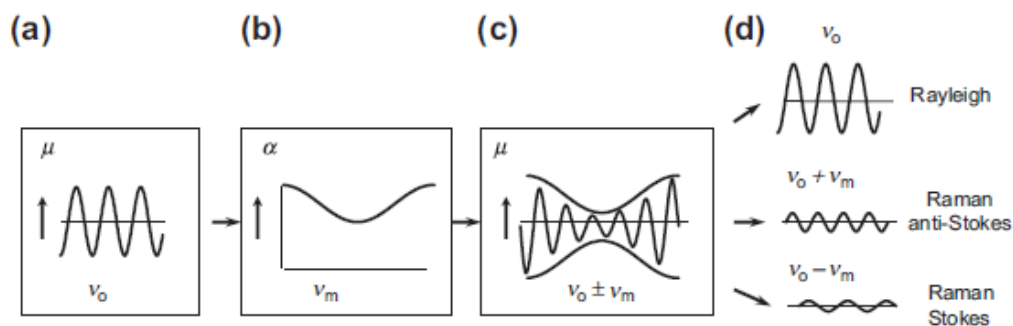
Figure 1.8: Scheme of the waves that lead to Rayleigh and Raman scattering signals. (a) represents the induced dipole oscillation at the frequency of the incident radiation v_0; (b) the change of the polarizability of the molecule, caused by the vibration. In (c) the amplitude-modulated dipole oscillation, that can be resolved into (d) three frequency-modulated, steady-amplitude waves, that give rise to the Rayleigh, Stokes and anti-Stokes Raman scattering. The scheme was taken from [30].
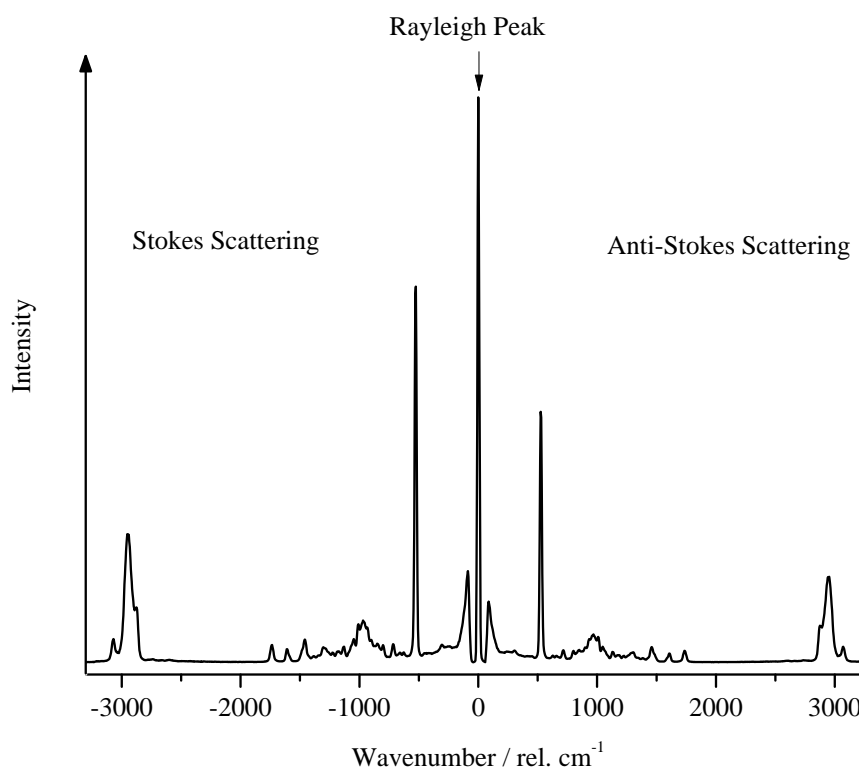
Figure 1.9: Exemplary full Raman Spectrum of microscopy oil. The highest peak in the middel is the Rayleigh peak; to its left the more intense Stokes scattering with negative shifts and to the right Anti-Stokes scattering with positive shifts.

light's frequency, and is given by:

$$I_R \propto v^4 I_0 N \left(\frac{\partial \alpha}{\partial Q} \right)^2 \tag{1.8}$$

where I_0 is the intensity of the incident light, α the polarizability and Q the amplitude change. N is the number of scattering molecules. From this it can be seen that the choice of the laser wavelength and its intensity, together with sample concentration, are crucial to the quality of the spectrum [30].

Comparison to Infrared Spectroscopy

A fundamental difference between IR and Raman spectroscopy is that the process observed in the IR spectrum is an absorption process, while a Raman spectrum arises from a scattering effect. IR is a resonance effect, where the energy of the photon has to match the vibrational energy gap of the molecule in order to be absorbed and promote the molecule to a higher vibronic level. Therefore, a polychromatic light source is used to excite the molecule and the difference between the intensities of incident and transmitted light is recorded. In order for a molecule to be IR active it must show a change in the dipole moment upon vibration [12]. Certain vibrations will cause the dipole moment to change, while others will change the polarizability only or additionally. Hence, certain vibrational normal modes will be IR active, while others will be Raman active, or (not) active in both cases. From this it follows that these two techniques can provide complementary information [30]. The symmetry of a molecule can provide, at least partially, information on what kind of vibrations are to be expected, and this will be discussed below.

Symmetry and the rule of mutual exclusion

To determine if a bond, or group of bonds, is Raman and/or IR active, and which signal originates from which type of bond, the molecule's symmetry must be considered. Heavy atoms generally move less than light atoms, and bends tend to vibrate at lower frequencies than stretches [12]. Additionally, symmetric stretches and non-polar groups tend to be more Raman active, while asymmetric stretches and polar groups tend to show stronger IR activity.

In Group theory the symmetry elements of a molecule are classified into point groups and applied on vibrational spectroscopy. The details lie beyond the scope of this thesis, and so only the most important aspects will be mentioned. The rule of mutual exclusion states that any vibration of a centro-symmetric molecule can only be IR or Raman active, due to its high symmetry. If the center of symmetry is retained during the vibration, the molecule can be Raman active, but will certainly not be IR active (and the opposite is true as well) [30]. Planar molecules and those possessing an axis of symmetry can be both Raman and IR active. The symmetric stretch of a homonuclear diatomic
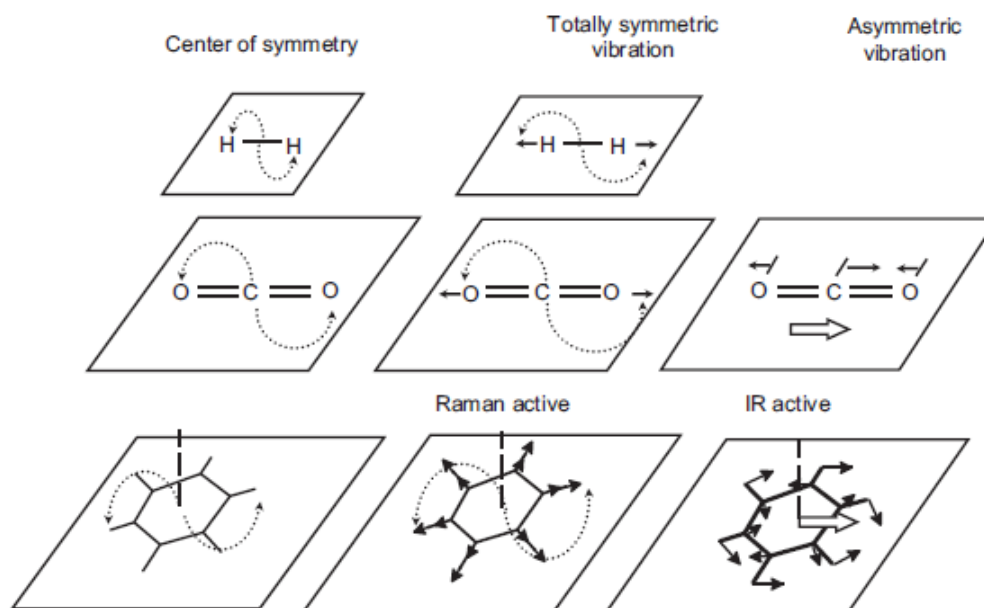
Figure 1.10: Possible stretching vibrations of different planar molecules with a center of symmetry. When the polarizability changes, the vibration is Raman active, if the dipole moment changes, then the mode is IR active. The scheme was taken from [30].

molecule will cause a change in the polarizability of the molecule, but it will not change its dipole moment, and thus, it will be Raman active only – an advantage for Raman spectroscopy. On the other side, the dipole moment and polarizability of a heteronuclear diatomic molecule will change as the bond stretches, and will thus be both IR and Raman active [12]. Asymmetric stretches of polyatomic molecules exhibit more IR activity, as the dipole moment of a molecule changes during an asymmetric vibration, but not, or just to a low extend, the polarizability. It should be noted, that asymmetric stretches in Raman, and symmetric stretches in IR can be observed, but have rather low intensities [12]. Figure 1.10 [30] shows some planar, homo- and hetero-atomic molecules and their stretching possibilities.

As an illustration, the number of vibrations of a water molecule will be calculated and Raman/IR activity assessed. H_2O has three atoms and is not linear. Applying the $3n$-6 rule, with $n = 3$, gives 3 vibrational modes. The symmetric stretch comes at $\bar{\nu} = 3652 \text{ cm}^{-1}$ and is predominantly Raman active, while the asymmetric stretch ($\bar{\nu} = 3756 \text{ cm}^{-1}$) and the bending vibration ($\bar{\nu} = 1595 \text{ cm}^{-1}$) show strong absorption in the IR spectrum, and are very weak in the Raman spectrum. This leads to an advantage of Raman over IR spectroscopy: since the absorption of the bending vibration of water in the IR region is strong and in the lower spectral region, other peaks might be hidden, and so, the inspection of moist or wet samples, like biological samples, is preferentially done with Raman spectroscopy [53].

1.3.3   Confocal Raman Microspectroscopy

In order to understand the functioning of this Raman imaging technique, the section below will give an introduction to the optical elements enabling the imaging - confocal microscopy.

Confocal Microscopy

The basic definition of a confocal microscope is the alignment of a point source of excitation light (a laser), an illuminated focus point within the sample and a pinhole with a detector [12]. This configuration enables the observation of single points within a thick sample resulting in high contrast and optionally 3D images, as will be detailed below.

The point-like excitation source is focused onto the sample through an objective lens and illuminates only a tiny spot of the sample very brightly, while the rest will receive less light and contribute little to the detected signal. This is the first difference to a conventional wide-field microscope, which uses an extended light-source that is focused into one plane, but illuminates the whole sample and thus, information from out-of focus planes is detected with higher intensity as well. The placement of a pinhole in the image plane allows the separation of the out-of-focus radiation from the in-focus radiation, which should be detected. This is the essential difference to wide-field microscopy: light from the focal point can be separated from light next, above or below it. The implication of this is that only one point of the sample can be observed at a time, and thus, the sample must be scanned (i.e. with a scanning stage) in order to obtain an image [12]. A basic representation of this concept can be seen in Fig. 1.11.

The quality of the image depends on various parameters, some of which must fulfill the following relation:

$$\frac{M}{NA} \geq \frac{\pi d_0}{v_{p_{max}} \lambda} \tag{1.9}$$

M is the magnification and NA the numerical aperture of the objective. d_0 is the diameter of the pinhole; $v_{p_{max}}$ is the detector radius and λ the excitation wavelength.
The magnification determines the beam path length. The numerical aperture determines the angle of light waves [45] and therefore the amount of light that can be gathered by the lens and how well it can be resolved spatially.

$$NA = n \ sin \, \alpha \tag{1.10}$$

Where n is the refractive index of the medium between the objective and the sample (air, water or oil) and α is half of the aperture angle.
The pinhole diameter determines how much light within the illumination volume can reach the detector, and will thus determine the intensity of the signal and influence resolution. The illumination volume itself depends on the wavelength of the incident light and the objective [14]. The detector radius determines the area of the pinhole that the detector covers and is used interchangeably with
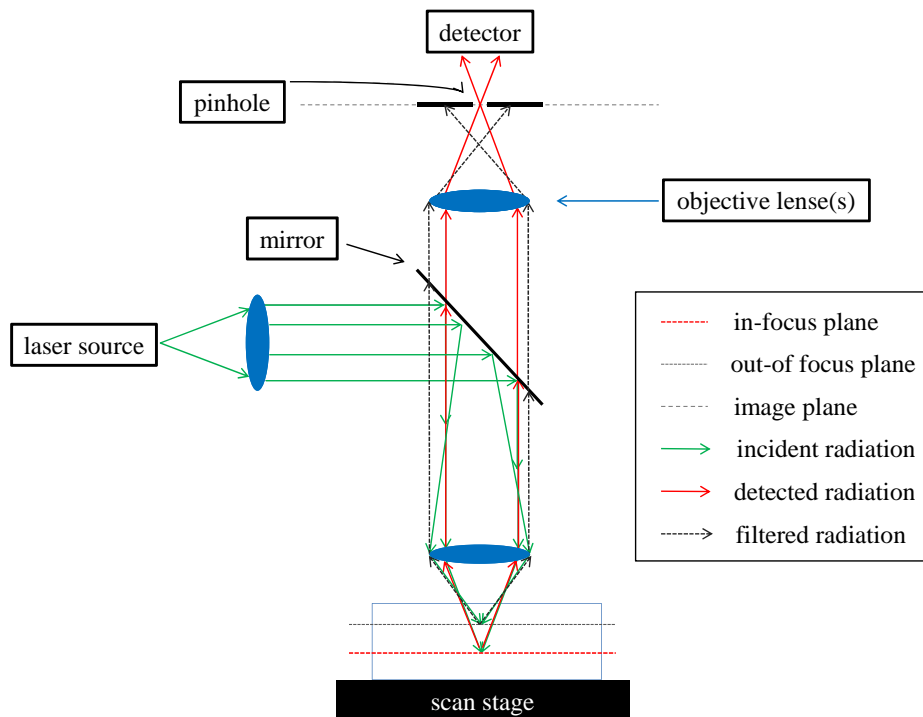
Figure 1.11: Representation of the light beam pathways in a confocal microscope

pinhole size in [14], probably due to the fact that the area of the detector is usually bigger than the pinhole size.

These parameters influence the three-dimensional energy distribution of the light, described by the Point Spread Functions (PSFs) . These account for the quality of image formation. The PSFs can describe the electric, magnetic or total energy density in a point and their patterns are mainly caused by diffraction from lenses and objectives [14]. This description arises from the fact that focused light forms a double cone in the axial direction, with the highest intensity at the center – the focus point. Rotated laterally by 90°, this results in a circular diffraction pattern. The radius of the innermost dark ring is a measure for the resolving power of the objective. The PSF of excitation is located in the sample and increases with decreasing aperture angle, which in turn lowers the resolution. The PSF of detection locates to the pinhole, and is mainly influenced by the pinhole size [12]. Ideally, the pinhole is adjusted so that only the central part of the focused light passes through [14]. Increasing the pinhole size gives higher signal intensity, while trading off against resolution.

An optical system is characterized by its effective PSF, the intensity of the signal observed, that is a three dimensional representation of the diffraction pattern [45]. It is composed of PSF of excitation and the PSF of detection. Because those two functions are independent of each other, the effective PSF is given by their product [12, 14]. This can be viewed as the probability of detecting a photon that was emitted by the point light source, interacted with the sample and, from there, went through the pinhole and to the detector [12].

Depending on the technique used, different types of detectors are employed. An image is constructed by scanning (imaging) the sample, that is, to make a measurement at every (self-definable) equidistant

point of the area of interest. This is often done by moving the specimen relative to the objective (in x, y and z directions) with a piezo-electrical scan stage. Provided the sample is homogeneous [41], thick samples can be looked at without using conventional sectioning techniques – this is called optical sectioning [12].

Considerations for Confocal Raman Microspectroscopy

As discussed in section 1.3.1, the Raman signal is a form of scattering. At a given excitation wavelength and intensity the intensity of the scattering, inherent to the sample, is another parameter that needs to be taken into account in order to explain the observed intensities. The scattering occurs in all directions and is subject to a wavelength shift [14]. The intensity PSF (I_{CF}) for a confocal Raman emitting point is thus:

$$I_{CF} = h_{eff}{}^2 \cdot f(x, y, z) \tag{1.11}$$

With $h_{eff} = h1(u, v)\, h2(\dfrac{u}{\beta}, \dfrac{v}{\beta})$.

$h1$ and $h2$ correspond to the excitation and detection PSFs, respectively. u and v are the optical coordinates of the sample, and $\beta = \lambda_2/\lambda_1$ (were λ_1 = excitation and λ_2 = distribution of scattering wavelengths). $f(x, y, z)$ is the Raman generation [14]. It can be seen from the definition of h_{eff} that the effective PSF becomes smaller with increasing wavelength shift and therefore the intensity and the resolution decrease [14]. Also, when $h1$ for large aperture angles is compared with $h1$ for small angles, it can be seen that the symmetry of the electrical energy density depends on the initial polarization direction, and this of course influences the signal intensity [14].

The lateral (x, y) resolution (Δx) of a confocal microscope is given by the Full Width at Half Maximum (FWHM) of the intensity of the PSF. It depends on the wavelength and the numerical aperture as given by equation 1.12 [14]:

$$\Delta x = 0.61\lambda/NA \tag{1.12}$$

The axial resolution, that is, the thickness of an optical section, is given by:

$$\Delta z = 1.26n\lambda/(NA)^2 \tag{1.13}$$

Where n is the refractive index and λ the wavelength in vacuum [12]. Of course the pinhole size must be adjusted accordingly.

In the apparatus the light is delivered to the sample and to the detector by well isolated fiber optics, which allow the spatial separation of the laser source and the detector from the confocal microscope [67]. The detection fiber acts as a pinhole and is a multi-mode optical fiber with several channels of different diameter. Before detection the light coming from the sample must be filtered, because

the Rayleigh peak is so much more intense than the Raman signal and reflections from the sample surface are possible. The filtering device can be a Notch filter, an Edge filter or a series of at least two monochromators [53].

When a visible laser is used as in this work, a dispersive spectrometer and a Charge-Couple Device (CCD) are used for detection [53]. The dispersive spectrometer consists of a silicon grating where each wavelength is dispersed onto the detector at a different angle. The more grooves per mm (g/mm) the grating has, the higher is its spectral resolution [14] and the narrower the wavenumber range that can be covered at once. There are gratings with 600 and 1800 g/mm and some spectrometers allow switching of the grating. The resolution is considered to be high at a differentiation of 1 cm^{-1}, while lowering the efficiency of photon delivery to the detector. As a consequence the signal intensity decreases [14]. The CCD detector consists of an array of, typically 1024×127, silicon photodiods defining the number of pixels of the detected spectrum. Back-illumination and Peltier cooling improve the efficiency of detection.

General Practical Considerations

Even though sample preparation is straightforward with most samples, some issues have to be considered. For instance, it should be verified that no impurities or orientation effects alter the spectrum unknowingly [30]. Also, care should be taken when comparing different measurements, because the signal becomes weaker the further away it is recorded from the optical focus and the thicker the sample is. The signal intensities can thus differ substantially and an appropriate pre-processing step should be used [20].

Due to the confocal setup the often hard to control fluorescence is diminished compared to other techniques. However, fluorescence is one of the main disadvantages when using a laser in the visible range. Such interference can pose heavy restrictions on what kind of samples or, as the case may be, in which aggregate state a sample can be analyzed. As mentioned before, measurements in the hydrated state can damp the fluorescence and additionally diminishes the risk of thermal decomposition (sample burning) [53]. These facts make confocal raman microscopy a good tool for the investigation of biological samples. This thesis may serve as an example for this type of usage.

1.4   Data Analysis

The evaluation of confocal Raman spectra and images taken from biological samples, and more in general – spectroscopic data, is not an easy task, due to their multi-dimensionality [14] and the fact that there are often more variables (eg.: wavenumbers) than cases (eg.: spectra) [64]. This results in high requirements for the software during acquisition and data processing, as well as for the hardware. The dimensions, as mentioned earlier, include the spatial position (x, y, z) of the spectrum in

the sample area/volume, the spectrum itself with spectral shift and corresponding intensity, as well as time, if required [14]. The complexity of the spectra arises from the nature of the sample and effects coming from the, confocal measurement setup. In the case of images made from biological tissues, or extracted components of the latter, auto-fluorescence of the sample, co-localization of pure components, different signature of extracted pure components relative to native states, similarity of spectra of different monomers, orientation effects, as well as poor S/N ratios contribute to the effective dataset, just to mention the most important [42].

There is no convention on how such data are to be analyzed, and different authors use different uni- and/or multivariate approaches in combination with preprocessing steps. In the following, the methods used for data analysis in this work will be elucidated.

1.4.1   Preprocessing

Preprocessing of Raman data provides a means to exclude certain effects, like noise or background contributions caused by the instrument or fluorescence, in order to selectively simplify the data for the follow-up analysis, including image generation and multivariate analysis [14]. It has to be noted that great care should be taken when interpreting the results of multivariate analyses after certain preprocessing steps, as they can heavily influence the former [5]. This also counts for univariate analysis, as each processing step of the data changes the information content.

Cosmic Ray Removal

An effect regularly observed is cosmic rays. They arise from high-energy particles from outer space that interact with atoms and molecules in the Earth's atmosphere and with devices on earth, like the CCD camera in the spectrometer. They cause very sharp and narrow, high intensity peaks to be observed in many spectra [14]. In order to avoid their influence on e.g. a peak fitting procedure, they should be removed. This can be done either by considering neighboring spectral pixel or neighboring spectra in time or space scans, and to remove such outliers – the exact thresholds and ranges must be set by the user [14].

Background correction

Background correction of Raman spectra is an important step before an actual analysis, in order to exclude contributions from the CCD camera and the sample (auto-fluorescence, inhomogeneity of the background...) Given the natural variation within biological materials, a comparatively big and varying background relative to the peaks in the spectrum makes it difficult to compare the peaks themselves, as the background will be the predominant effect or even introduce artifacts in subsequent analysis [5].

There exist several methods to subtract the background from a spectrum, but most of them require the user to define some parameters, mostly by trial and error. One way is to fit a polynomial to the background and to subtract it from the spectrum. As done in this work with the WiTec Project Four Plus©software, the user defines the background and peak regions in the spectrum by hand, and the algorithm generates a polynomial of user-chosen order using only the regions marked as background. A mask can be generated from this marked regions and applied onto the spectra of other samples. The more complex the background of a spectrum is, the higher will be the order of the polynomial that describes it [8].

The problems of this user-selection are its robustness and reproducibility. The user must define a mask that will, in the best case, suite well all the spectra handled during batch processing and to know which order to choose for the polynomial, in short – the best fit. In the case of the WiTec software, the best fit can only be subjectively assessed by the user and requires some experience.

Pre-transformation

Depending on the question of the analysis and the structure of available data, different forms of pre-transformation like centering or standardization can and sometimes have to be applied [5]. For instance, due to using a confocal measurement setup, resulting in spectra taken at different sample heights, and different measurement parameters for extracted pectins and pollen (integration time/ excitation power), the total intensity of the spectra between samples and sample areas changes, resulting in higher weighing of more intense spectra upon comparison, which can be misleading. In order to compensate for this, especially when the goal is to classify spectra into groups, normalization of the spectra should be considered [19]. In literature it is not always clear what normalization means, as several ways exist. Here, the term normalization will be used for the scaling of each spectrum to unit area, as used in [25] and shown in equation 1.14 [5].

$$^{rs}x_{ij} = \frac{x_{ij}}{\sum_{j=1}^{J} x_{ij}} \tag{1.14}$$

Other forms of pre-transformation will be presented in the relevant sections, as they are applied only for certain analysis steps, and not throughout the whole chain of calculations.

1.4.2   Chemometrics

Chemometrics descibes techniques of multivariate analysis applied onto data of chemical or biochemical problems. This involves relatively basic but powerfull techniques like the principal component analysis, dealing with the description of a system, but also much more advanced techniques that can be used to create system models with strong predictive powers. In this work only basic chemometrics have been applied and the theoretical background is given below.

Principal Component Analysis (PCA)

PCA is a very powerful tool, provided the user is able to interpret the results correctly. According to Dieing et al. [14] the results of a PCA can be used to reduce the dimensions of the data set to the relevant ones and subjecting the results to eg. cluster analysis, which will reduce computational times. Also, by selecting the relevant or interesting components, the original spectrum can be reconstructed, which can aid to reduce the noise. Even though the error term will be greater, it is reasonable not to include the axes containing noise for the reconstruction [5, 14]. Furthermore, images can be reconstructed from the PCs. Last but not least, the ordination diagrams provide a way to find correlations between image pixel, or spectra from different origins. In this work, PCA was additionally used to find the best fitting polynomial for background correction, see Section 2.4.1 and 3.1 for more details.

The PCA is a linear, unconstrained ordination method [52], which allows the reduction of a multivariate data set into its principal components [14] . The data set contains I cases/observations (rows) with J different variables (columns), and thus has I points in a J-dimensional space. In simple terms, a PCA seeks out new variables (= principal components) that are linear combinations of the given variables and contain as much variance (in the sense of information) about the cases as possible. Also, the newly found variables must be independent of each other. Then, the relation of the cases and/or variable values can be visualized with the help of an ordination diagram; this is, plotting the principal components against each other. In other words, a new coordinate system consisting of the principal components (PCs) must be found, so that the cases are oriented in the direction of greatest variation for both plotted PCs, also called axes. This is done by rotating the system in such a way, that the data points are most widely spread along the axis [13]. The basic algorithm is explained below, and was adapted from [52]:

Step 1: Assign arbitrary case scores t_i

Step 2: Calculate new response variable scores p_j by doing a linear regression from t_i

Step 3: Calculate new t_i by calibration from p_j

Step 4: Remove arbitrariness of the scale by standardization of the case scores (stretching the axis)

Step 5: Stop on convergence, else iterate from step 2.

For a linear model, the calibration in step 3 is done by a least squares regression of the response variable score to the case score. The response variable scores correspond to the regression coefficients of each response variable for each axis. The response variables themselves are mean centered (mean = 0) across the cases. This algorithm will lead to the first PC (PC0 in this work). The following axes are found by considering the remaining variance (not explained by the previous PCs), but with the

constraint of being linearly independent of all previous axes [52].

This problem is usually dealt with using matrices, and there are various computational approaches. This adds some confusion to the terms used for a PCA, because different fields of application use different expressions to define the same thing, or even use the same expression for different things. The most important terms used in chemometrics are explained below.

The original data matrix is designated *X* and has the dimensions $I \times J$. The rank L of this matrix is defined as the minimum number of rows (*I*) or columns (*J*) of *X* and gives the maximal number of non-zero principal components [1, 5]. *X* can be transformed into

$$X = T \cdot P + E \tag{1.15}$$

where *T* is called the score matrix (= case scores), *P* the loading matrix (= response variable scores) and *E* represents the error matrix. The original value of a single element x_{ij} of the *X* matrix is then given by $x_{ij} = t_i \cdot p_j + e_{ij} = \hat{x}_{ij} + e$ [5].

The score matrix T has the dimensions $I \times L$. It consists of column vectors (t_l) for each principal component ($l...L$), also called eigenvectors [5]. This matrix describes the position of each sample (case) in the PC space [29]. The elements of *T* have the property of being orthogonal to each other, if, and only if, their eigenvalues differ. If this is the case, the square matrix $T' \times T$ results in a diagonal matrix, the elements of which are zero values, except in the diagonal, where the eigenvalue of the respective axis can be read out [1, Appendix A]. Each successive axis will have a lower eigenvalue and the proportion of variance explained by an axis is usually expressed as the percentage of the eigenvalue of the axis over the sum of all eigenvalues. The loading matrix *P* has the size $L \times J$. It consists of row eigenvectors (p_l) for each PC, and these represent how much the original variable contributes to the respective principal component [1, 5, 29]. In the NIPALS method the loading vectors are normalized to 1, this is, $\sum_{j=1}^{J} p_{aj}^2 = 1$. Thus, the square matrix $P \times P'$ results in an identity matrix and gives the number of PCs [1, 5]. The error term can be obtained by the Residual Sum of Squares (RSS) over all eigenvalues, which also equals the sum of squares for the error matrix *E*, with element e_{ij} [5].

The following paragraph will re-frame this concept for spectroscopy. First of all, a PCA can be done using a whole image, or using spectra from different samples. In the case of an image, the image data set consist of *I* pixels, each of them containing a whole spectrum with *J* spectral pixel (1024 pxl including the Rayleigh peak). Each spectral pixel is regarded as a variable, and thus a dimension, and its value, the CCD counts, determines the size of the variable. Furthermore, the pixel of the spectrum cannot be regarded as independent, since a peak usually spreads over several pixels, and thus result in

a direction [14]. The loadings of the first few (relevant) axes will therefore show whole peaks, while the rest of the PCs (i.e. eigenvalue < 1 %) will only describe noise. If a spectrum is very noisy, then even the first axes will very probably describe noise only [5, 14]. Thus, it is important to have a good signal to noise ratio, which can be improved by some smoothing procedure.

K-means Cluster Analysis

K-means cluster analysis (KMCA) is an analytical tool designed to classify data according to their dissimilarity. It is a non-hierarchical [52] or 'pseudo-hierarchical' [14] classification method that is widely used in tissue analysis [3] and based on the dissimilarity of a set of variables belonging to one sample [14, 52]. I In spectroscopy the set of variables is the spectrum itself, and the analysis of a spectroscopic image results in a spatial map of clusters, with each having a distinct spectral signature [3].

The goal of the algorithm is to partition a data set, comprised of n data points each described by j variables, into a predetermined number of groups, k (with K < N), by minimizing the intra-group distance, while maximizing the inter-group distance and without assuming any statistical distribution [23, 52]. This is achieved by randomly assigning all the data points to one and only one of the k clusters. The dissimilarity of the spectra can be computed via the Euclidean distance $d(x_i, x_{i'})$, as given by the equation below [23]:

$$d(x_i, x_{i'}) = \sum_{j=1}^{J}(x_{ij} - x_{i'j})^2 = ||x_i - x_{i'}||^2 \tag{1.16}$$

It follows from equation 1.16 that the Euclidean distance between two cases, x_i and $x_{i'}$, is equivalent to summing the squared difference of each variable in each case (x_{ij}). The cluster assignments are characterized by an encoder $k = C(i)$, whose particular solution C^* is to be minimized [23, 68]:

$$\begin{aligned} C^* &= min_C \frac{1}{2} \sum_{k=1}^{K} \sum_{C(i)=k} \sum_{C(I')=k} ||x_i - x_{I'}||^2 \\ &= min_C \sum_{k=1}^{K} N_k \sum_{C(i)=k} ||x_i - \bar{x}_k||^2 \end{aligned} \tag{1.17}$$

Where $\bar{x}_k$ is the mean vector of the kth cluster, and $N_k = \sum_{i=1}^{N} I$ is the number of points associated to that cluster. This function describes how distant the individual cases of one cluster are from the mean calculated by all the points belonging to that cluster, in other words the variance of the cases

[23]. For the spectroscopic image this means that an average spectrum is computed for each cluster and all spectra are compared to each of the cluster means and reassigned to the cluster with the lowest distance [68]. Because this is computationally very expensive, the algorithm works in an iterative manner by always reducing the value of C* until convergence[23]. According to the WiTec Project Four Plus$^©$help file the steps are:

Step 1: Initialize all cluster centers, that is, calculate the mean spectra of all randomly assigned clusters

Step 2: Compare each spectrum to each of the cluster centers and associate each spectrum to the cluster with the less distant mean

Step 3: Recalculate the cluster centers

Step 4: Reinitialize at step 2 until convergence

It should be noted, that although the algorithm is ensured to converge, it can do so on a local minimum, and hence not represent the optimal solution [3, 14, 23, 52]. Thus, the user is advised to repeat the same analysis various times, also starting with various cluster numbers k [52] in order to find a good solution. Also, it is recommended in Dieing et al. [14] to remove the background prior to cluster analysis. The term 'pseudo-hierarchical' arises from the fact, that the resulting clusters can in turn be partitioned into k clusters and the user can re-merge the subclusters in a different way. Thereby some refinement of the cluster distribution can be achieved, although this should be interpreted with care, as subjective user intervention is necessary for this. Several kinds of pre-transformation can aid the optimization of the clustering. Data reduction, here in the sense of averaging over several wavelengths, reduces noise and computational time. Manhattan or Euclidean normalization can increase the sensitivity to spectral shape, while being insensitive to intensity differences caused by integration time or material density. In this work the Manhattan norm was used, as it retains the proportionality of the signal, while with the Euclidean norm the impact of small values is suppressed. Finally, it can sometimes be of use to work with the derivative of the spectra, in order to increase sensitivity to sharp Raman peaks [68]. Derivatives also aid the removal of residual fluorescence contributions [5].

1.4.3   Image Generation

As already mentioned in section 1.3.3, the data for an image are generated by recording spectra at a selectable distance to each other in a two- or three-dimensional space. In the simplest case an image is formed by representing the intensity or wavelength shift of a peak of interest as a function of the spatial coordinate.
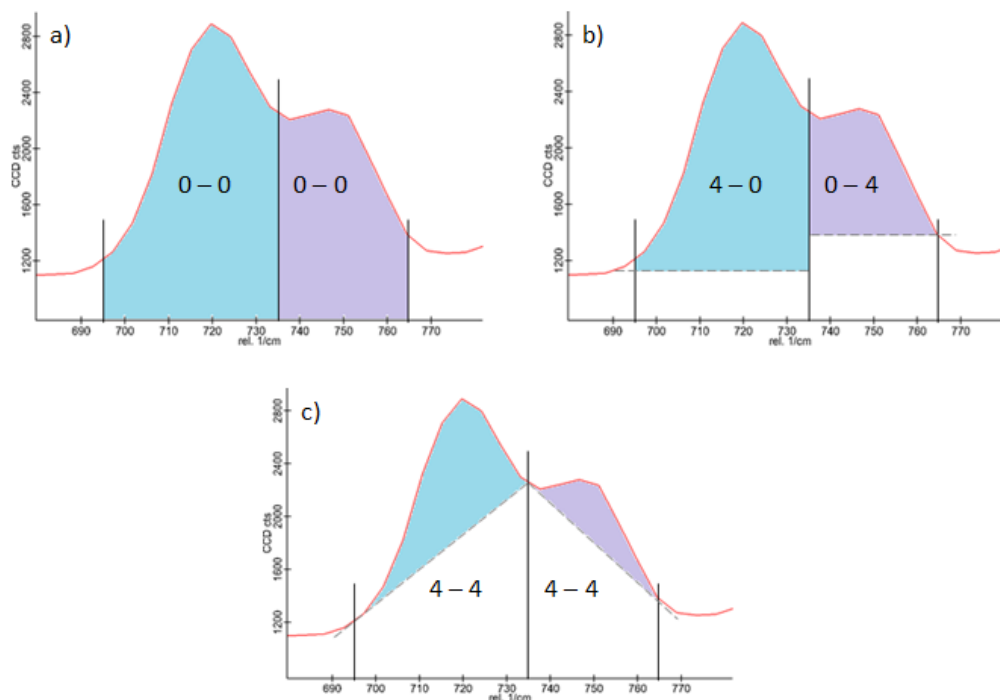
Figure 1.12: a) No background removal (0-0), **b)** One-sided background calculation from 4 pixel (4-0, 0-4 resp.), **c)** Two-sided background calculation from 4 pixel

Univariate Image Generation

If one peak in the spectrum is regarded as one variable, although in reality it spans several wavelengths, the intensity of that peak can be calculated. This can be done by integrating over the whole peak, thereby obtaining the area, or for example by measuring its height. Depending on what is represented, different structures can become visible. This essentially is Raman imaging - scannin of a sample and representation of one variable in space for visualization of the image.

In case of an intensity image, be it height or area, it is important to choose well the baseline, especially in the case of quantitation. Effects such as peak shape, vicinity of the peak and residual fluorescence should be considered. Even though it is more important that the method for the determination of the baseline (point) is the same, rather than its absolute position [53]. The WITec software offers the possibility to quickly calculate the area of a peak, by integrating over all the CCD values recorded in the selected spectral range. The user marks the peak by hand, and can define if the background should be removed or not. If yes, the number of pixel outside the peak range can be chosen that will be used to calculate the average background on each, or just one side (the integration limits). Depicted in Fig. 1.12 is an example of the effect of the integration limits, with zero and four pixel as an example.

Of course, the result of each approach will be different, and the choice of which one to choose is difficult. Including the whole background, as in **a)**, is only a suitable choice, if the background in all spectra is approximately at the same height. This can only be ensured, if an appropriate background correction has been made. Approaches **b)** and **c)** both use the 4 pixel after the black line and subtract

the area below. In my opinion this approach is difficult to control because variations in peak intensities of neighboring peaks or even appearance of new peaks in the vicinity might change the baseline point so much, that no comparison can/should be made. A way to weaken this problem, and also recommendable in approach **a)**, is using peak ratios, if the data are not noisy [5].

Multivariate Image Generation

After performing a multivariate analysis, be it a PCA or a KMCA, the results of the analysis can be represented as an image, the information content being different than in the univariate case.
For instance, all the pixel belonging to the same cluster obtained by KMCA can be assigned the same color and an image can be constructed. The WiTec software gives the additional choice of a color scaling that represents the cluster affiliation.
But also the PCA results can be used to visualize the data. The case scores of each principal component can be plotted as an image, and thereby its distribution can be visualized. The response variable scores, in this case peaks, can also be integrated, similarly to the univariate approach described above.

1.4.4   Peak Assignment and Localization

Even though pectin spectra are very complex, showing many vibrational modes, several authors [20, 25, 57] have attempted to assign some of the peaks to chemical groups or specific domains found in pectin, while others just mention certain peaks [48, 59]. The above mentioned studies used different Raman techniques and different excitation wavelengths than in this work and it is thus possible the peaks have slightly different shifts. Also, the spectra were recorded in different types of cells, dried films or dried powders.

In their work, Himmelsbach et al. [25] recorded NIR-FT-Raman spectra of pectin in different chemical states, that is, the acid, the salt and the methylated form as powders and the dried Ca-crosslinked form. They defined several peaks that serve as markers for the differentiation of the former three forms. Synytsya et al. [57] made a detailed assignment of the vibrational modes associated with the peaks seen in pectic acid, potassium pectate and pectinates of various degrees of methoxylation, degrees of acetylation (DA) and mixed forms thereof. They collected and defined markers for the differentiation of Methyl- and Acetyl-esters of pectin. They also studied the behavior of the skeletal vibration band of the pyranoid ring around 855 rel. cm^{-1} in all of those forms in dependence of the DE. In table 1.1 the defined markers and their assignment according to Himmelsbach et al. [25] and Synytsya et al. [57] are listed, if relevant to the here presented spectra. Most of the marker assignments are consistent, except for the exact wavenumbers and and some assignments.

For instance, there is a discrepancy in the methyl-pectate assignment. Synytsya et al. [57] detected two peaks at 2960 and 2860 cm^{-1} and assigned them to an asymmetric and a symmetric stretch of

the methyl C-H bonds, respectively. On the other hand, the spectra of Himmelsbach et al. [25] do not show any peak at either position, instead the C-H$_3$ vibration was assigned to the band at 2891 cm^{-1}. The peak at 1455 cm^{-1} also has an ambiguous assignment in the literature, that is, it is assigned to the C-O stretching of the methyl-ester group in [59] and to the (asymmetric) C-H bending of the same group in [48], [57] and [25].

Also, the assignment of the 855 cm^{-1} band is not consistent. Himmelsbach et al. [25] adopted the assignment from Séné et al. [48], assigning only the asymmetric C-O-C stretch of the glycosidic linkage to this band. Synytsya et al. [57] in turn extended this assignment to a skeletal vibration involving both, the glycosidic linkage and the C6 carbon. According to the authors, the vibration involves the positions C6-C5-O5-C1-O1 and is thus sensitive to C-6 modifications, but apparently also to acetylation of the C-2 and C-3 hydroxyls [57]. This would explain why this band is sensitive to the substitution pattern of pectin, since it is closer to the site of substitution. Synytsya et al. [57] instead assign a band at 1145 cm^{-1} to the stretching of the glycosidic bond, which also corresponds to the assignment in [20].

Table 1.1: Collection of peaks found in different forms of pectin. The peak positions and assignments by Synytsya et al. [57] and Himmelsbach et al. [25] were compared.

Pectin Form	Wavenumber / cm^{-1} Assignment as in Himmelsbach et al. [25]	Wavenumber /cm^{-1} Assignment as in Synytsya et al. [57]
Pectin General	$\sim$ 2940 - ν(C-H) of galacturonates not seen	2941 - 2945 - ν(C-H) 1050 & 1030 - ν(CC)(CO)
Polygalacturonic acid	1743 - ν(C=O)$_{COOH}$ 1327 - not assigned 1248 - not assigned 1141 - not assigned 1077 - not assigned 851 - ν_{as}(C-O-C)$_{glycosidic}$	1740 - ν(C=O)$_{COOH}$ 1330 - δ(C-H) 1254 - δ(C-H) 1145 - ν(COC)$_{glycosidic}$ 1079 - ν(CO)+ δ(OH) 853 - (C6-C5-O5-C1-O1) skeletal vibration
Pectate (salt) Ca-salt [25] K-salt [57]	1605 - ν_{as}(COO$^-$) 1415 - ν_s(COO$^-$) 1245 - not assigned 1140 - not assigned 1080 - not assigned 856 - ν_{as}(COC)$_{glycosidic}$ 814	1607 - ν_{as} 1405 - ν_s(COO$^-$) 1242 - δ(C-H) 1144 - ν(COC)$_{glycosidic}$ 1078 - ν(CO)+ δ(OH) 857 - (C6-C5-O5-C1-O1) skeletal vibration 814 - γ(C-OH)$_{ring}$

Table 1.1: Collection of peaks found in different forms of pectin. The peak positions and assignments by Synytsya et al. [57] and Himmelsbach et al. [25] were compared.

Pectin Form	Wavenumber / cm^{-1} Assignment as in Himmelsbach et al. [25]	Wavenumber /cm^{-1} Assignment as in Synytsya et al. [57]
Me-Pectate	Not seen 2891 - ν(C-H)$_{CH_3}$ 1747 - ν(C=O)$_{COOMe}$ 1459 - δ(C-H)$_{CH_3}$ 1343 / 1324 - not assigned 1270 - not assigned 1074 - not assigned not seen not seen 849 - ν_{as}(C-O-C)$_{glycosidic}$ lower intensity	2960 - ν_{as}(C-H)$_{CH_3}$ 2860 - ν_s(C-H)$_{CH_3}$ 1750 - ν(C=O) 1458 - δ_{as}(C-H)$_{CH_3}$ (1440 for acetyl ester) not listed 1260 - ν(COC) not listed 922 - δ(C-H$_3$)$_{Me-ester}$ 928 - δ(C-H$_3$)$_{Ac-ester}$ 852-862 - depending on DM/DA
Neutral sugars	2983 / 2894 - xyloglucan / xylan 1268 - arabinan, acetylated glucomannan 1121 - pectic galactan 937 - pectic galactan	not investigated
Rhamno-galacturonan I	1455 - not assigned 1137 - not assigned 1080 - not assigned	not investigated

Table 1.1 demonstrates the difficulty in finding a reference peak with constant wavelength, since most if not all peaks shift slightly depending on the backbone and subunit constitution. For instance, the skeletal vibration at 855 cm^{-1} is a rather prominent peak (especially in the powdered form, for example see [25]) and its frequency is located between 850 and 862 cm^{-1}, depending on the DM and DA, as well as on being the salt- or the acid-form. Also, methyl-esters tend to result in a lower shift than acetyl-esters. Similar conditions apply to almost all other peaks as well.

Furthermore, in table 1.2 some peaks from other substances, such as water and fatty acids, were added from various sources.

In Figure 1.13 the peaks found in the spectra of this work are shown using the spectrum of Polygalacturonic acid as an example. Those peaks that were not found in the references regarding pectin were marked in bold. A detailed discussion of the spectra can be found in sections 3.2, 3.3 and 3.4.

Table 1.2: Collection of peaks from several compounds possibly relevant to the recorded spectra.

Material	Peaks / cm^{-1}	Assignment
Water	$\sim$ 3020 - 3720	ν(O-H) stretching region, dominated by H$_2$O stretching when present [6]
Iso-propanol	818	ν(C-O) [61]
Various fatty acids	$\sim$ 1655 (s)	ν(C=C) [18]
	1440 - 1450	ν(C-C), δ(CH$_2$) twisting and deformations, δ(CH$_3$) deformations [18]
	1002 (w)	Methylhexadecanoic acid [18]
	1010 (w)	15-Methylpalmitic acid [18]
Lignin	1660	ν(C=C) [21]
β-D-Glucose	1002 (mw)	- [18]
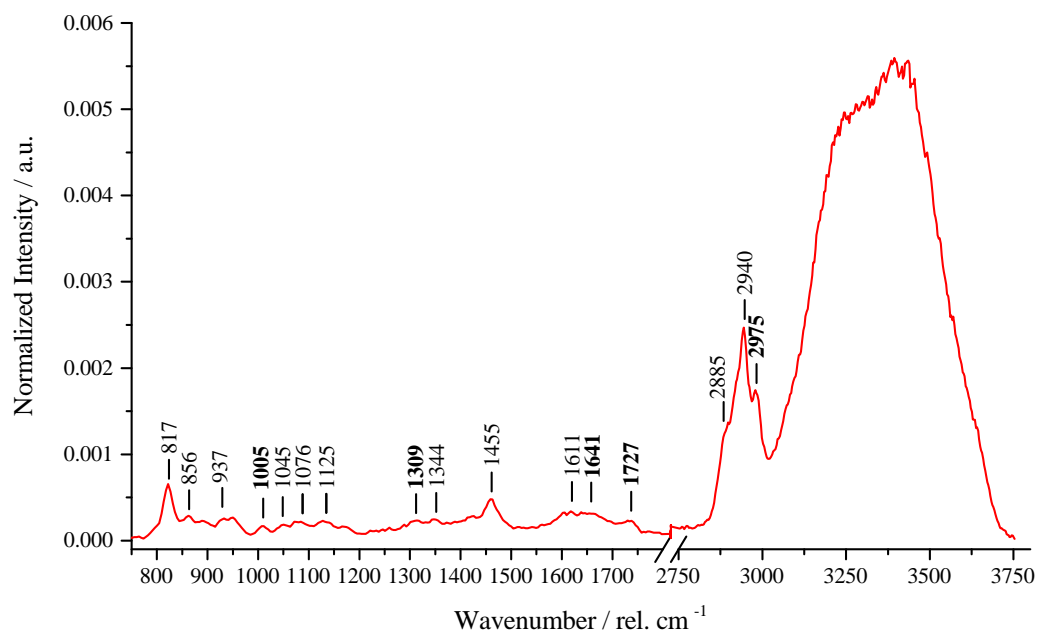
Figure 1.13: The most relevant peaks found in pectin are indicated using the poly-galacturonic acid solution spectrum. The peaks marked in bold (at 2975, 1730, 1641, 1305 and 1005 cm^{-1}) are not discussed or present in the literature in relation to pectin. At 817 cm^{-1} the propan-2-ol (ISTD) can be seen and is only present in extracted pectins.

Chapter 2 – Materials and Methods

2.1 Pollen

2.1.1 Materials

Pollen was collected from flowering *Lilium longiflorum* bought in spring from local shops. Some specimen was used immediately and the rest frozen at - 18 °C for later use. For germination the growth medium LPMG according to McKenna et al. [35] was used: 7 % (w/w) sucrose, 0.1 mM $CaCl_2$, 1 mM KCl, 1.6 mM H_3BO_3 and 15 mM MES-buffer. Then the pH was adjusted to 5.6 with NaOH. All these materials were kindly provided by Lawrence J. Winship [65, 66].

2.1.2 Sample Preparation

A spatula tip of pollen was transferred into an Eppendorf tube and 1 ml LPGM added. Since the pollen needs a lot of oxygen to grow, the tube was gently shaken by hand for approx. 2 hours, taking care not to warm the medium too much.

Before Raman imaging, the state of the pollen was verified under the light microscope (glass slide and cover). If satisfactory, the pollen was osmotically shocked by increasing the sucrose concentration to 12 %, otherwise no image could be taken since the pollen would "grow out of sight" In order to get a good spectral view on the pollen, the high sucrose had to be washed out before imaging. For this purpose, the Eppendorf was shortly centrifuged at 135 rpm, the supernatant discarded and the pollen re-suspended in water (repeat 3 - 4 x).

For the measurement itself, a drop of the pollen suspension was entrapped between a conventional glass slide for microscopy and a cover glass slide. All the edges of the cover glass where carefully sealed with nail-polish to avoid loss of water.

2.2   Pectin

2.2.1   Materials

Table 2.1 shows all the used pectins, including their abbreviation for the rest of this work. Four HMPs, one of which is a pectin extracted from apple and three LM pectins from citrus fruits were used, including two potassium salts. Polygalacturonic acid was also included as sample for the backbone vibrations.

Table 2.1: Specifications of pectin samples and PGalA. The sample code designates the names of the samples throughout this work. The shaded rows are LMPs (DE < 50 %), others are HMPs, except PGalA which represents the homogalacturonan.

Product name	Sample code	GalA [%]	DE [%]	Source	Provider	Product #
Genu®pectin type LM 12 CG-Z	GenuLM12	94.5	34.4	citrus	CP Kelco	113681
Genu®pectin type D slow set-Z	GenuD	89.9	65.2	citrus	CP Kelco	114879
Genu®pectin type B rapid set-Z	GenuB	86.6	70.7	citrus	CP Kelco	113075
Polygalacturonic acid (95 % enzymatic)	PGalA	92.3	0	-	Sigma-Aldrich	81325
Pectin Apple	HMPA75	-	70.8	apple	Sigma-Aldrich	76282
Pectin from citrus peel	LMPC7	84.1	8.2	citrus	Sigma-Aldrich	P9135
Pectin, esterified potassium salt	LMPC34K+	66	26	citrus	Sigma-Aldrich	P9311
Pectin, esterified potassium salt	HMPC70K+	74	62	citrus	Sigma-Aldrich	P9436

For the preparation of all solutions 18 MΩ de-ionized water (MQ-water) was used. Other chemicals used for pectin and/or PGalA solutions were: iso-propanol (ACS grade, Reag. Ph. Eur. - VWR Chemicals); sodium hydroxide (99.0 % - ACM Chemicals); hydrochloric acid (analytical reagent grade - VWR); calcium chloride di-hydrate (meets USP testing specifications, Sigma-Aldrich), di-sodium-hydrogen-phosphate monohydrate (ACS grade, $\geq$ 99.0 % - Fluka). Deuterium oxide (99.90 % - Euriso-top); Amorphous CaF_2 crystals (Hellma Materials) and silizium-wafers were tested as internal standards.

2.2.2 Sample Preparation

Several procedures for the preparation of a pectin solution, the choice of an internal standard, as well as sample mounting were varied and the best used for the whole series of pectins. For each procedure an HMP and an LMP was used, in order to find out, if the procedure works in both cases and to minimize differences in sample preparation. Furthermore, procedures for the Ca2+-crosslinking of the LMP solutions were sought. Also, a method for the preparation of a PGalA solution was sought out. The best procedure should be the one that would allow the preparation of the solutions and gels using the mildest possible conditions, that is, to avoid heating, in order to mimic the conditions in the pollen tube. The use of buffers was avoided in most trials, because of the possibility of interference with the spectra and the fact that the exact composition of the pollen tube cytosol is not known, although it would have been appropriate. Only the results of the successful experiments are presented in section 3.

Selection of an internal standard

The qualities the internal standard (ISTD) should have were chosen as follows: Easy handling, no chemical reaction with the sample, no peak interference with the pectin spectrum and the peak(s) itself should have constant intensity. Candidates were CaF_2 crystal, Si-wafer and D_2O because their spectra do not interfere with the pectin spectrum. The CaF_2 was dismissed because of potential ionic interactions with the pectin chains and the difficulty of sealing well the glass covers or finding any other measurement cell that would fit the purpose. For the latter reason the Si-wafer was also dismissed. D_2O was a better candidate, being easier to handle. On the other side, the potential hydrogen-deuterium exchange with the acidic hydrogen atoms in pectin is an effect that could manipulate the spectrum and would thus need more experiments to assess its impact on a Raman spectrum. Also, this effect is likely dependent on the class of the pectin and the pH.

After further investigation, a pectin preparation procedure was found in literature [31] that uses iso-propanol as dispersing agent (see below), which is equally handy as D_2O and has no peaks interfering with the pectin spectrum. As opposed to the pre-selected candidates, iso-propanol plays two roles at the same time, making it the best ISTD for this system.

Measurement Cell

There are several requirements for the measurement setup of the sample. As the samples, pollen and pectin, are measured in water, the measurement cell must be air-tight in order to avoid desiccation caused by the heat generated by the laser. Furthermore, because of the inherent depth dependence of the signal due to the confocal microscope, it is of advantage to have a defined sample height in order
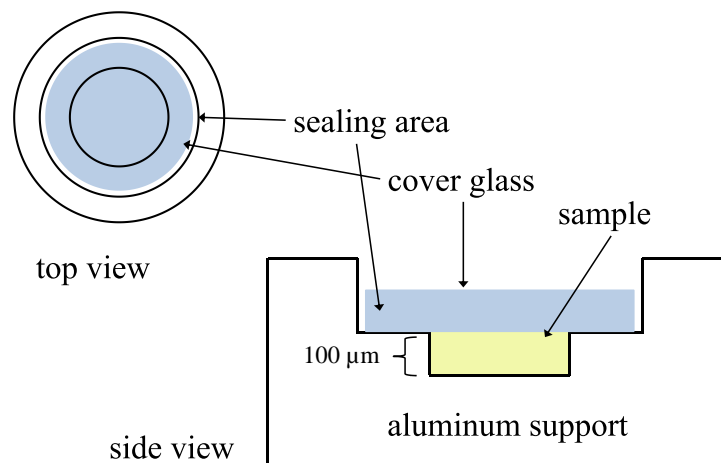
Figure 2.1: Top view and profile of the designed measurement cell with defined depth and easy sealing.

to avoid too big intensity differences, especially in the case of the pectin samples. Also, this reduces the need for data manipulation prior to the actual analysis.

Initially the pectin solutions were measured in between glass slide and cover slip as for the pollen tubes. Due to the difficulty of sealing the CaF_2 crystals (height 2 mm), as well as the Si-wafers, a circle was cut into a plastic plate and a big cover slide glued to the bottom with nail polish. Then the ISTD was placed into the chamber, the rest filled up with pectin, and the chamber was then carefully closed and sealed with another cover glass, always taking care to not enclose any air bubbles. These setups were used only in the preliminary experiments, and had the problem of being too deep without a solid ISTD, leading to issues with knowing the position within the sample and signal intensity because of the confocal setup. Mostly a piece of aluminum foil had to be placed under the measurement cell in order to be able to find the focus.

This lead to the design and realization of a measurement cell made of aluminum according to the scheme below (Fig.2.1). A depth of 100 μm was chosen for the central ring, because a shallower chamber showed signs of evaporation. The resulting sample volume is about 7.8 μl. After the sealing area was brushed with a thin layer of nail polish, a drop of pectin was placed into the central department and the cover glass carefully placed on top. The borders were equally carefully pressed on, while excess of sample was pushed out. After cleaning the excess, the space between the cover glass and the support was filled with nail polish and allowed to dry. This setup allowed finding the focus easily and having a defined sample height.

Unsatisfactory Procedures

- Pectin:

    - 1 ml MQ-water was heated to 50 °C, 2 % (w/w) LMPC7 added and left to stir for 30

min. The solution was cooled and sealed between glasses, as described above for the pollen. From the same solution another sample was prepared where a piece of Si-wafer was co-entrapped in between the glasses. The procedure was dismissed due to high inhomogeneity of the sample and difficulty of sealing due to the big height difference.

– 1 ml MQ-water was heated to 80 °C, and 6 % (w/w) pectin added under stirring. The solution was stirred at 100 °C for 20 min, then at 80 °C for another 20 min and left to cool to *RT*. The spectra showed no peaks due to high fluorescence, hence the procedure was dismissed.

- Poly-galacturonic acid:

    – To 1 ml of a 0.5 M NaOH solution, 5 % (w/w) PGalA was added under stirring. The turbid suspension turned yellow immediately, but became white again after some time of stirring, without dissolving. Therefore, the suspension was heated to 50 °C, but this did not help either. The spectrum showed fluorescence only.

    – The above procedure was repeated with a 0.1 M NaOH and heating to 80 °C, which resulted in a yellow suspension, showing high fluorescence in the spectrum.

Satisfactory Procedures

- Pectin:

    – 10 - 60 mg of pectin (HMs and LMs) were wetted with 100 µl iso-propanol and 900 µl MQ-water added under stirring. Then the beakers were sealed with parafilm and adhesive tape and left to stir for 24 h at 500 rpm (LMPs) and 300 rpm (HMPs).

- Poly-galacturonic acid:

    – 50-60 mg of PGalA (= 5-6 %) were wetted with 100 µl iso-propanol (65 %) and 0.5 ml MQ-water added under stirring. Then, 1 M NaOH was added in 10 µl steps under vigorous stirring until the PGalA dissolved (a total of 150 - 160 µl was needed), which resulted in clear viscous solution. Finally, MQ-water was added to reach 1 ml and the solutions left to stir for at least 1 h.

    The amount of NaOH needed corresponds to 0.15 M and similar amounts were later found in other publications [37, 58]. These samples were only measured four days after sample preparation, and no precipitation occurred. (Without the addition of NaOH the solutions precipitated after some days.)

    – The procedure used in Stoddart et al. [54] was also adapted although it makes use of a buffer, because its concentration was so low, that no interference with the spectrum was found. A 0.1 M Na_2HPO_4 buffer was made and its pH adjusted to 6.5. To 20-30 mg of

PGalA 100 μl iso-propanol (65 %) were again added as dispersing agent and ISTD. Then, 900 μl of the buffer were added under stirring. This procedure was fine for a 2 % (w/w) solution, but 200 μl of 0.5 M NaOH had to be added to the 3 % solution after about 1 h, because of re-precipitation. The solutions were left to stir for 24 h.

Cross-linking with Ca^{2+}

All cross-linking experiments were done using GenuLM12®and the calcium solutions were prepared from a 0.5 M CaCl$_2$.2 H$_2$O stock solution. Although none of the procedures led to a uniform gel, some samples could be used for comparison and will therefore be presented in the results. The R values were calculated according to equation 1.1, but cannot be assumed to be true values, due to the inhomogeneity of the mixtures.

- Unsatisfactory Procedures

    - Dissolving in CaCl$_2$: 20 mg of pectin were wetted with 100 μl iso-propanol and 1 ml of 39 mM CaCl$_2$ solution added under stirring (R = 1.2). The mixture was left to stir for 1 h and allowed to set until the next day. A clumpy precipitate was the result.

    - Diffusion: Again 1 ml of a 4 % solution was prepared as in the previous case, but the 1 ml 39 mM Ca-solution was poured over the pectin and allowed to diffuse for 1 h (R = 0.6). Using a spatula, a layer of the surface was sampled, later a deeper layer - only fluorescence was observed in both cases.

    - Dilute to 3/4: A 2 % pectin solution was prepared using 100 μl of iso-propanol, 900 μl of water and stirring for 1.5 h. Then 500 μl of a 6 mM Ca-solution were added and the mixture stirred for 30 min (R = 0.04). Again, strong fluorescence led to the exclusion of this experiment from further analysis.

- Satisfactory Procedures

    - Mix Powders (T1): 20 mg of GenuLM12 were mixed with 4.5 mg of CaCl$_2$ in the powdered form, then 100 μl of iso-propanol were added, followed by 900 μl of water under stirring (R = 1.3). The mixture was left to stir for ∼ 4 h. Nothing resembling a gel could be observed, nevertheless images of a bigger clump were made and analyzed further.

    - Dilute to half (T2): A 4 % GenuLM12 solution was prepared according to the satisfactory pectin procedure (except stirring for only 1 h). Then 1 ml of a 39 mM CaCl$_2$ solution was added under stirring (R = 0.6). Clumps formed immediately and the mixture was left to stir for 3 h. Also this trial was investigated further.

    - Dilute to half and stir (T3): A 4% GenuLM12 solution was prepared as in the previous point and left to stir over night. The next day, 1 ml of a 8 mM calcium solution was added and allowed to stir for another 24h (R = 0.03). The result was investigated further.

2.3 Apparatus and Measurements

2.3.1 Apparatus

For this work, the Witec GmbH alpha300 A confocal Raman microscope with 532 nm excitation wavelength was used. In the picture below (Fig.2.2) a schematic representation can be seen (adopted from [67]). The function of the individual elements are listed in the table below and the role of the most important parts has been elucidated in section 1.3.3, p. 21 [67].
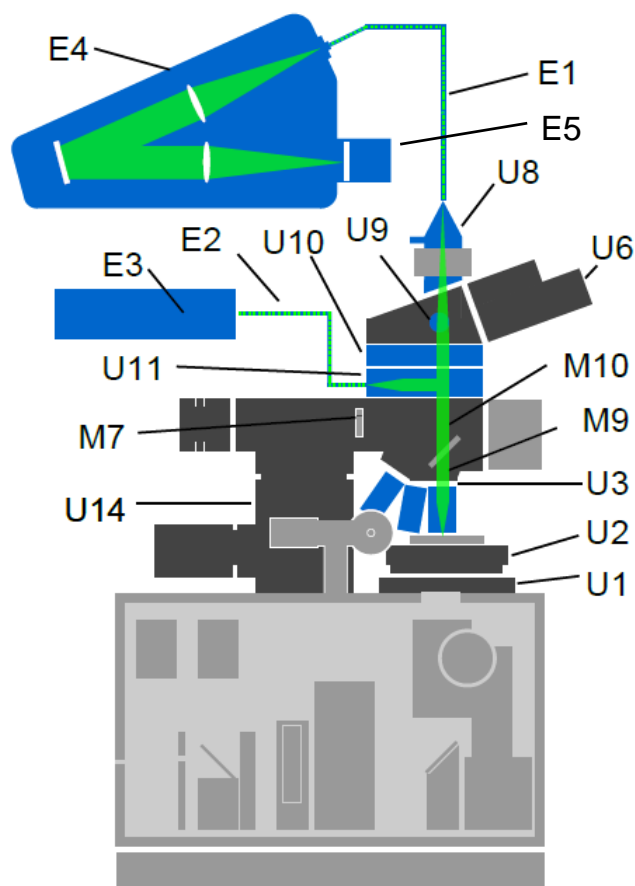
Figure 2.2: Scheme of the confocal Raman setup used in the alpha300 model by Witec GmbH. The light path is shown in green [67].

2.3.2 Measurements

At the beginning of each measurement day, the spectrometer was calibrated using a Si-wafer. For this purpose, the instrument was run in oscilloscope mode and the excitation wavelength adjusted in the (sub-)decimal range until the most prominent Si peak was located around 521 rel. 1/cm (521.2 $\pm$ 0.25 rel. 1/cm on average).

Table 2.2: Functions of the elements of a representative confocal Raman setup built by Witec GmbH, as shown in 2.2. Specifications concerning the specific alpha300 model used in this work are given in brackets.) Witec

Element	Function
U1	XY positioner
U2	Scan stage
U3	Objective turret with objectives
U6	Binocular tube with ocular camera
U8	Fiber coupling unit optical output
U9	Pushrod
U10	Filter slider unit
U11	Laser coupling unit optical input
U14	Microscope Z stage with stepper motor
M7	Field stop diaphragm
M9	Objective turret
M10	Reflector slider
E1	Multi-mode optical fiber (25, 50 & 100 µm)
E2	Single-mode optical fiber
E3	Laser (532 nm)
E4	Spectrometer USTH 300 (gratings 600 g/mm & 1800 g/mm, Peltier cooling, -70 °C)
E5	Detector DV401A-BV352 (CCD camera, 1024×127 pixel, 26×26 µm/ pixel)

For the extracted pectins the laser power was adjusted to the maximal power of 26 mW, while the pollen tubes were measured at 10 mW. All spectra/images were recorded using a Nikon 60x oil-objective (NA = 0.8, WD = 0.3, ∞/0.17) with Leica immersion oil (n_e^{23} = 1,518), which results in a lateral resolution of 0.4 µm. Due to the confocal setup, any sample under the microscope had to be focused in light-microscopy mode. For the 60x oil objective this results in an axial resolution of 1.6 µm. In order to find the focus more easily a piece of aluminum foil was placed under the glass slide of the pollen samples. In case of the pectin solutions, the chamber itself took over that role.

For the pollen tubes, the Zeiss EPI PLAN 20x objective (NA = 0.4, WD = 3.1, ∞/0) was used to locate the pollen in normal light microscopy mode, and then taking care not to lose the position, the 60x oil objective was used for imaging in one plane (x-y) The 100x objective could not be used, because it was impossible to find the pollen again in the imaging modus. The size of the image depended on the parts of the pollen imaged, the spacial resolution (number of spectra per µm) was rather experimental and the integration times varied between 0.5 – 2 s. For quick visualization of the image the CH or OH vibrations were integrated and the resulting intensity represented over the image space.

The pectin solutions were imaged in the x-z direction, because the signal changes with depth in a confocal setup, and the focus is never at the exact same height. In order to make the spectra comparable this measure was necessary. To do so, the images were recorded starting at the bottom of the cell, were 20 spectra were taken per layer (1 spectrum/ µm) until reaching the cover glass. This relatively low spatial resolution was chosen because of the inhomogeneity of the samples – to get a better representative average. The samples of the cross-linking trials were imaged in stacks, that is areas of 50 µm^2 per 1-3 layers , a the distance of 20 µm between each layer and 2 spectra/µm. Quick visualization was again performed using the intensities of the CH and OH vibrations.

2.4   Data Analysis Methods

The entire data analysis, including all pre-processing steps, was performed with the WiTec Project Four Plus$^{©}$software and the extracted values further compared using Origin$^{®}$9.1 Pro.

2.4.1   Preprocessing

Cosmic Ray Removal

The spectra were corrected for cosmic rays using the following parameters: Filter size: 2
Maximum number of cosmic rays (per spectrum): 2
Dynamic factor: 8
Interpolation: linear from neighboring pixels

X-axis adjustment

Due to the calibration of the spectrometer every day, the wavelengths assigned to the 1024 pixel of the x-axis did not completely correspond to each other. As a result the spectra were slightly shifted relative to each other and the overall spectral resolution, that is the resolution when including several days of measurement, was actually lower than the resolution of the spectrometer itself. Therefore, all spectra were re-calibrated to the average excitation wavelength calculated from all the measurement days with the WiTec software. The software then adjusts all the wavenumbers of the spectrum according to this value.

Background correction

The WiTec Project Four Plus ©software provides a tool for correcting the background of spectra and images. To find out which spectral mask and order of the polynomial should be used, a representative 1 layer image of an extracted pectin and a representative pollen image were used and a median filter (Median 3: spectral filter size 1; spatial filter size 0) was applied on them in order to reduce the noise in the data. Please note that no smoothing was applied during the actual analysis. The reason for using so different samples was that all the spectra should be background corrected with the same mask and order, if possible.
An auto-polynomial function was used, which avoids negative intensity values depending on the noise threshold. After some trials, slightly different masks were used for the pollen and the pectin images. The respective background was then fitted with polynomials of orders 3 to 6 with 0 noise threshold (no negative values) and an additional polynomial of 3rd order with noise threshold 2 (baseline can have negative values). From here on the designation of the polynomials will be Poly x,y, where x is the order of the polynomial and y the noise threshold.

Two very different ways how to test which auto-polynomial best describes the background were used in order to have a double check-up. The goal was to find the polynomial that least influences the spectrum and so the condition was that the 'right' polynomial would be the one that gives the results closest to the uncorrected spectrum.

- PCA:
  A PCA was performed separately on the uncorrected and each of the corrected versions of the pectin and pollen images. The Rayleigh peak was excluded, since it would influence the PCA substantially and is not of interest here. The rest of the whole spectrum was used, including areas without peaks, in order to certainly capture background contributions. A minimum/maximum filter was used to calculate the percentile eigenvalues. Theoretically, the total variance of the extracted pectin's image should be smaller than that of a pollen image, since the pollen image should show very different spectra, while the extracted pectin image should
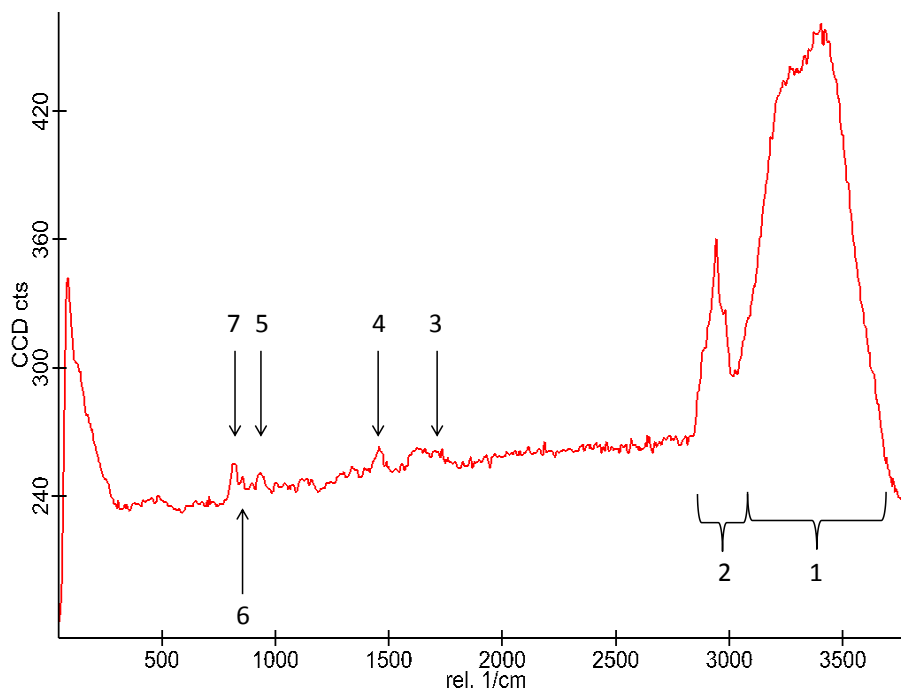
Figure 2.3: Exemplary uncorrected spectrum with arrows indicating the peaks that were chosen for the evaluation of the best background correction polynomial. Peak no. 7 was not used for the pollen, as it corresponds to the internal standard, and was thus not present in the pollen spectra.

have very similar spectra. Thus, if a polynomial order works well for both types of data, it indicates that it is appropriate. For this purpose, the loadings of the principal component axes were inspected, as well as their eigenvalues. The first seven axes were chosen for comparison.

- Peak contribution:
Seven prominent peaks of different size were chosen (see Fig. 2.3) and their intensities calculated for each of the images. The intensities were summed up and the percentage of each peak to the total was determined. Finally, the ratios were sorted and the polynomial(s) closest in ranking to the uncorrected peaks got 1 score. The polynomial with most scores was determined to be the most appropriate.

After assertion of the right polynomial, all the pectin spectra could be corrected using the same mask. In the case of the pollen, most images were corrected using the same mask, but for some the mask had to be slightly adjusted. In one case a cluster analysis had to be performed prior to background correction, because the background in different parts of the image was so different that different masks had to be used.

Data cropping

Before any further analysis, all the spectra had the Rayleigh peak and the upper spectral end removed, the new spectral range being $\approx$ 30-3850 rel. 1/cm. This was done in order to reduce the amount of data and to not include any effects of the Rayleigh scattering in subsequent steps.

Pollen

Many pollen images were recorded, while only six of them were used for the analysis. Using the Witec ProjectPlus$^{©}$, the pollen spectra were all normalized according to formula 1.14, p. 26. As mentioned in section 2.3.2, the pollen images had to be recorded at low intensity and integration time. For this reason, the spectra were much noisier as compared to the pectin spectra and hence, a preliminary PCA was performed in order to reduce the noise. A mask containing the spectral regions 300-1800 rel. 1/cm (for convenience called 'fingerprint region' in this work) and 2750-3050 rel. 1/cm (CH vibrations) were used for this purpose, and the first 10 principal components were selected for the output. The thereof resulting reconstructed spectra were used for the spectral analysis.

Pectin

Since the pectin samples could be measured with much higher laser power and integration time, no PCA was performed for noise reduction. Because the pectin images included regions of glass, as well as spectra where the sample burned, each of the pectin images was subjected to a cluster analysis in order to pre-select the data. For the root cluster options a data reduction factor of 10 was used, with data pre-transformation mode 'derivative', Manhattan normalization, Euclidean distance and k-means clustering mode. Additionally, a spectral mask was created that spanned the fingerprint region in order to differentiate well glass regions from pectin, as well as sort out burned or noisy spectra. Furthermore, creating 5 clusters from the root cluster showed the best discrimination. Finally, for each sample the clusters showing the clearest signals were selected and the average was calculated for further analysis. The resulting average spectra were normalized in the same way as the pollen spectra in order to eliminate intensity differences between the samples.

2.4.2   Analysis of Pollen

The now de-noised pollen images were subjected to cluster analysis in order to separate the different cell compartments. The same root cluster options as for the pre-selection of the pectin spectra were used: data reduction factor of 10, with data pre-transformation mode 'derivative', Manhattan normalization, Euclidean distance and k-means clustering mode. Here, the fingerprint and the CH vibration region were analyzed and 4 primary clusters were formed. If necessary, further clustering

was done for refinement. When satisfactory, the clusters representing vesicles and wall were extracted and analyzed separately with PCA in order to extract information that is specific for the wall and/or the vesicles. With the goal of determining specific peaks for wall and vesicles, performing a "mixed PCA" (over the whole image) would not make sense, because of the different sample number, that is, image pixel representing the wall and the vesicles [3]. Nevertheless, the image representation of the eigenvalues (called transformed spectrum in the WiTec software) can give some information about the weight of the loadings in the imaged space.

An overall average spectrum was calculated from all the samples, one for the wall and the vesicle clusters of the KMCA, respectively. This was done in order to reduce further the number of spectra used for the determination of the peak positions. The wall average spectrum was made only from clusters containing both tip and shaft. Although the eigenvectors of all wall and vesicle clusters showed very similar shape, respectively, the absolute scores were not the same and hence no average was calculated from them.

The eigenvectors were compared to the peaks seen in the overall average spectra, because, according to theory, they show the relative contribution of different substances, and thus can clearly show peaks that are only seen as shoulders or part of broader peaks in the average spectra.

The peak positions were determined using the automated peak finding algorithm provided by the WiTec Project Four Plus [©]software.

2.4.3 Analysis of Pectin

The average spectra resulting from the cluster analysis of the pectin samples and the calcium-pectin samples were overlaid and the peak positions compared. The peak positions were again determined by WiTec peak finding algorithm.

2.4.4 Comparison of Pollen and Pectin

The areas of the C-H and O-H stretching peaks were calculated using an integration limit of 0 - 0 and the ratio of CH to OH calculated. The samples were sorted in ascending or descending order of their respective intensities in order to assess their information content. Finally, the peak positions extracted from the pollen and the various pectin samples were compared.

Chapter 3 – Results and Discussion

3.1   Background Correction

The eigenvalues calculated by the PCA for the pectin image are shown in the table below. The first axis of the poly6,0 had the highest explanatory power. Additionally, an interesting and reassuring feature of this analysis was, that the second principal component of the uncorrected spectrum corresponded to the first PC of the poly 6,0 version, while the first axis showed mainly fluorescence as shown in Figure 3.1.

Table 3.1: PCA eigenvalues of pectin spectra corrected with different polynomials

	λ PC 0-7	λ PC 0
no corr	98.2	91.6
poly6,0	98.3	91.6
poly5,0	99.2	88.9
poly 3,0	99.3	85.5
poly 3,2	99.3	89.2
poly4,0	99.5	88.9

The loadings of the first principal component of the uncorrected spectrum are shown in Fig. 3.1a. They appear to represent the main background signal, thus showing that background fluorescence is the most important influence on the data. Furthermore, it demonstrates the power of PCA to differentiate patterns in the data. It would be interesting to test whether it could be used as a background correction method *per se* or in combination with other techniques, but this is not the focus in this work. Fig. 3.1b shows the second PC of the uncorrected spectrum, which already reveals some peaks in the negative direction, although some residual background contribution can be seen in the positive curvature. Fig. 3.1c shows the first PC of a spectrum corrected with Poly 6,0. The baseline is centered around zero, showing that the background has been removed and additionally has the same orientation as Fig. 3.1b, as opposed to the corresponding loadings of the other polynomials.
For the pollen images, the loadings of the first axis of the uncorrected spectrum explained 97% of the variance, and the closest to this was the poly3,2 version with 95.46 %. Actually the poly 6,0 version was farthest apart from the original data, but the first axis still explained 95.12% of the variance, and
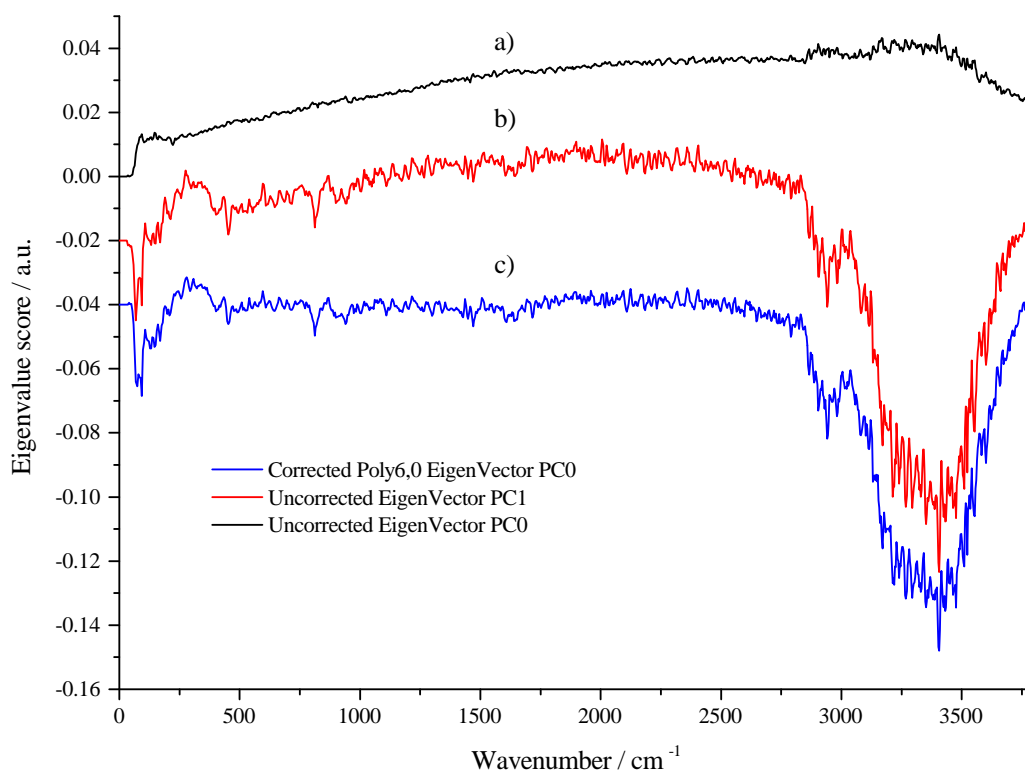
Figure 3.1: Loadings resulting from PCA of pectin samples offset by 0.02 a.u.: **a)** PC 0 of uncorrected spectra shows mainly fluorescence, **b)** PC 1 of uncorrected spectra shows residual fluorescence and peaks,**c)** PC 0 of Poly6,0 has the same direction as b)

the eigenvectors also had the same direction. So, also in this case, although not being the closest result to the original, the polynomial of 6th order is applicable.

The peak contribution test also showed that the polynomial of 6th order fitted best, because for most peaks the percentage of contribution was closest to the uncorrected data, and this in case of the extracted pectin and the pollen image. This was interpreted such that the polynomial of 6th order least distorts the spectrum in the relevant regions. This test also showed that in theory different regions of the spectrum should be fitted by different polynomials, as shape changes can be quite drastic. This finding is the subject of several publications, including [15] and [8].

3.2 Pollen tubes

In Figure 3.2 all the Raman maps of the different pollen samples evaluated in this work are shown by their false color image. This intensity image is generated by integration of the general pectin C-H stretching vibration peak at 2940 cm^{-1}. Figure 3.2a) shows the image of the tip and a small part of the shaft of a pollen tube. The numbers indicate the different compartments: **1** - the cell wall, **2** - the vesicles, **3** - the cytosol and **4** - the medium. Figures 3.2 b and c) show the apex and the shank of the pollen tube, together with a part of the shaft. Figure 3.2 d) is an image focused on the apex of the
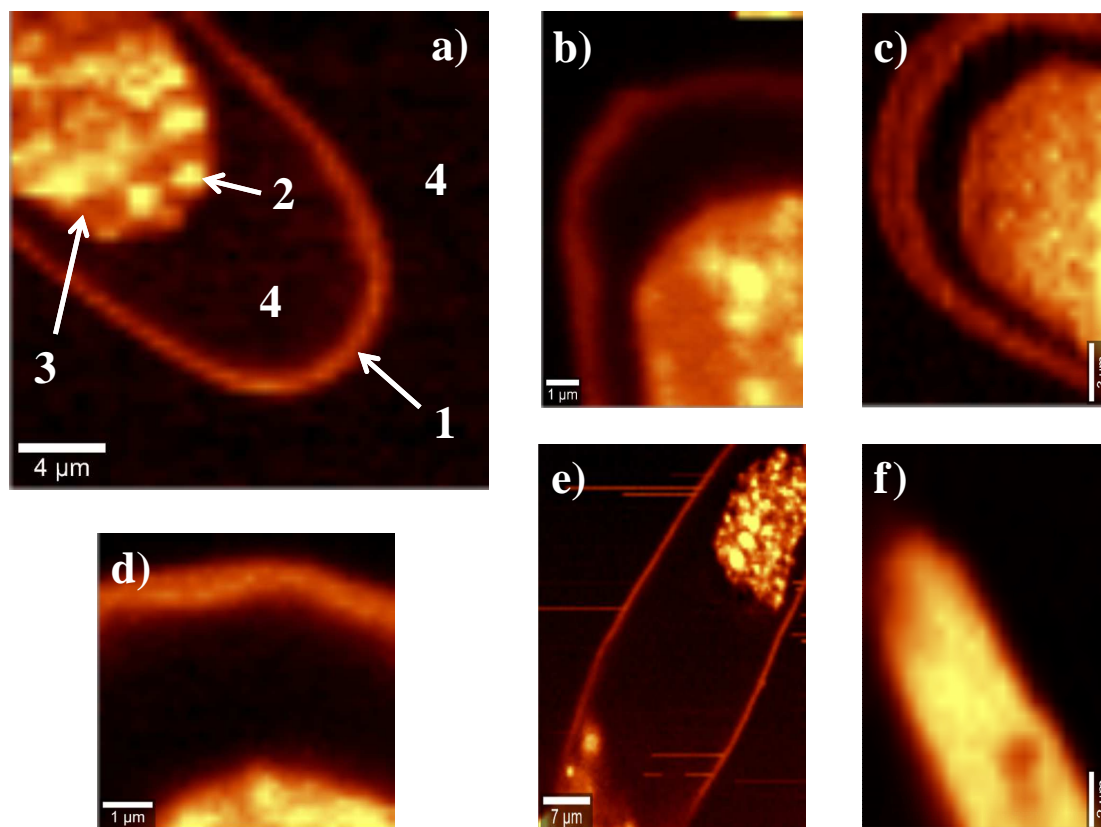
Figure 3.2: False color code Raman images of different pollen samples. The color code is generated by the integrated intensity of the general pectin C-H stretch at 2940 cm^{-1}. Lighter colors (i.e. yellow) represent high intensities, while darker ones (i.e. redish-black) low intensities. The image shows where in the pollen pectin can be detected. **a)** tip and shaft, **1** - cell wall, **2** - vesicles, **3** - cytosol, **4** - medium – scale 4 μm, **b)** tip and shaft – scale 1 μm, **c)** tip and shaft – scale 3 μm, **d)** tip – scale 1 μm, **e)** shaft – scale 7 μm, **f)** tip and shaft – scale 2 μm

pollen tube, where part of the cytosol is visible. Finally, Fig. 3.2 e and f) show mainly the shaft of a pollen tube, where 3.2 f) also frames the tip.

The first observation in figure 3.2 is that the cytosol pulled back from the cell wall in all the samples, which is due to the osmotic shock. It is not clear if the medium enters the pollen from all sides or not, but in some samples (see Fig.3.2 b, c) it can be seen that the inner and the outer wall were physically separated, although KMCA did not separate them into different clusters (not shown). In one case (Fig.3.2 f) the wall did not get separated, but the cluster analysis revealed great spectral differences in those two parts, as can be seen in Figure 3.3 in the next section. Future investigations might focus on finding a way to stop the pollen tubes from growing without the osmotic shock, which might change the results. Stopping the growth is necessary here, because the growth rate is too fast for the imaging, most probably even with a faster CCD camera. Using shorter integration times would trade off too much signal-to-noise ratio, and reducing the spacial resolution would hinder the detection of the exact distribution of the integrative process.
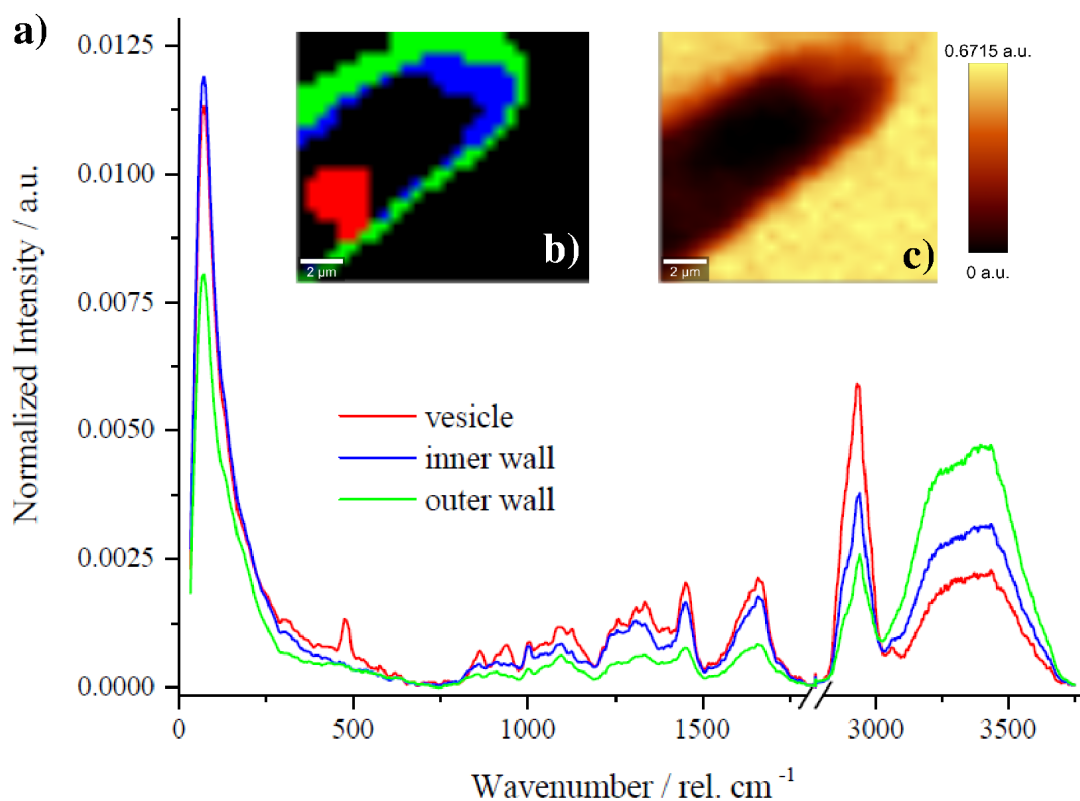
Figure 3.3: a) Full Raman spectra of the areas distinguished by KMCA and **b)** corresponding cluster image. The vesicle is represented in red, the inner wall in blue and the outer wall in green. The black area in the image corresponds to the medium and was not analyzed. **c)** Intensity image using the water peak (compare Fig.3.2 f).

3.2.1   Pollen Hydration

Figure 3.3 shows the average spectra resulting from the correspondingly colored clusters obtained by KMCA of 3.2 f). Shown in red is what is interpreted as a pectin vesicle. The inner side of the wall is shown in blue and the outer side of the wall in green. The O-H stretching modes appear as a very broad band from 3020 to 3700 cm^{-1} and are dominated by water [30], hence it can be named the water peak. Although the water peak was not included as argument in the KMCA, and therefor the different clusters were generated only by the spectral differences in the fingerprint and C-H regions, it can be seen that there is a great difference in the the size of the water peak. As a comparison the intensity image of the water signal is shown in the right image. Part of the cell wall can be seen, but the outer and inner parts cannot be differentiated as clearly as in the cluster image. Note also that the darkest area of the intensity image, containing least water, does not correspond to the area where the KMCA formed the vesicle cluster. For simplicity, this area is designated as the bulk here. The reason why the vesicle pixel were clustered separately from the bulk is probably that the vesicle spectrum contains more differences in the fingerprint region than the bulk area, while the latter (spectrum not shown) contains even lower amounts of water but in total less distinguishable variables (i.e. differences in the fingerprint region). As a consequence, it cannot be assumed that the clustered vesicle is in fact a vesicle - surrounded by a membrane, but it can be assumed that it shows unincorporated pectin, as

will be discussed below.

Because Raman spectroscopy allows the measurement of hydrated specimen, without interfering with the rest of the signals, the amount of water in the different compartments of the pollen tube can be used as an indicator for concentration or swelling (see section 3.4 for a discussion). It can be seen that most peaks become weaker with increasing water content. This could be related to the concentration difference of pectin in the different compartments of this small area of the cell. The vesicles most probably contain highly packed pectin, resulting in a very small water peak, even revealing an additional peak at 3070 cm^{-1}, while both wall spectra already contain much more water, and still the outer part is more hydrated than the inner one. This is an additional indication that the bulk and the putative vesicle clusters indeed constitute of unincorporated pectin.

The difference in water content could be explained as follows: While the pollen is still alive, the calcium gradient, together with PME, performs the cross-linking and thus hardening of the wall towards the shaft. The primary site of pectin delivery, and also contact point to enzymes and ions, is the inner surface of the wall. The amount of cross-linking sites is lower at the site of delivery, as the material is gradually de-methoxylated, but the calcium concentration is higher, so each carboxylate is immediately occupied by a calcium ion. Nevertheless, the amount of cross-links per unit area must be slightly higher on the inside of the pollen tube tip, because it is reduced by the radial expansion/deformation towards the outside of the wall. Since several samples were taken from the same batch, those imaged later the same day spent a longer time in the solution and thus some swelling may have occurred on the outer wall. Additionally, accumulation occurred in this sample, that is, the rate of delivery of pectin was higher than the rate of expansion of the tube, and thus the tip shows a very thick layer of pectin compared to the other samples. This fact also indicated that the bulk material can indeed be unincorporated pectin, but maybe already outside the vesicle membrane.
Although a difference in water content of different wall areas/compartments cannot be seen in all the samples, a big difference between wall and vesicle can be seen and will be discussed below.

3.2.2 Vesicles vs. Wall

Figure 3.4 shows the overall average spectra of the wall and the vesicle clusters calculated from six different pollen tube samples after PCA was performed. Most of the vibrations seen in the vesicle spectrum are about twice as intense as those of the wall spectrum. This could be due to the fact that the vesicles are very densely packed in comparison to the gel structure that pectin forms in the wall. In the C-H stretching region of the vesicle spectrum a peak at about 3012 cm^{-1} can be seen, which is neither present in the wall spectrum, nor mentioned in the literature listed in table 1.1 on page 34, nor mentioned elsewhere. The highest peak of the vesicle is at 2929 cm^{-1}, whereas the wall spectrum has its highest peak at 2939 cm^{-1} with a shoulder at 2929 cm^{-1}. There is no record of a peak at 2929 cm^{-1} in literature, but the wall-peak at 2939 cm^{-1} could be a C-H stretch of RGI or arabinan or a general pectin backbone peak[25]. The peak finding algorithm does not mark more peaks in this
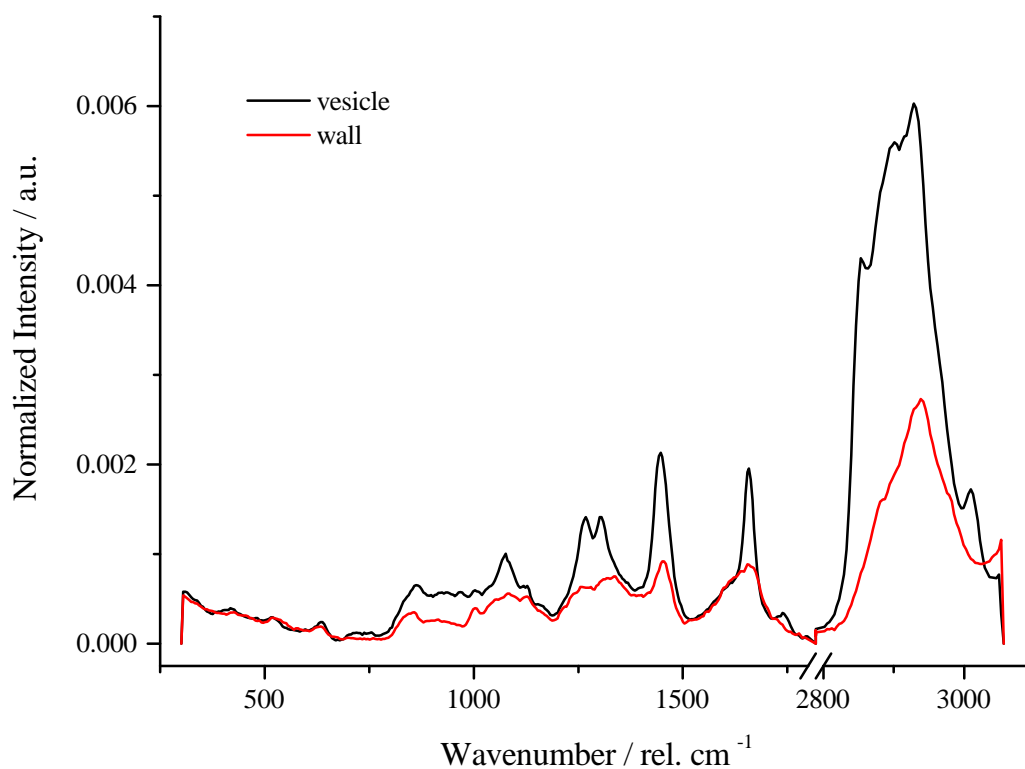
Figure 3.4: Average spectra of cell wall and vesicles of lily pollen tubes after cluster analysis (n=6). Only the regions analyzed by PCA are displayed.

region, although there is another important difference: When the C-H stretching region is scaled to the highest peak of both spectra, it can be seen that the vesicle spectrum shows a peak at about 2854 cm^{-1}, which is very close to the position of the methyl C-H stretch of the methylated form of pectin mentioned in literature at 2860 cm^{-1} [25]. This CH_3 stretching peak is present in both spectra, but has a much lower intensity in the wall spectrum.

The following peak is small but important and appears at 1740 cm^{-1} in the vesicle spectrum. According to literature, this peakrises from the C=O stretching of the carboxyl group on the galacturonic acid, and shifts from about 1740 to 1750 cm^{-1} upon methoxylation [25, Fig. 4]. The individual vesicle spectra reveal that this signal peaks between 1743 and 1747 cm^{-1}, which can indicate both the acid and the ester, although on average the acid seems to prevails. This peak is barely observed in the wall spectrum, which can be explained by the Ca-cross-linking in the wall according to Himmelsbach et al. [25]. They show that the disappearance of the C=O stretching signal is linked to an increase in two signals at 1605 and 1415 cm^{-1}, the asymmetric and symmetric stretching of the calcium carboxylate, respectively. The wall spectrum does show a little shoulder at 1415 cm^{-1}, and the signal is only slightly higher in the region of 1600-1620 cm^{-1}.

In the area of 1520-1700 cm^{-1} there is a big accumulation of bands peaking at 1657 cm^{-1} for the vesicles and at 1659 cm^{-1} for the wall. In the publications by Himmelsbach et al. [25] and Synytsya et al. [57] this spectral region hardly shows any peaks. But Larkin [30] mentions that carboxylic acid dimers show C=O stretches in that region, as well as the corresponding salts. The presence of water might be another fact that should be considered. Because the signal is much more intense in the

vesicle, it could also be assumed that it relates to the lipids forming the vesicles and the lipids in the cell membrane. The fact that several fatty acids show C=C stretches in this region [18] support that fact. Lignin has a peak at 1660 cm^{-1} [18], but it is unlikely that there is a high lignin content in the vesicles and not in the wall or that lignin is co-transported with pectin.

The spectral region from 1400 to 1500 cm^{-1} is known to show C-C stretching and twisting and bending of ethyl and methyl C-H groups, as well as C-O stretching [30]. This is reflected in the peak shape, because in both cases the peaks are very broad and thus a conjunction of many peaks. The wall spectrum has a strong peak at 1453 cm^{-1}, with almost identical height as the C=C stretch mentioned above, whereas the vesicle shows a very strong band at 1447 cm^{-1} that is about $1/5^{th}$ higher than the corresponding signal in the wall spectrum. The wall peak probably corresponds to the C-H scissoring of the methoxyl group δ(COO-C-H$_3$) [48, 57], and the lower shift of the vesicle band could again indicate fatty acids, like for example 13-Methylmyristic acid [18], but more likely there is another explanation. While the references do not mention any shift in this peak, it is questionable how to interpret it. In theory, the pectin in the vesicles should have a higher DM than in the wall, and thus, a higher intensity of this peak, which it does. A possibility is that the shift might arise from the presence of water or the configuration of the material. The dense packing of pectin in the vesicle might give a restriction on how much the bond can vibrate and thus cause a lower shift. In the wall the density is much lower, and more freedom of movement possible, leading to the shift also found in the dried material.

Furthermore, the wall average spectrum displays a peak at 1331 cm^{-1}, which should be a general pectin peak - δ(C-H), but is not present in the vesicle spectrum. At 1303 cm^{-1} the vesicle spectrum displays a band that is merely a shoulder in the wall spectrum. No reference to this peak was found in relation to pectin or cellulose. Both spectra exhibit a peak at 1268 cm^{-1}, the one in the vesicle spectrum being much more intense. According to Synytsya et al. [57] this peak corresponds to the C-O-C stretching (ν(COC)) of the methyl-ester of pectin, and thus it is in accordance with theory that this peak is more intense in the vesicle spectrum.

The wall and vesicle spectrum also show a general pectin peak at 1075 and 1084 cm^{-1}, respectively. They correspond to C-O stretching (ν(C-O)) and O-H deformation (δ(O-H)) vibrations, respectively. In the wall a weak band at 1003 cm^{-1}, is shifted to 1007 cm^{-1} in the vesicles. According to the reference database created by Gelder et al. [18], this peaks could correspond to fatty acids (i.e. Methylhexadecanoic acid - 1006 cm^{-1}) or to D-(+)-Glucose (1002 cm^{-1}). In the reference literature about pectin this band was not mentioned, although it can be recognized that this region bears some unassigned peaks in [25]. Generally the region from 950 - 1200 cm^{-1} is assigned to C-C and C-O stretches [18]. The skeletal vibration peak mentioned in the introduction is not obvious to interpret. Because there are several peaks in this region the band is very broad, and the localization by the WiTec algorithm is heavily influenced by that. Nevertheless there is a difference: it is located at 851 cm^{-1} in the wall spectrum, while it is shifted to 864 cm^{-1} in the vesicle spectrum. The two peaks cross each other around 858 cm^{-1} and the wall band has a higher signal at 850-858 cm^{-1}, while the vesicle peak is higher at 858-862 cm^{-1}. This could indicate that the pectin in the vesicles is acetylated, while it is not or less in the wall. It should be mentioned here that, according to Synytsya et al. [57], the acid or the

a) PC1   **b)** PC2   **c)** PC3
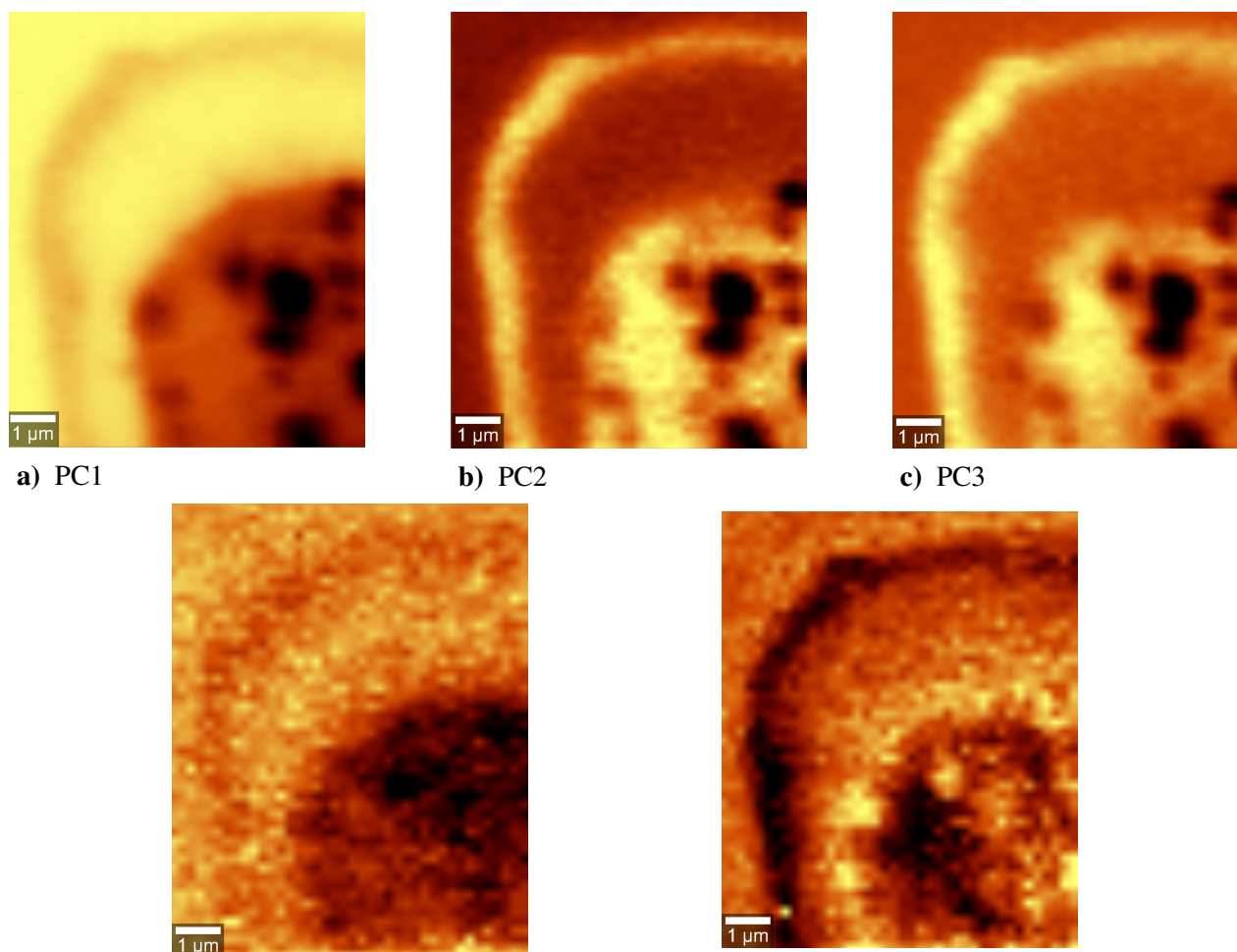
Figure 3.5: Local-eigenvalue images (transformed images) of the first five principal components of a pollen tube image, identified by the preliminary mixed PCA.

salt of PGalA have shifts that do not correspond to the DM/DA trends. The acid gives a signal at 853 cm^{-1} and the potassium salt at 857 cm^{-1} [57]. All lower bands are almost identical for both spectra.

The principal component analysis delivered many results on different levels. The first five eigenvalues resulting from the mixed PCA, performed as a pre-processing step, were plotted as an image in Fig.3.5. This transformed image now shows how much each data point scores in each principal component, expressed differently: how representative the loadings are for that point. This way, it can be seen which parts of the pollen image is described by which principal component. By observation of the loadings, compounds could be identified, but as mentioned in the introduction, the amount of data points showing i.e. the cytosol, the medium, the cell wall, the cell membrane and the vesicles differs, and hence care has to be taken upon interpretation. Nevertheless, it is interesting to look at the transformed images as a demonstration of the power of the PCA. Fig.3.5a) shows the local eigenvalues of the first axis. Since the loadings point in the negative direction (which is the case for all samples, data not shown), the image has to be perceived as the negative. Thus, the darker parts actually have the highest scores. It can be seen that the vesicles are darkest, then followed by the cytosol. This

only tells us that the cytosol must bear many organic molecules, and that its content is very different from the medium around the pollen, which has the lightest color of the image. The area between the cell wall and the cytosol appears as light as the one outside the pollen tube, which confirms that when the pollen tube growth is stopped by the osmotic shock, the medium enters the pollen through the cell wall. The wall area is clearly darker and must thus bare similar molecules or amounts of it as the vesicles. The variables scoring in the loadings must hence describe best the vesicles, but have common features with the wall, most probably pectin.

The second component, Fig.3.5b), prevalently describes mostly the cell wall and vibrations that are found in the cytosol. The vesicles are very dark, thus this component describes mostly common features of cytosol and cell wall. Note also that the very tip of the cell wall is a little weaker than the shank and shaft. Similar observations are made for the third axis, Fig.3.5c), which appears to describe the same thing as the second axis, but the medium scores higher, thus other materials must be important in this loadings. The fourth image,Fig.3.5d), mostly describes the measurement medium, as it appears lighter than the wall and the vesicles, as well as the cytosol. In Fig.3.5e) an interesting feature appears - the cell membrane and apparently areas around the vesicles. Clearly, the cell wall, appearing very dark, is not described by this combination of variables, instead they must mainly represent lipids, which is probably what is found upon inspection of the loadings. Again this confirms that indeed the cell membrane pulls back upon the osmotic shock. This short interpretation shows that a lot of information can be gained by looking at the transformed images of several axis, even without exact inspection of the loadings.

The second PCA that was computed, was done on each cluster (wall & vesicle) separately. The purpose was to clarify the assignment of ambiguous peaks found in the average spectra in terms of their belonging to pectic molecules or not and to which if possible. In the following the eigenvectors (= loadings) resulting from the second PCA will be analyzed. The main observation is that for the first component the eigenvectors all point into the same direction for vesicles and the wall and give mostly the same information. The second component is already very complex and only the C-H region will be discussed. The further axes will not be discussed here, as this would go beyond the scope of this work. For reasons of clarity Fig. 3.6a) and 3.6b) show the first eigenvectors of only one of the pollen tubes together with the corresponding average spectra (average of all samples). Because the first axes were originally pointing into the negative direction, they were multiplied by '-1' for the sake of comparison.

In the C-H stretching region of the vesicle PC1 (Fig. 3.6a)) the peak at 2929 cm^{-1} is visible as a shoulder, but two more peaks are emphasized as being of equal importance (height) than the 2929 cm^{-1} peak, that is at 2896 cm^{-1} and at 2855 cm^{-1}. The latter was already visible in the average spectrum and according to Himmelsbach et al. [25] indicates the methyl-ester C-H stretch of pectin. The band at 2896 cm^{-1} is similarly referred to as the symmetric stretching of the methyl-ester C-H of pectin by Synytsya et al. [57]. It is questionable why those two references did not detect both peaks, but both are visible in the spectra presented here. Also, a peak not mentioned in the references at 3013
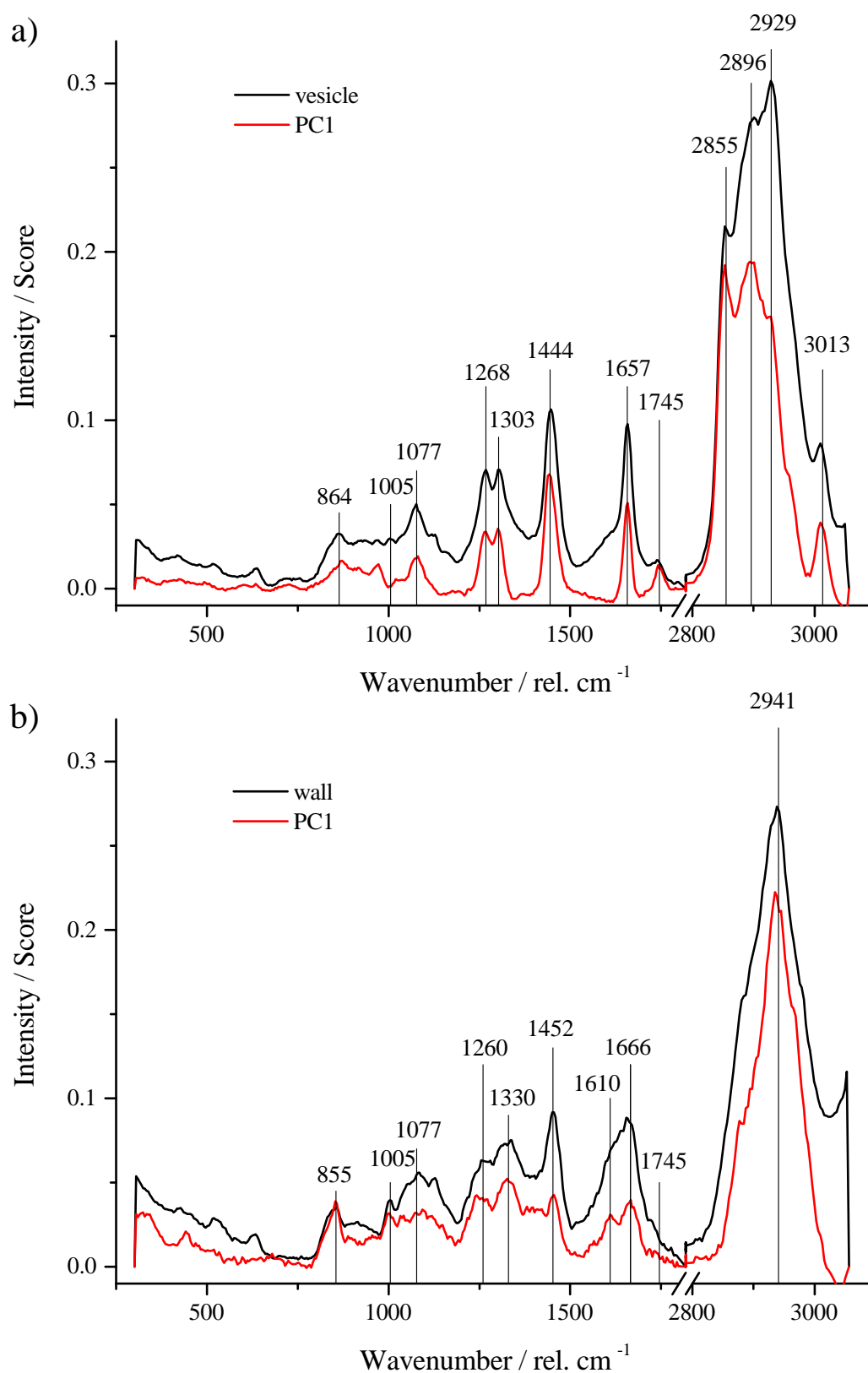
Figure 3.6: Eigenvectors of principal Component 1 resulting from the PCA of an exemplary wall and vesicle cluster, plotted together with the corresponding overall average spectra. **a)** Eigenvector and average spectrum of the vesicles. **b)** Eigenvector and average spectrum of the wall.

cm^{-1} is seen in the vesicle PC1 and is not present in the eigenvector of the wall. In the C-H stretching region of the wall an interesting trend is observable: the samples where the wall was separated (3.2 b,f) the shift of the general pectin C-H stretch is at about 2931 cm^{-1}, while it is at a higher position in the other samples (2936-2941 cm^{-1}). Himmelsbach et al. [25] show that pectic galactan has a lower position of this peak at about 2930 cm^{-1}, while the other investigated derivatives are at about 2941 cm^{-1}, which is a general pectin peak.

The first eigenvector of the vesicles also shows the carbonyl stretching of the methyl-ester of pectin as an isolated peak at 1745 cm^{-1}, while it is not present in the wall vector. The spectral region between 1520 and 1700 cm^{-1} does still show an accumulation of peaks, but the maximum that is already apparent in the average spectra of the wall (1659 cm^{-1}) is shifted to 1666 cm^{-1}. Also, a second peak becomes clear at 1610 cm^{-1}. The vesicle vector shows this peak in a much more narrow way with center at about 1655 cm^{-1} and the peak at 1610 cm^{-1} is not observable. The band at $\sim$ 1610 cm^{-1} could indicate the out-of-phase stretch of the carbonate of pectin (ν(C=O)), as mentioned in Séné et al. [48] and Himmelsbach et al. [25]. Even though there is no concrete assignment for the band at 1660 cm^{-1}, these last observations clearly indicate a de-methylated state of pectin in the cell wall, while pectin in the vesicles is methylated. Furthermore, it shows that PCA is capable of discriminating between different chemical states of the same substance, as long as the signals do not show a too strong co-localization.

As was seen in the average spectra, the eigenvector of the first axis reveals that the vesicles have a lower shift in the C-H bending/C-O stretching region (1444 cm^{-1}) and the wall a higher one (1452 cm^{-1}). Also, the general pectin peak at 1331 cm^{-1} is not present in the vesicle vector, instead the peak at about 1303 cm^{-1}, which is also partly visible in the wall vector. Another interesting difference of the PCs is the peak appearing at 1268 cm^{-1} in both average spectra. In the wall PC1 this peak appears at 1260 cm^{-1} on average, while it appears at 1268 cm^{-1} in the first principal component of the wall. Also, the samples where the cell wall was split, and a separate PCA performed for the inner and outer wall, show different shifts. The inner wall's peak is at about 1264 cm^{-1}, while the outer wall's is at about 1258 cm^{-1}. The spectra of arabinan and acetylated glucomannan show a peak at 1268 cm^{-1}, although there is no assignment [25]. Given the fact that the peak position of the inner wall is closer to the position of the vesicle, it could be argued that this peak is associated to lipids [18], since the inner part of the wall is also closer to the cell membrane. Otherwise, it could indicate a more methoxylated state, since the inner side of the wall is where the pectin is integrated into the wall.

The PC1 of the vesicles also shows that the peak at about 1077 cm^{-1} is important for the description of component, although already to a lesser degree than the previous peaks, due to its lower score. While not having an assignment, this band can be seen in several spectra of Himmelsbach et al. [25], always involving PGA - in its methoxylated or calcium cross-linked forms. Furthermore, the band at 1005 cm^{-1} is part of the description of the wall pectin, but not for the vesicles, although it can be seen in the average spectrum. As mentioned above, this peak could indicate to glucose or fatty acids, but is not mentioned in the literature as relating to pectin.

The rest of the eigenvector spectra are very similar to the respective average spectra. The skeletal vibration around 855 cm^{-1} is again shifted to lower wavenumbers in the wall (854-858 cm^{-1}) than

in the vesicle (858-864 cm^{-1}). This great variation does hence not allow any unambiguous statement about the degree of methoxylation or acetylation of pectin in the pollen tube. Nevertheless, Séné et al. [48] state that this peak becomes stronger in acidic pectins, which is the case here, since the score in the wall component is at about 0.4, while it is at 0.15 in the vesicle component.

As for the second component calculated by the PCA, all the lower wavenumbers show a very complex vector, that is not absolutely the same for all samples. The only information that is easily extractable from this component, is that the scores pass from positive to negative (or vice versa) between 2900 and 2920 cm^{-1} for both the vesicle and wall vectors. This indicates that there is a negative correlation between these peaks. Both peaks assigned to the C-H stretching of the methoxyl group thus are correlated, while the general pectin peak at 2940 cm^{-1} is not. This can be simply interpreted given the fact, that the eigenvectors are a mere representation of the direction of greatest variance. The general pectin peak is most probably more constant than the methoxyl-specific peak, because the methoxy groups are not present everywhere on the chain, that is, their distribution over the chain is not constant due to, for example, the degree of blockiness or the orientation of the chains themselves. This in turn causes this negative correlation.

3.2.3 Tip vs. Shaft

The cluster analysis of the different pollen tubes was not able to distinguish between the tip and the shaft spectra. For this reason, fig. 3.7 shows the average spectrum of the tip of one of the pollen tube (red) and the average spectrum of another pollen tube representing only the shaft (blue).

In the C-H stretching region the general pectin peak at 2041 cm^{-1} is identical for both spectra. The shoulder at about 2900 cm^{-1} has higher intensity in the shaft, but this band is not mentioned in literature. The band at 1653 cm^{-1} is more intense in the tip spectrum, but both have a slightly lower wavenumber than the average spectra of wall or vesicles. The assignment remains unsure, but could indicate lipids, as mentioned above. The methoxyl C-H bending is located at 1461 cm^{-1} in the shaft and is of higher intensity than the corresponding band in the tip spectrum, which is additionally shifted to 1453 cm^{-1}. The peak at 1270 cm^{-1} is more intense in the shaft spectrum, and should be indicative for the methyl-ester of pectin ($\nu(COC)$) [57], which does not support the theory, that de-methoxylation increases from the tip towards the shaft, and hence the signal should be equal or weaker than at the tip. The bands at 1125 and 1075 cm^{-1} have about double intensity than the corresponding tip peaks. The pair can be seen with similar shift and shape in the pectic galactan spectrum in [25]. The shape of the same region in the tip spectrum reminds more of the PGalA spectrum recorded by [25]. The skeletal vibration around 855 cm^{-1} is more isolated in the case of the tip spectrum, and locates to 853 cm^{-1}. The peak finding algorithm does not return any value in the case of the shaft. In the fingerprint region, the shaft spectrum has much higher intensity and isolated peaks. The principle components cannot be compared in this case, because PC1 of the shaft cluster is too noisy.
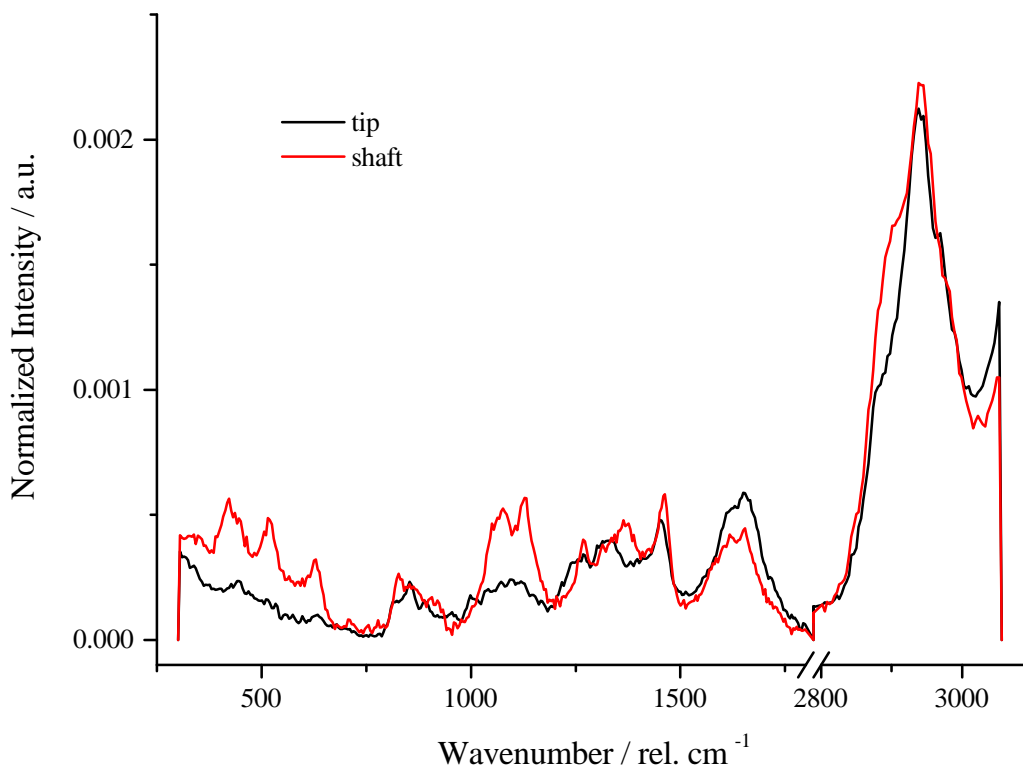
Figure 3.7: Average spectra a tip and a shaft cluster resulting from KMCA of two different pollen tubes.

3.3 Extracted Pectins

3.3.1 Pectin Solutions

As mentioned in chapters 2.3.2 and 2.4, the pectin samples were imaged in the x-z direction and then the spectra pre-selected via KMCA for further use. Figure 3.8 shows an example of the clusters resulting from the KMCA of a pectin solution image measured using a width of x= 20 µm and a depth of z = 80 µm. All the other images resulted in these four characteristic clusters as well. Figure 3.8 also shows the corresponding spectra, which are presented in the same colors as the clusters. In some of the samples up to 40 % of the total image spectra had to be excluded from the final average spectra, because of burning clumps (black curve, green area at the bottom), noisy parts near to clumps (blue), or because the cover glass was reached (green curve). For further analysis the red areas are used. Although it is not well visible in the glass spectrum of Fig. 3.8, the glass-cover has a characteristic spectrum with distinctive features when fully immersed in that sampling region. The glass region can be recognized by a very broad intensity increase in the region from 280 - 600 cm^{-1} and a broad peak at 925 cm^{-1}. In the interface region to the solution both, pectin and glass, are visible and these spectra must be sorted out, which was achieved by the KMCA (green area on the top of the image in figure 3.8).

Compared to the spectra found in the main references [25, 57], the intensity of the pectin spectra shown here is relatively low. The main reason is that they used an excitation laser wavelength of 1064
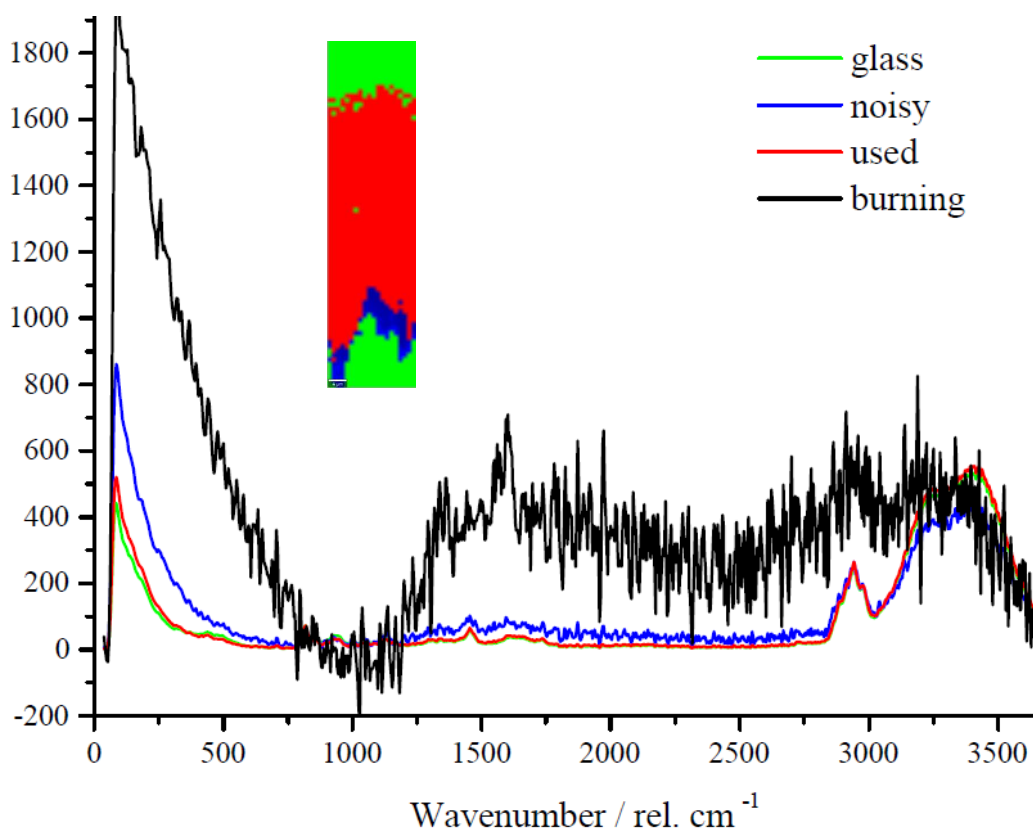
Figure 3.8: Clusters resulting from an exemplary LM pectin solution with the corresponding spectra; the lower green area is shown in black in the graph.

nm in both cases. The longer wavelength allows the use of much higher laser intensities (0.1 - 1 W), even though the samples were dried. Furthermore Himmelsbach et al. [25] pressed the dry samples into a gold die, thereby further amplifying the signal.

The high resolution used in this work proves to be inappropriate for pectin solutions prepared as described in section 2.2.2, because it reveals the microscopic inhomogeneity of the samples. For their reference samples Himmelsbach et al. [25] solved this issue by using a lens in order to de-focus the excitation laser beam. The inhomogeneities require additional data analysis tools (i.e. KMCA) in order to access the 'clean' part of the data. Effects such as sedimentation of (un)-hydrated clumps cause heavy changes in noise levels or even burning of the sample, as seen in Fig. 3.8. Possibly even orientation effects caused by aggregates of pectin might have an impact on the size (and position) of some peaks. All of these effects make it impossible to distinguish between different concentrations that are close together, such as 2 and 3 % solutions. Unfortunately higher concentration differences are hard to achieve with pectin, since the sample preparation becomes more and more difficult or even impossible with increasing concentration and the inhomogeneity most probably also increases. These are the reasons why only the spectra of the 3 % solutions were used for analysis.

The change in signal intensity that is observed though such a scan can be seen in the cross-section shown in Fig. 3.9 displayed as the sum of the whole C-H stretching region ($\sim$ 2830 - 3000 cm^{-1}).
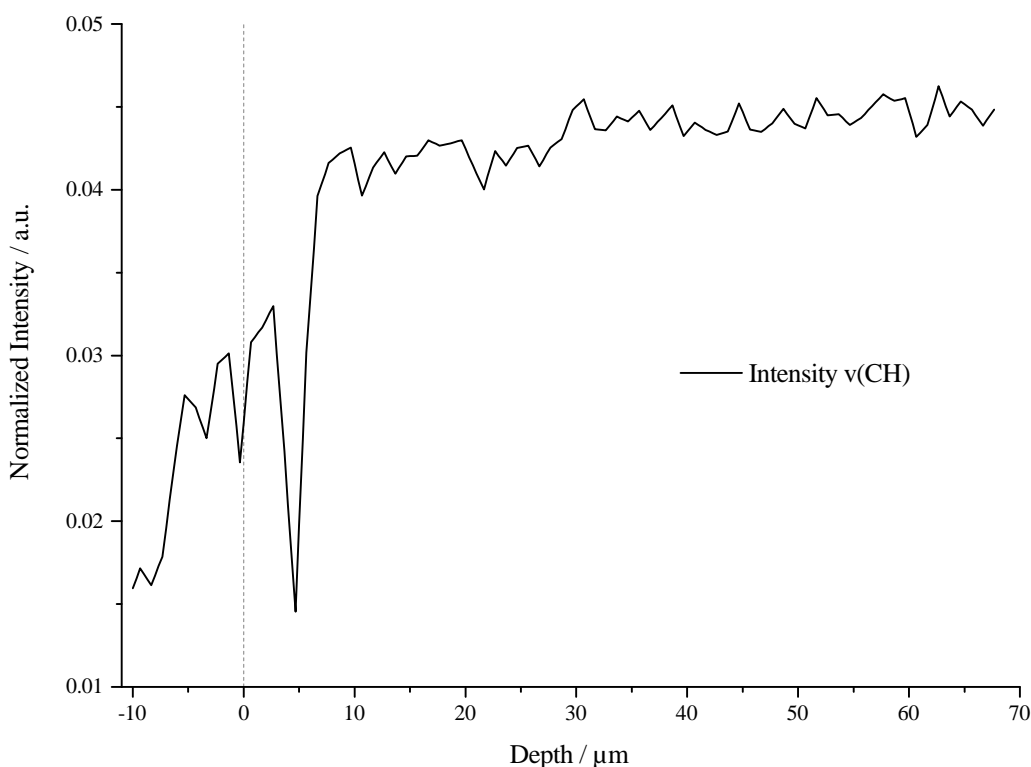
Figure 3.9: Vertical cross-section of an exemplary pectin solution image shown via the integrated intensity of the C-H vibration peaks; the dashed line represents the focus point.

The height where the laser was focused is shown by the dashed line and serves as zero reference point. At the top of the image (70 μm) the signal is slightly more intense, which is an inherent effect of confocal measurements and is an issue that can be overcome by normalization or by the use of a lens to disperse the lasers beam at the sample surface as was done by Himmelsbach et al. [25]. A linear regression of the interference-free part of the cross-section (10 - 70 μm) showed that the signal intensity decreases by about 10 % for this sample. This decrease is negligible for a peak of this size, but may have more influence on smaller peaks. In samples were spectra were taken deeper within the glass region (the upper edge of the image) the intensity difference is much higher, mainly because of the contribution of the glass bond vibrations. The sharp drop of intensity at 5 μm is caused by a clump at the bottom of the spectrum, resulting in burning of the sample and thus a drastic decrease of the C-H vibrational signal (see black curve in Fig. 3.8). The signal strength below the optical focus drops harshly due to the confocal setup.

Because of the above explained effects, the average spectra of all the pectin samples were calculated from the clusters resulting in comparatively less noisy average spectra. Depending on the sample, 800 to 1500 spectra were used for this purpose. Figure 3.10 shows the calculated average spectra in the range of 2800 - 3800 cm^{-1} (Fig.3.10A) and 800 - 1800 cm^{-1} (Fig.3.10B). The wavelengths shown are the average values of all the pectin solutions.

The water peak in Fig. 3.10A is of approximately same height in all the samples. It is followed by the C-H stretching peaks (ν(C-H)) at 2975 cm^{-1} and 2940 cm^{-1} and a shoulder and 2885 cm^{-1}. The
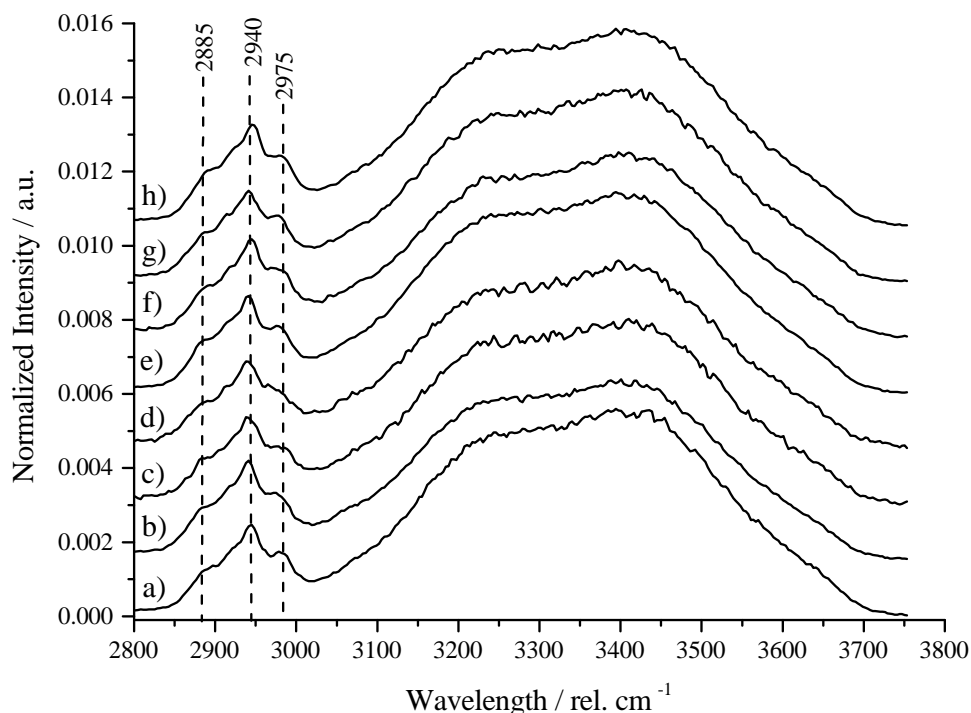
A) Spectral region from 2800-3800 cm−1. The O-H stretching region from 3050 to 3700 cm^{-1} is dominated by water. The dashed lines are located in the C-H stretching region and show the average peak values.
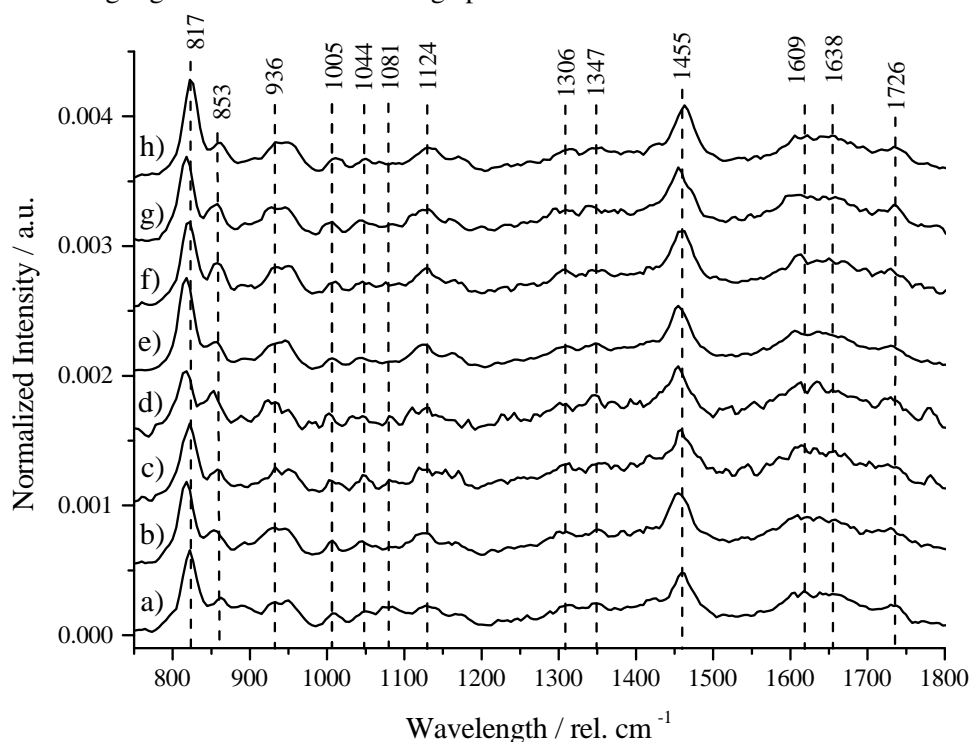
B) Spectral region from 800-1800 cm−1. The dashed lines show the average values of the peaks discussed in the text.

Figure 3.10: Average spectra of all pectin solutions. **a)** PGalA **b)** LMPC7, **c)** LMPC34K+, **d)** GenuLM12, **e)** HMPC70K+, **f)** GenuD, **g)** GenuB, **h)** HMPA75. See 2.1 (37) for details about the individual samples.

highest peak of the C-H vibrations is the general pectin peak at $\sim$ 2940 cm^{-1} (ν(CH)) [25, 57]. All the LMPs have a lower shift than the HMPs with PGA being exactly in the middle with 2940 cm^{-1}. For the LMPs this peak appears between 2037 and 2939 cm^{-1}, while for the HMPs it is shifted to 2941 cm^{-1}. The shoulder at 2885 cm^{-1} was specifically seen in the spectrum of methyl-α-PGA, but not assigned [25]. Note that this signal is also present in the spectrum of polygalacturonic acid (3.10Aa), although in theory it should not and it is hence questionable, if this signal really comes from the methyl-ester group. The peak at 2975 cm^{-1} is not seen in any of the reference spectra, which makes the C-H stretching region look different than seen in the spectra of the referenced papers. A possible reason could be the aggregate state, which is solid in the reference studies and liquid/suspension in the present one.

Fig. 3.10B shows the 'fingerprint' region of the spectrum. The carbonyl C=O stretching of the carboxylic acid or ester should be present at about 1745 cm^{-1}, the exact position being dependent on the substituent [25, 57]. This peak was not detected in any of the samples, instead an unknown peak between 1722-1730 cm^{-1} appears consistently, but is not mentioned in the literature nor seen in any of the reference spectra.

Contrary to the spectra in [25] and [57] there is an accumulation of many peaks in the spectral region from 1660 to 1700 cm^{-1}. The peak finding algorithm identified a peak at 1637 cm^{-1} on average. This peak is assigned to the C=C stretchings in [30] and might indicate some impurities in the extracted pectins as for example lignin, although no other lignin signals were detected Gierlinger2006. Lipids also show C=C bond vibrations in this spectral area, but it is not expected to find such molecules in these samples.

At 1609 cm^{-1} on average is a band that is assigned to the μ_{as}(COO$^-$) of the potassium salt of pectin in [57]. Not only is this peak present in all the spectra, but also does it not show an increased intensity in the potassium pectates investigated (Fig. 3.10B.c and e). Due to the liquid environment, the acid-base equilibrium explains the presence of carboxylate groups in the solution, and thus the appearance of this peak in the spectrum.

Although indicated as a marker for methoxylation [57, and others], the prominent peak at 1455 cm^{-1} is seen in all the spectra, including the one of PGA, where it should not appear if this assignment is correct. The only explanation would be that the signal is indeed a C-O stretching signal, as assigned in [59], but mixed with the C-H bending of the methoxy-group. This peak ranges from 1453 to 1457 cm^{-1} across the samples, but no trend regarding the DE can be observed.

In [25] a band at 1343 cm^{-1} was recorded for the methyl-polygalacturonate that is not seen in the other samples, nor was it assigned to a vibrational mode. Interestingly all of the spectra presented in Fig.3.10B show this peak, including PGA, and range from 1339 to 1349 cm^{-1}, but again no trend regarding the DE can be observed. A peak at 1306 cm^{-1} on average is consistently present in all the samples, but is not seen in any reference spectra, on the other hand the peak at 1270 cm^{-1} shown in [57], corresponding to v(COC)$_{Me-ester}$, is not seen in any of these spectra.

Around 1124 cm^{-1} a band can be seen that is also seen in the pectic galactan spectrum (β-(1-4)-galactose side-chain of pectin) presented in [25]. A band at about 1081 cm^{-1} is seen in the references that is higher than the one at 1124 cm^{-1}. In the presented pectin spectra, this peak is visible, but significantly smaller than the former. It can be found in the Ca-pectate and RGI spectrum at the same wavelength in [25]. At 1044 cm^{-1} the μ(CC)(CO) [57] peak is seen and is of similar height as the band appearing at 1005 cm^{-1}. The latter is not mentioned in the references, but is present in all samples presented here and can be seen in the some of the pectin and neutral polysaccharide spectra of Himmelsbach et al. [25]. Furthermore, a badly resolved multiplet with average center at 936 cm^{-1} can be seen. Even though the peak finding algorithm does not mark the individual bands, when measured by hand, they appear at approximately 930 and 950 cm^{-1}. The peak at 950 cm^{-1} is well visible in the arabinan spectrum shown in [25]and Synytsya et al. [57] designate the same peak as the CCH and COH scissoring of pectin. Also, they assigned a peak at 922 and 928 cm^{-1} to the C-H$_3$ bending of the methyl- and acetyl-ester, respectively [57]. Both peaks have approximately the same height relative to each other in all the samples, but are not seen this way in the references. Again it should be considered, that the hydrated state of pectin could be responsible for the different appearance of the spectra compared to those found in literature.

Finally, the skeletal vibration at $\sim$855 cm^{-1} did not prove to be useful for indicating the degree of esterification under the given measurement conditions. In their work Synytsya et al. [57] found that this vibration has a very low wavenumber of 853 cm^{-1} in polygalacturonic acid and the potassium salt 857 cm^{-1}. With increasing degree of methoxylation the peak shifts to smaller values from 856 to 850 cm^{-1}. In order to see if this behavior could be confirmed with the experiments presented here, the peak position of the skeletal vibration was plotted against the degree of esterification of the respective pectin sample in Fig. 3.11. PGA showed a shift of 856 cm^{-1} together with HPMA75. Interestingly GenuB, having basically the same DE of 70 % as HPMA75, shows its peak at 853 cm^{-1}. The only difference between them is the source (see table 2.1 on p. 37). The LMPs all have their skeletal vibration peak at 849 and 850 cm^{-1}. As opposed to the findings in [57], Fig.3.11 suggests that the LM pectins, with degree of methoxylation below 50 %, have a lower shift of the skeletal vibration. Also the other peaks mentioned above have been plotted in the same way against the DE, but no trend is recognizable for any of the peaks (plots not shown).

The last peak shown comes from iso-propanol, the internal standard, with mean position at 817 cm^{-1}. The way the data of this work were processed, the use of an internal standard was not helpful. Nevertheless, if the data should be used for other questions in the future, it can be useful to have it there.

Most peaks that have been identified in these spectra are known in the literature, but those claimed to be specific for the methoxy-groups also appear in the PGA spectrum, which should not be the case. Additionally, peaks have been found that are not mentioned in the literature at 2975, 1726, 1638, 1306 and 1005 cm^{-1}. The most probable cause, as already mentioned, is the solution state, which might change the behavior of the bond vibrations due to hydrogen bonding and hydrophobic interactions. Additionally, the peak shape/intensity can be altered by the molecular motion in the solution state,
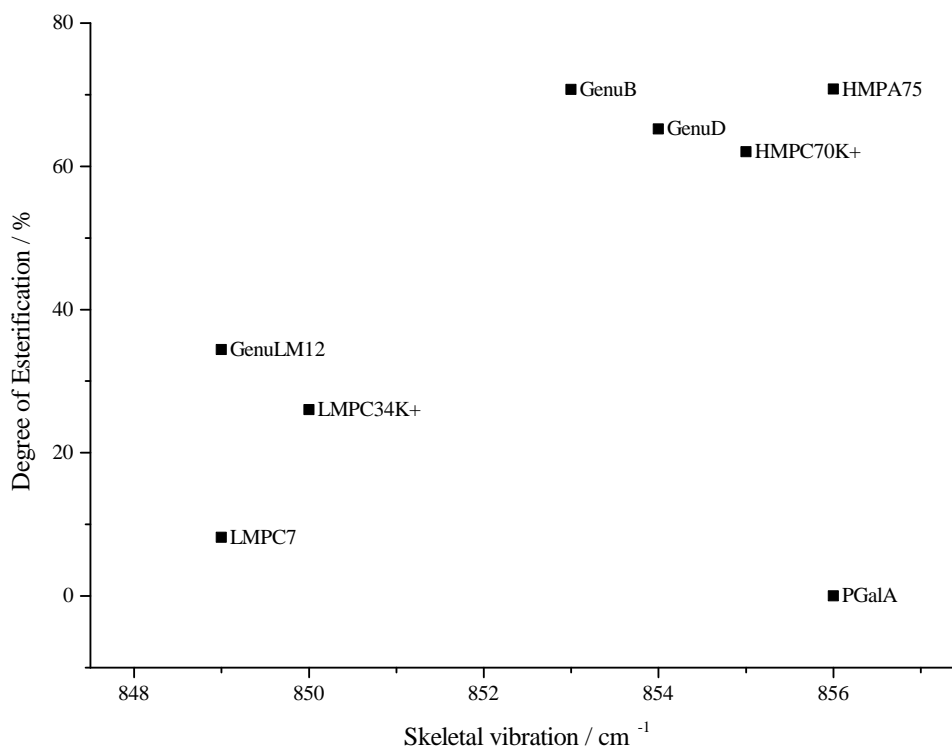
Figure 3.11: Spectral positions of the skeletal vibration of the different pectins relative to their degree of esterification. The LMPs tend to have a lower shift than the HMPs. Polygalacturonic acid (PGalA), together with HPMA75, has the highest shift of the series with 856 cm^{-1}.

since Raman spectroscopy is sensitive to the orientation of a molecule, as is the case in solution state NMR.

The spectra of the extracted pectin samples did not give a hint on their degree of methoxylation, since none of the signals did show any obvious dependence on the latter. Also, as opposed to what was expected, PGA did not show any significant differences to the other samples. Since no PCA could be performed on these samples, because the spectra were too noisy, the information extracted by the eigenvectors could not be accessed, which might have given a mean for differentiation. Perhaps the subtraction of the polygalacturonic acid spectrum from the other spectra could hint on peaks indicative for the DE. Furthermore, the recording of spectra with different concentrations would be useful in order to assert spectral differences in this regard and eventually lead to the construction of a model for the pectin in the pollen tubes. This in turn requires the realization of a homogeneous pectin solution, definitely including the adjustment of the pH value with an appropriate agent, which was not attempted here. Due to the polyprotic nature of pectin and the high viscosity, adjusting the pH might not be an easy task. Perhaps the easiest way would be the preparation of a bigger amount of a very low percent solution for the adjustment of the pH and then evaporation of water to achieve the right concentration. As such, this experimental series may serve as a basis for further experiments.

3.3.2 Ca^{2+}-cross-linking of extracted pectins

In the following section the spectra and images of the calcium cross-linking trials will be analyzed. The procedures elucidated in section 2.2.2 (p. 2.2.2) for the production of a pectin gel were considered as satisfactory when the spectra resulting from these experiments did not show too strong fluorescence, too much noise or burning. Again, the images were clustered using KMCA and the average spectra resulting from the clusters compared. The experiments were labeled T1 (mix powders), T2 (dilute to half) and T3 (dilute to half and stir). Apart from the mixing times, the main difference between the experiments was the concentration of the calcium added. T1 was prepared by mixing the powders and had the highest concentration of calcium, with the binding sites over-saturated (R = 1.3). T2 was attempted with half of that concentration, that is, about half of binding sites were occupied (R = 0.6). T3 had a CaCl$_2$ concentration 20 times lower than T2, with R = 0.03 corresponding to 3 % of binding sites occupied. Figure 3.12 shows the clusters resulting from the KMCA. The black areas are those that showed burning of the samples or fluorescence and were excluded from further analysis. T1 (Fig. 3.12a)) resulted in two main clusters, while T2 (Fig. 3.12b)) and T3 (Fig. 3.12c)) showed three distinct clusters. Also, it can be seen that the distribution of the individual clusters in the particular frames becomes more homogeneous with decreasing R-value and increasing mixing time.

a) T1 - Mixed Powders (R = 1.3)

b) T2 - Dilute to Half (R = 0.6)

c) T3 - Dilute to Half and Stir (R = 0.03)
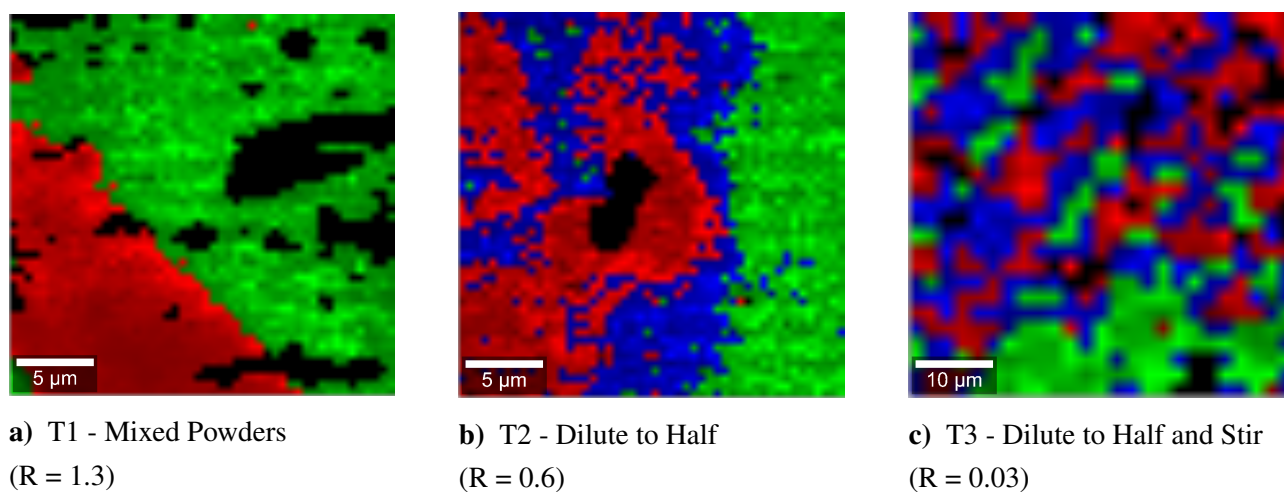
Figure 3.12: Cluster images resulting from the cluster analysis made on the Ca-cross-linked GenuLM12 samples T1, T2 and T3. **a)** T1 - Mixed Powders (R = 1.3), scale = 5 μm; **b)** T2 - dilute to half (R = 0.6), scale = 5 μm; **c)** T3 - dilute to half and stir (R = 0.03), scale = 10 μm. The individual colors reflect the similarity of the spectra across the experiments - the average spectra of the red, blue and green areas, respectively, are the most similar as will be detailed below. Black areas are clumps that burned or were very noisy.

The first step was to find out if the individual clusters of the different experiments had something in common. All the average spectra of the clusters were overlaid and the most striking differences between the clusters - and similarity between the experiments - were asserted. In Figure 3.13b) the

most obvious change was found in the normalized size of the water peak (3020 - 3720 cm^{-1}). The spectra were colored by experiment and three different intensity levels were found for each of the experiments. Although the calcium concentrations used for each experiment were very different, the intensity levels of the water peak were found to be similar between the experiments, as can be seen in the representation of Fig. 3.13a) . This similarity was employed for the coloring of the clusters of Fig. 3.12. The red areas in Fig. 3.12, showed the lowest intensity of the water peak, while the blue and the green spectra showed a gradual increase of that signal, the coloring being analogous in 3.13a) .

The spectrum of one cluster of each experiment thus showed a similar intensity to one cluster of the other experiments, independent of the concentration of the calcium solutions. Upon cross-linking, water is gradually pushed out of the forming gel, because part of the hydration shell of the individual chains is replaced by ionic interactions with calcium ions and neighboring chains [49]. Therefore, the clusters with least water intensity probably reflect a more densely cross-linked area, the middle range a less linked area and the clusters where the water peak has highest intensity may be in a state closer to a solution. This was verified by additionally overlaying the GenuLM12 spectrum from the solution experiments, where it was found that, indeed, the amount of water in the solution spectrum was in the range of the green spectra of Fig. 3.13a) (not shown). Therefore, from here on the red clusters and spectra will be called 'cross-linked', the blue ones 'less linked' and the green ones 'solution'. Note that the green T1 curve (Fig. 3.13b)) is located between the blue and the other green curves, indicating that this area could be divided into more sub-clusters (i.e. analogous to the other samples).

The C-H stretching modes are also seen in Figure 3.13. The peak and shoulder positions are the same as for the pectin solution spectra in the previous section. The highest peak is again the general pectin C-H stretch at 2941 cm^{-1}. Interestingly, the peak finding algorithm showed that for the T3 experiment this peak is centered at 2946 cm^{-1}, while most other peaks in this spectrum are at the same position as in the other samples. The other peaks that can be discerned are shoulders which are not recognized by the algorithm, that is at 2975, 2915 and 2891 cm^{-1} as in the pectin solutions.

The intensity and also the behavior of the CH peak varies in the different experiments, as can be seen in Figure 3.13a) . The different clusters of experiments T1 (red) and T2 (blue) have different CH intensities, while interestingly the ones of T3 (black) are of exactly the same height. Also, T1 shows the highest intensity of all the cross-linked spectra, while the solution spectrum CH peak is of the same height as the cross-linked spectrum of T2. Each cluster of experiment T2 also shows different CH intensities, and it can be seen that the solution spectrum's peak is lower than the T3 intensities, which are the same for all three clusters. So although the cluster's water peak intensities are very similar for each of the experiments, the CH peaks do not behave in the same way for all of them. There is no obvious correlation between the size of the OH and CH peaks, but possible reasons will be discussed below.

Three only partially dependent phenomena can be observed at this point: First of all, the homogeneity of the sample is altered by the $Ca^{2}+$ concentration. Secondly, the OH peak shows approx. three
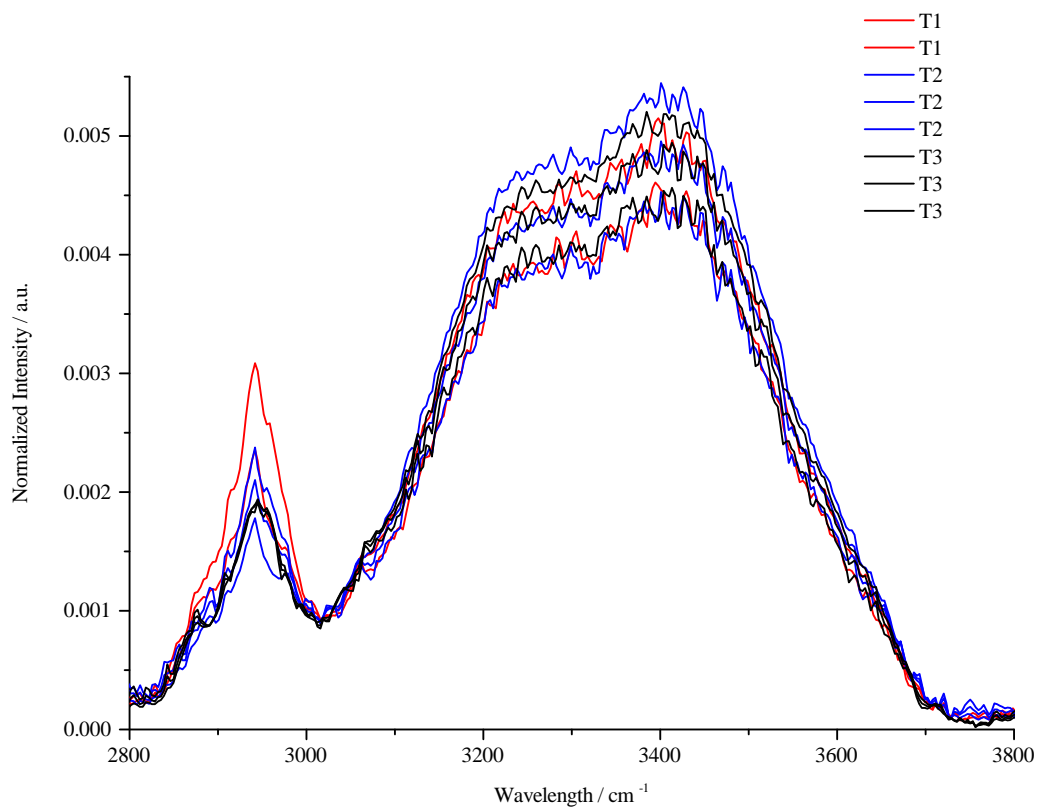
a) The curves are colored by assay.
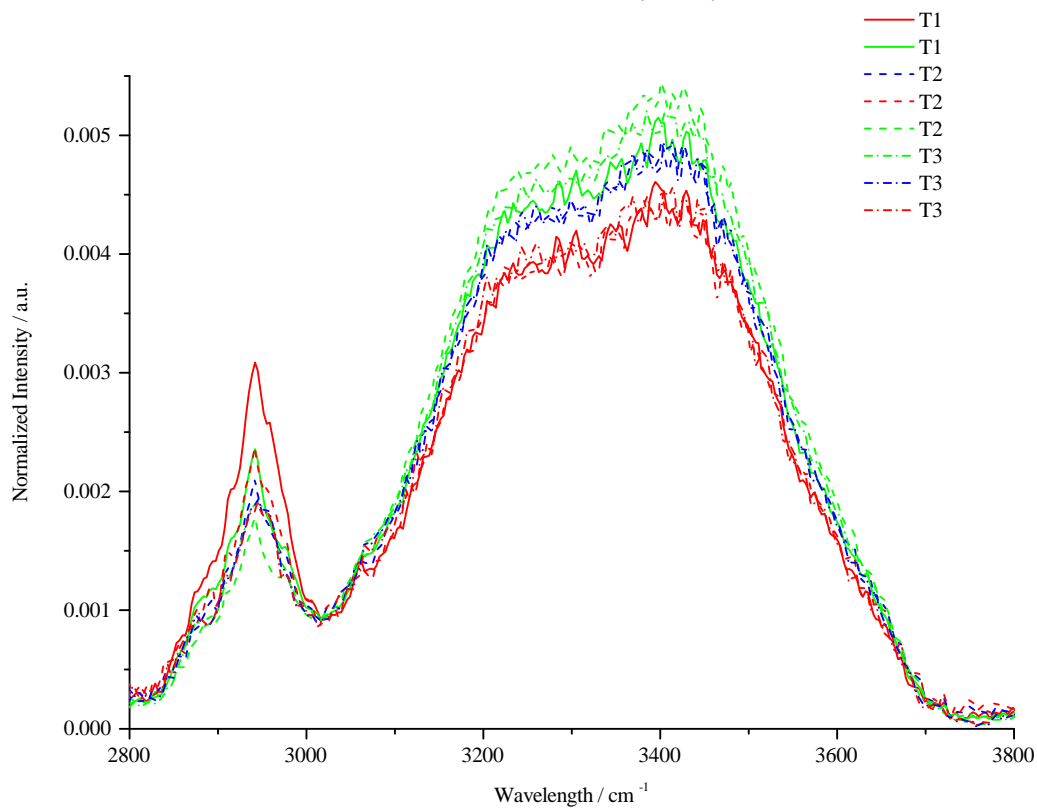
b) The curves are colored by cluster-type.

Figure 3.13: Calcium-cross-linked GenuLM12 average spectra in the region of 2800 - 3800 cm^{-1} showing the C-H and O-H stretching vibrations.

different intensity levels, which are the same for all cross-linking experiments. Therefore, in each of the experiments three areas of different water content were formed, independent of the Ca^{2+} concentration. And thirdly, the CH peak's intensity seems to be depend on the calcium concentration. Conversely, experiment T3 behaves totally different by showing the same CH level for each cluster, while the OH peak displays the same intensities as the other experiments. The changes in homogeneity can be explained by the kinetics of the cross-linking reaction. Pectin binds calcium via positive cooperative binding [49], that is, pectin's affinity for calcium increases with increasing amounts of occupied carbonyl residues. Therefore, the binding rate increases.

In experiment T1 - the least homogeneous sample - a calcium concentration above the saturation level of the binding sites (R > 1) was used. The pectin and $CaCl_2$ powders were mixed in the dried state and then water added after moistening. The inhomogeneity of the mixed powders, due to the presence of small $CaCl_2$ crystals and pectin clumps, results in very high local calcium concentrations in the moment that the added water dissolves the $CaCl_2$. For this reason, pectin can bind many ions at the same time, leading to a much steeper increase of its affinity for further calcium and to the formation of relatively big areas with all occupied binding sites. The excess calcium must diffuse through the cross-linked areas, which are barely agitated by the mixing process. The fact that the amount of water in this area is still the same as for the other samples, might be due to the saturated state of the binding sites, which determines the maximal amount of water that can be present. The cross-linking increases the density of the network, and therefore the intensitiy of CH peak. The excess calcium present in the cross-linked parts of this sample could explain the very high intensity of the CH peak, because it could be that the ion enhances the Raman activity of many vibrational modes of pectin. If this is the case, then this peak cannot be used as an indication for concentration of pectin in the presence of calcium.

In experiments T2 and T3 the situation is different, because the pectin solutions were diluted to half using the calcium solutions. At the interface where the two liquids meet, pectin also forms cross-linked areas, which should be understood as boundaries through which unbound calcium must pass through. The process of chelation is probably slower in experiments T2 and T3, because the lower calcium concentration affects the binding rate. As a consequence, the stirring process has a bigger influence on the distribution of calcium, resulting in a more even clustering. The middle and lower water content can be explained, if the gel formation is regarded as the formation of a new phase, leading to phase separation of water and pectin. This separation is far from complete, which is why pectin is detected also in these spectra. Unfortunately this does not explain why the CH peak intensities in experiment T3, with a theoretical occupation of the binding sites of 3 %, are the same for all the clusters. Especially given the fact that the CH intensity is higher than the lowest of the T2 experiment, which contains 20x more calcium. Swelling of the gel could be a reason, where the stretching of the pectin chains causes the network to loosen up, reducing the density and, thus, the CH signal. Theoretically, this would imply increased amounts of water relative to the other samples, which is not the case. Furthermore, since the binding and unbinding of calcium is an equilibrium state, a redistribution of the cross-links is possible, from the more cross-linked to less linked areas. This would also explain the more homogeneous state of T3, which, in addition to a very low calcium concentration, had a very

long mixing time compared to the other samples.

A lot of indications could already be gained from just the high frequency part of the spectrum, but the fingerprint region also shows interesting features, as can be seen in Figure 3.14. First of all, the spectral changes, asserted by Himmelsbach et al. [25] for the dried calcium-pectin-film, were the disappearance of the C=O stretch at 1743 cm^{-1} and the appearance of the asymmetric and symmetric OCO stretches at 1605 cm^{-1} and 1415 cm^{-1}, respectively. Furthermore, they observed a decrease in intensity of the skeletal vibration at 856 cm^{-1} and the appearance of a new peak at 814 cm^{-1} upon cross-linking. The above mentioned peaks are shown with dashed lines in Fig. 3.14.
The observations made by Himmelsbach et al. [25] could not be totally confirmed in the liquid environment. In the cross-linked spectrum T1 (Fig. 3.14a)) the C=O stretch is seen most clearly, but it is also visible in the T1 solution spectrum, while it is not in the other trials, nor in GenuLM12 without the addition of CaCl$_2$ (see 3.10, p. 64. All the spectra show the peak at 1605 cm^{-1}, although it is less intense than the peak at 1645 cm^{-1} in T3 (Fig. 3.14c)), while it is not in T1 and T2 (Fig. 3.14b)). The band at 1415 cm^{-1} cannot be observed as isolated peak in any of the spectra. As opposed to the indications made in the literature, the intensity of the skeletal vibration at ~ 855 cm^{-1} increases from cluster to cluster, notably showing the most striking increase. This is especially well seen in the spectrum of T2 (Fig. 3.14b)). In the solution spectrum of experiment T2 the band at 855 cm^{-1} is smaller than the internal standard peak at ~ 817 cm^{-1}. In the less cross-linked spectrum there is an increase in intensity of the 817 cm^{-1} peak, which could be related to the appearance of the peak at 814 cm^{-1} and therefore matching the indications by Himmelsbach et al. [25]. However, the skeletal vibration peak in this spectrum also increases and is higher than the ISTD peak. The cross-linked T2 spectrum shows only a minimal increase of the ISTD peak (relative to T2), but shows another substantial increase of the band at 855 cm^{-1}. The same was observed for T1 from the solution to the cross-linked spectrum, but not for sample T3, where the iso-propanol peak is very weak and barely visible in all of the clusters. An explanation for this could be that the iso-propanol partly evaporated during the long stirring period, even though the beakers were sealed.

In addition to the peaks indicated by Himmelsbach et al. [25] as responding to the calcium cross-linking of pectin, more changes can be observed in the spectra of Fig.3.14. An observation that is independent of the way the cross-linking was attempted is the general intensity increase of the spectral regions from approx. 1600-1750 cm^{-1}, 1300-1450 cm^{-1} and 800-1150 cm^{-1} from the solution to the cross-linked spectra. This is not completely true for experiment T3, which shows increases only in the regions of 1600-1750 cm^{-1} and ca. 800 - 950 cm^{-1}, and additionally at the C-H bending of the methyl ester at 1455 cm^{-1}. As in the pectin solution spectra, all the samples show a consistent peak at about 1730 cm^{-1} that is not mentioned in any of the references and which shows a distinct increase. Also increasing is the peak at ~ 1645 cm^{-1}, which was additionally located at 1638 cm^{-1} on average in the pectin solution samples. This peak is not mentioned in the literature and this spectral region indicates C=C or C=O double bonds [18, 30]. As in T3, the methyl ester C-H bending at 1455 cm^{-1} also shows an increase in the other samples. A strong increase is also seen in the peaks at 1334 cm^{-1} and 1302 cm^{-1}, which is especially well seen in sample T2 (Fig. 3.14b)). The band at 1334
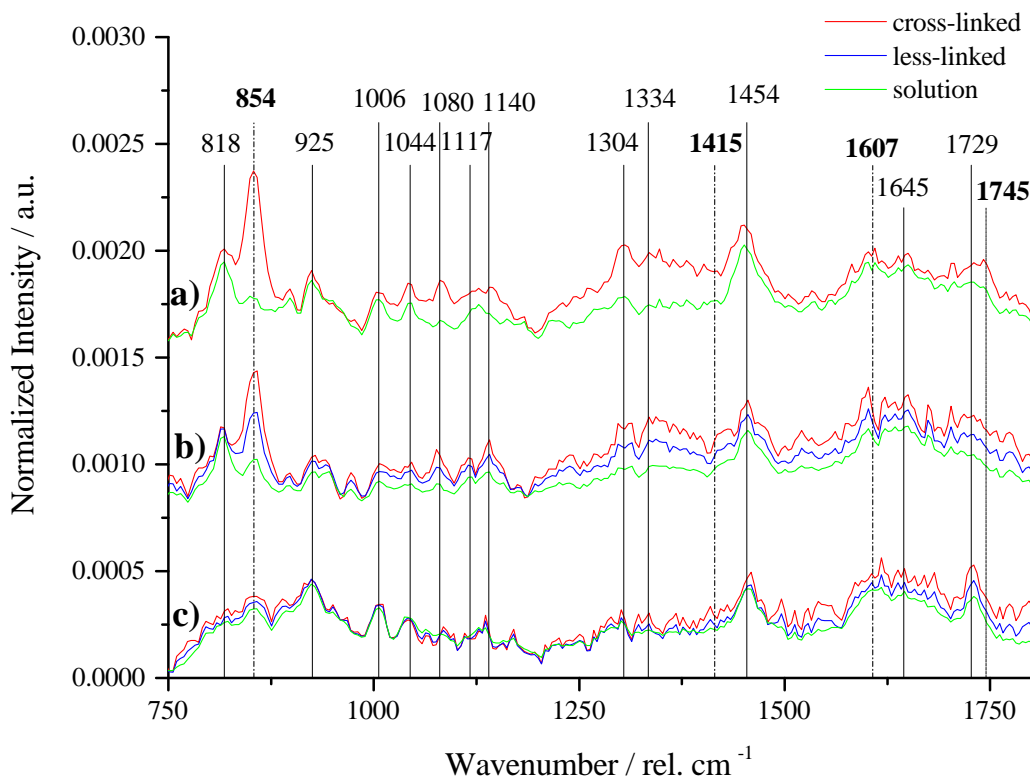
Figure 3.14: Grouped average spectra (750 - 1800 cm^{-1}) resulting from the cluster analysis performed on the images of the cross-linking experiments. The solution spectra are shown in green, the less cross-linked spectra in blue and the cross-linked spectra in red. **a)** 'Mixed Powders', alias T1. Note that only two clusters were formed and thus only two spectra are shown. **b)** 'Dilute to half', alias T2. **c)** 'Dilute to half and stirr', alias T3.

cm^{-1} is mentioned in both Himmelsbach et al. [25] and Synytsya et al. [57], which refer to it as a general CH deformation. The peak at ca. 1304 cm^{-1} is not present in any of the references, but again consistently in all the spectra recorded in the present work. Generally, vibrations from C-H bendings and carboxylates' C=O stretchings are seen in this spectral region [30]. In the region between 1000 - 1150 cm^{-1} mostly C-O stretches and in phase C-O-C stretches should be observable [30] in pectin. At 1140 cm^{-1} a peak is seen that is found at 1140 cm^{-1} and 1137 cm^{-1} in the calcium-cross-linked pectin and in the RG I spectrum of Himmelsbach et al. [25], respectively. It was associated to glycosidic C-O-C stretching [25, 57]. Also the bands at about 1082, 1045 and 1009 cm^{-1} show an increase in intensity, where the one at 1082 cm^{-1} shows the biggest increase and is apparent in the calcium-cross-linked spectrum of [25].

The increase in peak intensities described above was not observed in the solid state spectra of the references [25, 57]. Different phenomena could be the reason: The calcium ions in solution probably enhance the Raman activity of certain vibrational modes. Additionally, one reason could be that, upon cross-linking, the pectin chains become less motile and hence they have a more stable and uniform orientation (although not as immobile as a solid). This explanation is supported by the fact that many of the increasing peaks are the same for all the samples, even so some features differ. This could be caused by the remaining motion of the pectic chains. Further experiments, involving the fixing of the

sample axes, will be necessary to test this hypothesis. Additionally it can be said that the algorithm of the WiTec software found roughly the same peaks for the cross-linked samples as for the non-cross-linked ones, although some shifts are different do to the width and/or appearance/increase of some peaks.

A direct comparison of the cross-linked spectra of all the three procedures is shown in Fig. 3.15. The pectin concentration of all the samples is the same; just the amount of calcium is different, which is reflected most directly by the intensity of the skeletal vibration at ~ 855 cm^{-1} and the intensity of the C-H stretching peak from approx. 2800 - 3050 cm^{-1}. Even though the R values are no true values, they still can be correlated to the intensity of the spectra, and thus to the relative amount of cross-linking.
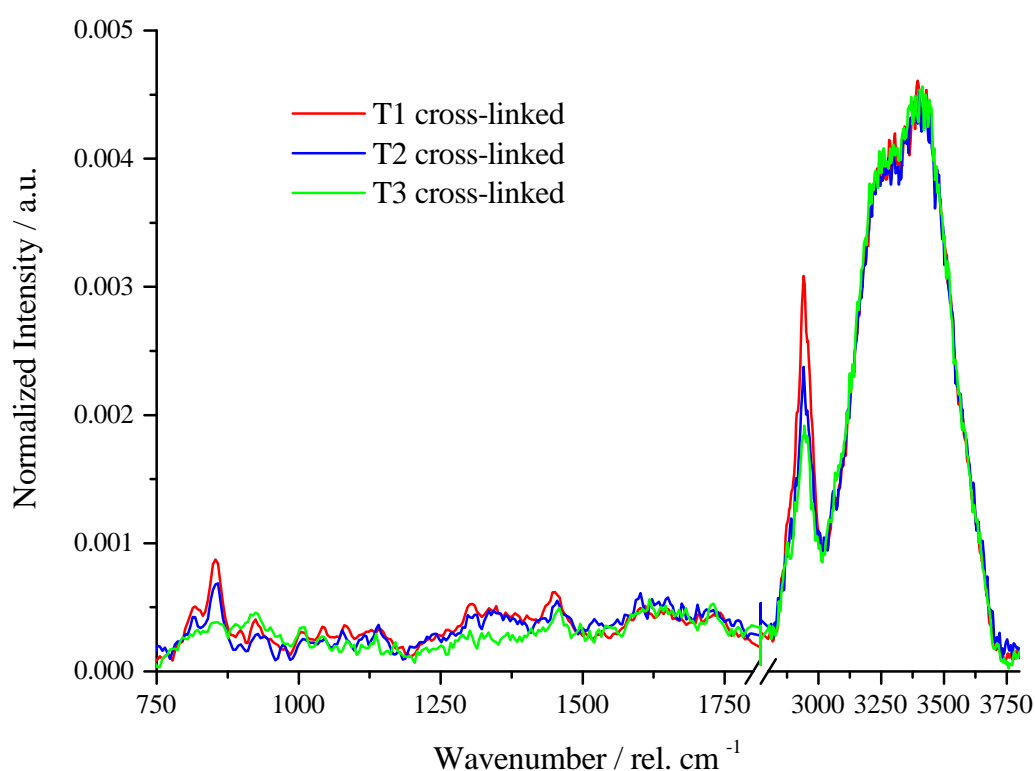
Figure 3.15: Comparison of the average spectra of the three cross-linking assays for GenuLM12. The average spectra result from the cross-linked areas clustered by KMCA.

The T1 spectrum, with a ratio of calcium ions to binding sites of 1.3, has the most intense C-H stretching vibration and also the skeletal vibration peak is the most intense of all the cross-linked spectra. This is followed by T2 with R = 0.6, showing the second highest ν (C-H) and skeletal vibration bands. Finally T3, with R = 0.03, has the lowest intensity in the above mentioned peaks and also in the spectral region between 1400 cm^{-1} and 1250 cm^{-1}. Note that the O-H stretching region has approximately the same intensity for all the samples.

An experimental series, involving the systematic increase of the R-value and using always the same procedure (i.e. T3), should give a better picture about the impact of calcium on the spectra of low methoxyl pectins. The peaks could be investigated in terms of their shifts and intensity increases, as

well as the behavior of the O-H stretching vibration.

3.4   Pollen vs. extracted Pectins

The purpose of this chapter is to compare the results from the two previous chapters. First the intensity and shape of the CH and OH vibrations in the high spectral regions will be discussed, as these signals seem to indicate correlation with density, swelling and/or cross-linking of pectin. Then the major differences in the spectral region from 800 - 1800 cm^{-1} will be asserted.

The integrated intensities of the whole CH and OH stretching regions (I_{CH} and I_{OH}) of the average spectra of all used samples were plotted in Fig. 3.16a) and b), respectively. Additionally, Fig. 3.16c) shows the ratio of CH to OH intensities in order to assess if this value is informative at all. The data were sorted in increasing (I_{CH} and $I_{CH/OH}$) or decreasing order (I_{OH}) to help understand the behavior of those two peaks over all samples, as it became clear in the last section that there is no obvious relation between their intensities.

In Figure 3.16a) the increase of the CH intensity coincides with the concentration of the pectin solutions and the pollen samples. The calcium assays were made with 2 % GenuLM12 solutions and the T2 solution cluster, as well as all the T3 clusters, is located at the lower end of the scale. This is followed by two wall clusters originating from image 3.2e) (p. 51), which show especially low CH intensities. The T2 less linked cluster forms a small boundary, its CH intensity being 0.062. The intensity values of the previous samples are located between 0.05 and 0.06. Calcium experiments T1 solution and T2 cross-linked appear towards 0.07 intensity values, followed by the 3 % pectin solutions (I_{CH} = 0.07 - 0.082). The pectin series is interrupted by some of the pollen wall clusters and the calcium cross-linked T1 cluster has a CH intensity almost identical to the one of the wall average (0.086). The samples with the highest CH intensity are all vesicle clusters (average I_{CH} = 0.2) and the remaining wall clusters (average I_{CH} = 0.09). This suggests that the CH peaks are sensitive to concentration, but to some extent also to the degree of cross-linking.

In the case of the OH peaks (Fig. 3.16b) the situation is different. An interesting observation is that all the different wall clusters are spread over almost the whole range of OH intensity values (I_{OH} = 0.74 - 0.55), one sample (Fig. 3.2f, 51) even lying at the level of the average vesicle (I_{OH} = 0.39). The pollen vesicles clearly gather at the lower end of the scale, containing only little water. All the pectin solutions, including the ones from the calcium experiments also have quite spread values (I_{OH} = 0.73 - 0.65). The less linked calcium clusters are grouped at 0.65 and the cross-linked calcium samples are grouped around I_{OH} = 0.59, right after the average wall spectrum with I_{OH} = 0.61. This ranking suggests that the water content alone does not correlate with concentration, but somehow is linked to the density of pectin. That is, if the material is in solution or a in a calcium cross-linked state that has swollen, the water peak is big. If on the other hand, the cross-linking is very dense, or pectin is packed into the vesicle, then the water peak is smaller.

Fig. 3.16c shows the percentile ratio of the CH and OH intensities. At a first glance the sorting of

Figure 3.16: Comparison of the integrated CH and OH intensities (**a** and **b**, resp.) and the percent ratio of CH/OH (**c**) of all sample average spectra. In each graph the samples were sorted in ascending or descending order. The clusters of calcium pectin samples were additionally labeled, as well as the pollen wall and vesicle averages. Note that the highest bar in graph **c** does show 220 %.

the percentage values of the CH/OH ratio seems to be dominated by the CH intensities: The calcium solution and less linked samples again have the lowest values ($I_{CH/OH}$ = 7 - 8 %), the cross-linked clusters thereof being placed in the middle and higher ends of the scale with 10, 12 and 15 % , respectively. The pectin solutions are located in the middle of the scale and have a CH/OH percentage of 10.5 - 13.5 %. The pollen wall clusters are spread similarly to the CH sorted data, and the vesicles again group at the highest percentages. One sample (Fig. 3.2e even shows a percentage of over 200 % for the calculated ratio. When looking at the ranking of the individual samples, some switches and shifts are observable, but do not change the overall trends described above. While forming the CH to OH ratio shows grouping of the sample groups, it should be concluded that forming the ratio of these two peaks gives a wrong picture, because the behavior of the OH peak is not well reflected and hence some information is lost.

The question remains as how or if these two effects, that is the concentration/cross-linking dependence of the CH peak and the density dependence of the OH peak, correlate. It can only be said that generally a low CH peak goes with a high OH peak, but as the graphs discussed above show, a clear conclusion cannot be made from these data. A detailed experimental series, with fixed procedures for the preparation of homogeneous pectin solutions and gels will be needed to attend to this question.
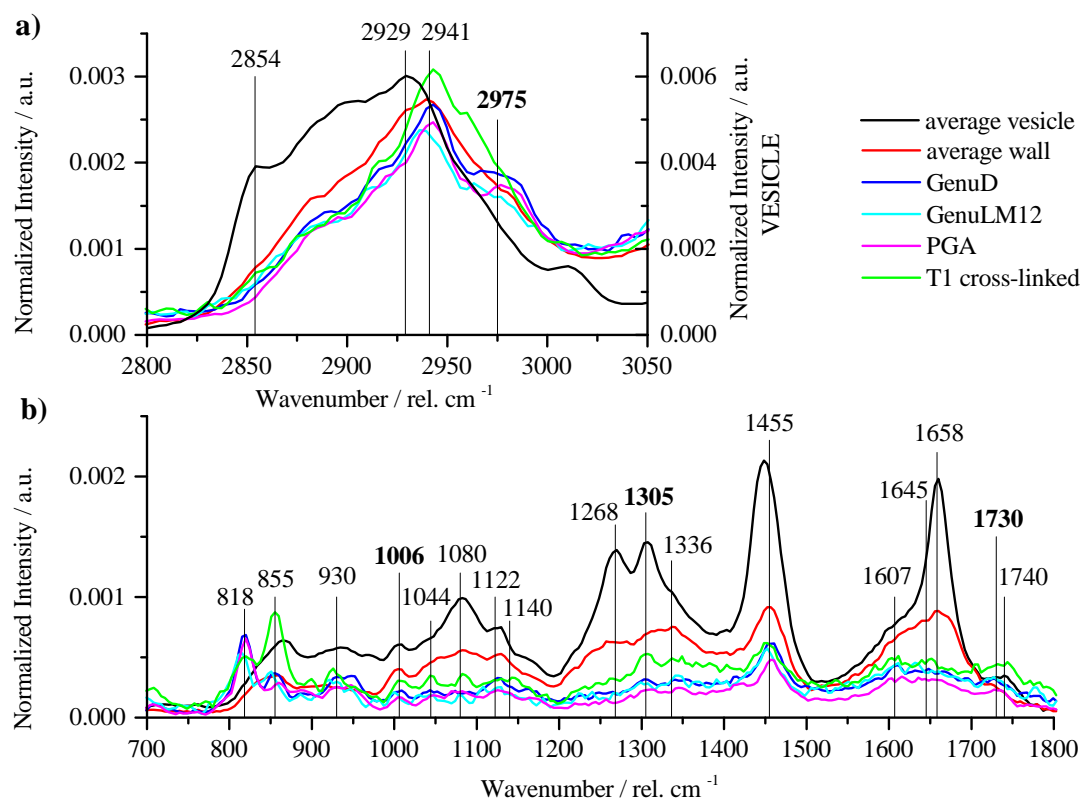
Figure 3.17: Comparison of the average spectra of the pollen wall, pollen vesicle, selected pectin solutions and a cross-linked cluster. **a)** CH stretching vibrations, spectral region from 2800 - 3050 cm^{-1}; the vesicle peak has its own scale on the right side. **b)** Spectral region from 700 - 1800 cm^{-1}. The peaks marked in bold are not seen or mentioned in the references [25, 57]. The legend on the right side is valid for both plots.

Finally, the peaks found in all the sample groups are compared in Fig. 3.17. For this purpose a set of spectra was selected for easier visualization. Since the calcium assays have quite similar shapes, only the T1 cross-linked spectrum was used for the overall comparison. From the pectin solution samples polygalacutronic acid was used as a comparison for the backbone peaks. GenuD (DE = 65 %) and GenuLM12 (DE = 34 %) were chosen to represent an LMP and an HMP, respectively. The salt forms were omitted in this case, because no significant differences were found.

Figure 3.17a shows the CH stretching peak of the representative samples of each group. Please note that the vesicle peak (black curve) is on a different scale than the other peaks (about double intensity). It can be seen that the vesicle peak is quite different from the other samples, not only in terms of scale, but also in terms of shape. A peak not found in literature is seen prevalently in the extracted pectin samples at 2975 cm^{-1}. This peak is recognizable as a mild shoulder in the pollen wall spectrum, and not at all in the vesicle spectrum. Additionally, the PCA of the pollen spectra did not indicate this peak as belonging to the first component, thus the reason for the appearance of this peak remains unclear. The general CH peak is located at about 2941 cm^{-1} for all the extracted pectins and the pollen wall spectrum, minor deviations being caused by the calibration. The same peak in the vesicle is clearly shifted to about 2929 cm^{-1}. Also, the vesicle peak shows the symmetric methyl-ester CH stretching at about 2854 cm^{-1}, which the other samples barely do.

In figure 3.17b the same spectra are plotted in the range of 700 to 1800 cm^{-1}. The cross-linked T1 sample and the pollen vesicle spectrum both display the methyl-ester C=O stretch at $\sim$ 1745 cm^{-1}, while the cell wall spectrum displays only a weak shoulder at 1725 cm^{-1} and in all the other extracted pectin samples the peak appears at about 1730 cm^{-1}. There is no record of the latter peak in the literature, but it could be argued that the presence of water shifts the peak to a lower wavenumber. The most cross-linked area in experiment T1 and the vesicles have in common that less water molecules interact with the backbone of the pectic molecule, which might be a reason for the presence of the methyl-ester C=O stretch in both samples. The vesicles contain very little water in total, and the hydrophobic areas, formed by the interactions of the methyl groups, do not allow for H-bonding between the carbonyl oxygens and the water molecules. In the case of a (strongly) cross-linked state, as in T1, the chains are pulled together, forming a dense meshwork that pushes out the water molecules, which therefore cannot interact with the carbonyl group to the same extent. When the network swells, as in the cell wall, or should there be more space between the individual chains, as in the solutions, more H-bonding to the carbonyl groups can occur and this in turn could be the reason of the presence of the peak at 1730 cm^{-1}.

The next, very prominent peak in the pollen spectra is located at about 1658 cm^{-1}. It is about 2x more intense in the wall, and 4x more intense in the vesicle spectrum than in the extracted pectins, where it is additionally shifted to about 1645 cm^{-1}. This gives a hint that this peak might come from C=C stretches of lipids forming the vesicles and the cell membrane, that is located right next to the cell wall. Neither of the two peaks is mentioned in the literature in the context of pectins. Furthermore, the extracted pectins show a peak of similar height as the previous peak at about 1607 cm^{-1}, which is assigned to the asymmetric OCO stretch by Himmelsbach et al. [25]. This peak is present in the pollen spectra, but less intense than the former, while both are more intense than in the pectin samples. The peak at 1455 cm^{-1} is present in all the samples, and again in the vesicle spectrum this band is at a smaller wavenumber of 1447 cm^{-1}. Again the intensity is about 4x higher in the vesicles and 2x higher in the wall, relative to the extracted pectins, of which PGA shows the weakest signal. This band is assigned to the asymmetric methyl-ester CH bending of pectin, but is also found in the spectrum of RGI in [25]. So it is not as specific for the methyl-ester as claimed by [57]. The general pectin CH bending is located between 1336 and 1344 cm^{-1} and present in all samples, even though just as a shoulder in the vesicle spectrum. It is covered by another peak that is present in all samples, that is at about 1305 cm^{-1} and not described in the literature. This band, as well as almost all peaks from this point to about 1000 cm^{-1}, is weakest in the extracted pectins, more intense in the calcium cross-linked spectrum, twice as intense in the pollen wall spectrum and about 4x more intense in the vesicle spectrum. The peak at 1268 cm^{-1} in the pollen spectra is not or barely present in the pectin spectra and can be seen in the arabinan spectrum in [25]. The extracted pectins rather show small peaks, probably corresponding to different general pectin peaks, but not detected by the WiTec algorithm. This hints toward the loss of arabinan residues during the extraction of pectin. At 1140 cm^{-1} (on average) a signal specific for calcium pectate [25] is visible in the T1 spectrum. It can be recognized that in the pollen wall spectrum, there is a shoulder at this position compared to the pollen vesicle spectrum, indicating the cross-linked state of the wall.

Between 1000 and 1100 cm^{-1} all the peaks are present in both, extracted and native pectin spectra. They are visible in the spectra of [25] and/or mentioned in [57] and correspond to general pectin peaks. This is true for all peaks, except the one at 1006 cm^{-1}, which is not mentioned in the literature, but clearly present in all samples. All the spectra show a peak at about 930 cm^{-1}, which belong either to side chains like arabinan or methyl-bending vibrations according to [25] and [57], although the exact position varies by about 10 cm^{-1} between the cross-linked pectin, pectin and pollen samples. Note that the intensity is about the same for all samples, except for the pollen vesicle spectrum.

The analysis of the position of the skeletal vibration at about 855 cm^{-1} of the extracted pectins in figure 3.11 (67) showed that the samples with a degree of methoxylation below 50 % tended to have a lower wavenumber. This supports the findings in the pollen tubes, where the peak position is at 851 cm^{-1} in the wall and at up to 864 cm^{-1} in the vesicles. Note also, that interestingly the cross-linked pectin peak is most intense of all the spectra. Finally the ISTD peak can be seen only in the pectin samples, at 818 cm^{-1}.

As an overview, table 3.2 shows the average peak position summary of all the types of pectin measured in this thesis: pollen vesicle, pollen wall, cross-linked pectin and pectin solutions. The rows marked in bold show the most prominent intensity changes.

Summarizing, it can be said that the spectra of the different samples showed quite a high variation in terms of overall shape of the spectrum, regardless of the source. Nevertheless, the intensity of the C-H and O-H stretching peaks seem to be indicative for the density and/or swelling of pectin, as well as have some relation to the cross-linked state, although not in a quantitative way in this experimental series. Most peaks referenced in literature could be identified and additionally four peaks appeared in (all) the spectra, which were not seen in the references [25, 57] - at 2975, 1730, 1304 and 1006 cm^{-1}. Their assignment and behavior remain to be clarified. Furthermore, the comparison of native and extracted pectins showed some peak shifts in the 'fingerprint' region of the spectrum, as well as strong intensity differences - also in the case of the calcium cross-linking of extracted pectins. The spectral variability might also be caused by the relatively high resolution of the confocal measurement setup (lateral R = 0.4 μm), due to which local variations in the micro-structure of the chains might be visible. Last but not least, also the calibration of the measurement setup should be taken into account for the minor variation of peak positions.

The spectra of the extracted pectins did not elucidate much about the local changes of pectin in the lily pollen tube, because no significant differences were found. Nevertheless, as such, this works shall serve as a preliminary study for the assertion of the limitations and problems encountered upon preparation of pectin solutions and pectin gels, as well as the recording of Raman spectra thereof in the hydrated state. This study also shows a possible measurement setup for the recording of Raman images of lily pollen tubes, and proves that it is indeed possible to discern pectin peaks within the spectra of the latter. Last but not least, this study shows a possible processing pathway of the recorded images and spectra, in order to reduce the massive amount of data to just a few spectra that are representative for each sample group and allow their comparison.

Table 3.2: Comparison of all the peaks found in pollen and pectin samples. Sh stands for shoulder. The rows marked in bold show the strongest intensity increase from the extracted pectins to the pollen samples.

Pollen wall peaks /cm^{-1}	Pollen vesicle peaks /cm^{-1}	Pectin peaks /cm^{-1}	Ca-pectin peaks /cm^{-1}
–	3070	–	–
–	3012	–	–
sh	**–**	**2975**	**2975**
2939	2929	2940	2943
–	2896	2885	2891
–	2854	–	–
–	1740	–	–
1725 sh	–	1726	1729
1659	**1657**	**1638**	**1645**
sh	sh	1609	1607
1453	**1447**	**1455**	**1454**
1415	–	–	–
1331	sh	1347	1334
sh	**1303**	**1306**	**1304**
1268	1268	–	–
–	–	1124	1138
1122	**1122**	**1124**	**1127**
1080	**1082**	**1081**	**1080**
sh	**sh**	**1044**	**1044**
1003	**1007**	**1005**	**1006**
–	**932**	**936**	**925**
851	864	853	854
–	–	817	818

Chapter 4 – Conclusion

The confocal Raman spectrometer proved to be a tool enabling the investigation of the microscopic cell wall of lily pollen tubes in a non-destructive way, without labeling and laborious sample preparation. The principal spectral features of pectin could be identified in the pollen tubes, as well as in different types of extracted pectins in the solution and cross-linked states.

The germination process was successfully initated, as well as stopped for imaging. With the part of the focus set on detecting pectin during the - aborted - growth process, not only the pectic cell wall, but also vesicles transporting pectin could be successfully identified using K-means clustering. The spectra of the different compartments primarily revealed a big difference in water content, being very low inside of the vesicles and comparatively high in the cell wall. Also, the vesicles showed a much higher intensity in most parts of the spectrum. Several peaks showed shifted positions when the wall and the vesicles, but also the tip and the shaft were compared. The principal component analysis that was performed on the whole image showed that even this basic exploratory analysis method can distinguish between different compartments of the pollen tube and investigation of the loadings could reveal specific combinations of peaks that describe them. The loadings of the first principal component, that was calculated for the wall and vesicle clusters separately, allowed the identification of a few peaks that are specific for the respective compartment, especially in the C-H stretching region. Using different programs, more advanced multivariate methods could potentially reveal more significant results, such as performing cross-validation after the PCA in order to determine the predictive power of the analysis and the number of significant principal components.

The next important part of this work was the preparation and measurement of different extracted pectins. The sample preparation was surprisingly challenging and inhomogeneity excluded the evaluation of the different concentrations. Further experiments should be attempted with a higher pH to achieve homogeneous solutions and thus meaningful concentrations. The designed measurement cell was a good container for the extracted pectin samples, as it successfully inhibited evaporation of water, and thus allowed measurement in the hydrated state. Here, k-means clustering was used for the filtering of the data to exclude unusable spectra, and clean average spectra could be generated from each sample. Unexpectedly, no major differences could be found between the different extracted pectins, although the range of degrees of methoxylation was quite high and even salt forms were used. The preparation procedures were calcium was applied to the solutions to achieve a gel were very different, and did not lead to proper gel formation. Nevertheless, these samples revealed

interesting changes in the spectra, which should also be investigated further using a better sample preparation procedure. There is potential for the preparation of calibration series in both, the pectin solutions - regarding spectral changes upon variation of the concentration - but also in the variation of the degree of cross-linking by variation of the calcium concentration and perhaps the substance used for that purpose, other than $CaCl_2$.

Finally, it is an easy thing to generate a big amount of data, but how to process them is another thing. The challenge of how to correct the background with the available software so that the spectrum is least distorted was overcome by two simple tests, one of them involving an unusual application of principal component analysis. The "right" polynomial was determined, but the selection of the spectral regions to include in the approximation could not be automated, which arguably should be the case in the future. All the spectra were re-calibrated using the WiTec software, in order to compensate for variations in the calibration of the spectrometer. Furthermore, normalization was performed to compensate different measurement conditions between pollen and extracted pectins, as well as noise reduction using PCA. K-means cluster analysis proved useful in both data sets for the partitioning of the data points - into cell compartments in the case of the pollen tubes and into usable and not usable data points in the case of the extracted pectins. This analysis chain can serve as an example of how such an analysis could be performed in a basic way, but it would be interesting to use more advanced chemometric methods in order to model i.e. the methoxylation patterns in the cell wall of the pollen tubes using well prepared calibration series of extracted pectins.

Bibliography

[1] Abdi, H. and L. J. Williams (2010). Principal component analysis. *Wiley Interdisciplinary Reviews: Computational Statistics 2*(4), 433–459.

[2] Atkins, P. W. and J. d. Paula (op. 2006). *Physical chemistry* (8th ed., 1st print. ed.). Oxford: Oxford University Press.

[3] Bonnier, F. and H. J. Byrne (2012). Understanding the molecular information contained in principal component analysis of vibrational spectra of biological systems. *The Analyst 137*(2), 322–332.

[4] Bosch, M. and P. K. Hepler (2005). Pectin methylesterases and pectin dynamics in pollen tubes: Current perspective essay. *The Plant Cell 17*(12), 3219–3226.

[5] Brereton, R. G. (2003). *Chemometrics: Data Analysis for the Laboratory and Chemical Plant: Data Analysis for the Laboratory and Chemical Plant* (1 ed.). Chichester: John Wiley Sons.

[6] Brooker, M. H., G. Hancock, B. C. Rice, and J. Shapter (1989). Raman frequency and intensity studies of liquid h2o, h218o and d2o. *Journal of Raman Spectroscopy 20*(10), 683–694.

[7] Campbell, N. A. and J. B. Reece (2008). *Biology* (8th ed ed.). Pearson Education, Inc.

[8] Cao, A., A. K. Pandya, G. K. Serhatkulu, R. E. Weber, H. Dai, J. S. Thakur, V. M. Naik, R. Naik, G. W. Auner, R. Rabah, and D. C. Freeman (2007). A robust method for automated background subtraction of tissue fluorescence. *Journal of Raman Spectroscopy 38*(9), 1199–1205.

[9] Capel, F., T. Nicolai, D. Durand, P. Boulenguer, and V. Langendorff (2006). Calcium and acid induced gelation of (amidated) low methoxyl pectin. *Food Hydrocolloids 20*(6), 901–907.

[10] Cardoso, S. M., M. A. Coimbra, and Lopes da Silva, J.A. (2003). Temperature dependence of the formation and melting of pectin–ca2+ networks: a rheological study. *Food Hydrocolloids 17*(6), 801–807.

[11] Chung, J. and Z. Zhang (2003). Mechanical characterisation of calcium pectinate hydrogel for controlled drug delivery. *Chem. Ind. 57*(12), 611–616.

[12] Conn, P. M. (©2010). *Techniques in confocal microscopy*. Reliable lab solutions. Amsterdam and Boston: Academic/Elsevier.

[13] Dallas, G. Principal component analysis 4 dummies: Eigenvectors, eigenvalues and dimension reduction.

[14] Dieing, T., O. Hollricher, and J. Toporski (2010). *Confocal Raman microscopy*, Volume 158 of *Springer series in optical sciences*. Heidelberg [Germany], New York: Springer.

[15] Esmonde-White, Francis W L, K. A. Esmonde-White, and M. D. Morris (2011). Minor distortions with major consequences: correcting distortions in imaging spectrographs. *Applied spectroscopy 65*(1), 85–98.

[16] Fayant, P., O. Girlanda, Y. Chebli, C.-E. Aubin, I. Villemure, and A. Geitmann (2010). Finite element model of polar growth in pollen tubes. *The Plant Cell 22*(8), 2579–2593.

[17] Fraeye, I., E. Doungla, T. Duvetter, P. Moldenaers, A. van Loey, and M. Hendrickx (2009). Influence of intrinsic and extrinsic factors on rheology of pectin–calcium gels. *Food Hydrocolloids 23*(8), 2069–2077.

[18] Gelder, J. d., K. d. Gussem, P. Vandenabeele, and L. Moens (2007). Reference database of raman spectra of biological molecules. *Journal of Raman Spectroscopy 38*(9), 1133–1147.

[19] Gierlinger, N., T. Keplinger, and M. Harrington (2012). Imaging of plant cell walls by confocal raman microscopy. *Nature protocols 7*(9), 1694–1708.

[20] Gierlinger, N., L. Sapei, and O. Paris (2008). Insights into the chemical composition of equisetum hyemale by high resolution raman imaging. *Planta 227*(5), 969–980.

[21] Gierlinger, N. and M. Schwanninger (2006). Chemical imaging of poplar wood cell walls by confocal raman microscopy. *PLANT PHYSIOLOGY 140*(4), 1246–1254.

[22] Harholt, J., A. Suttangkakul, and H. Vibe Scheller (2010). Biosynthesis of pectin. *PLANT PHYSIOLOGY 153*(2), 384–395.

[23] Hastie, T., R. Tibshirani, and J. H. Friedman (2008 // ©2009). *The elements of statistical learning: Data mining, inference, and prediction* (Second edition, corrected 7th printing ed.). Springer series in statistics. New York: Springer.

[24] Hill, A. E., B. Shachar-Hill, J. N. Skepper, J. Powell, and Y. Shachar-Hill (2012). An osmotic model of the growing pollen tube. *PloS one 7*(5), e36585.

[25] Himmelsbach, D., S. Khahili, and D. Akin (1999). Near-infrared–fourier-transform–raman microspectroscopic imaging of flax stems. *Vibrational Spectroscopy 19*(2), 361–367.

[26] http://passel.unl.edu/Image/siteImages/GrowingPollenTube LG.jpg.

[27] Jarvis, M. C. (2011). Plant cell walls: Supramolecular assemblies. *Food Hydrocolloids 25*(2), 257–262.

[28] Jarvis, M. C. and M. C. McCann (2000). Macromolecular biophysics of the plant cell wall: Concepts and methodology. *Plant Physiology and Biochemistry 38*(1-2), 1–13.

[29] Labbé, N. (2007). Extracting information from spectral data: Swst, advanced analytical tools for the wood industry.

[30] Larkin, P. (2011). *IR and raman spectroscopy: Principles and spectral interpretation*. Oxford: Elsevier.

[31] Lin, T.-P., T.-Y. Feng, Y.-H. Chung, and C.-L. Lan (1990). Quantification of methyl ester content of pectin by pectinesterase. *Bot. Bull. Academia Sinica 31*, 273–278.

[32] Löfgren, C., S. Guillotin, H. Evenbratt, H. Schols, and A.-M. Hermansson (2005). Effects of calcium, ph, and blockiness on kinetic rheological behavior and microstructure of hm pectin gels. *Biomacromolecules 6*(2), 646–652.

[33] MacDougall, A. J., G. M. Brett, V. J. Moris, N. M. Rigby, M. J. Ridout, and S. G. Ring ((2001)). The effect of peptide–pectin interactions on the gelation behaviour of a plant cell wall pectin. *Carbohydrate Research* (335), 115–126.

[34] McCarry, P. (January 2011). *Investigation into the production of calcium pectinate particles for oral delivery to the colon*. Ph. D. thesis, The University of Birmingham, Birmingham.

[35] McKenna, S. T., J. G. Kunkel, M. Bosch, C. M. Rounds, L. Vidali, L. J. Winship, and P. K. Hepler (2009). Exocytosis precedes and predicts the increase in growth in oscillating pollen tubes. *The Plant Cell 21*(10), 3026–3040.

[36] Mollet, J.-C., C. Leroux, F. Dardelle, and A. Lehner (2013). Cell wall composition, biosynthesis and remodeling during pollen tube growth. *Plants 2*(1), 107–147.

[37] Morell, S. and K. P. Link (1933). The methylglycosides of the naturally occurring hexuronic acids: I. the preparation of methyl-d-galacturonide. *J. Biol. Chem.* (100), 385–396.

[38] Munarin, F., M. C. Tanzi, and P. Petrini (2012). Advances in biomedical applications of pectin gels. *International journal of biological macromolecules 51*(4), 681–689.

[39] Ngouémazong, D. E., R. P. Jolie, R. Cardinaels, I. Fraeye, A. van Loey, P. Moldenaers, and M. Hendrickx (2012). Stiffness of ca(2+)-pectin gels: combined effects of degree and pattern of methylesterification for various ca(2+) concentrations. *Carbohydrate Research 348*, 69–76.

[40] Ngouémazong, D. E., N. F. Nkemamin, R. Cardinaels, R. P. Jolie, I. Fraeye, A. M. van Loey, P. Moldenaers, and M. E. Hendrickx (2012). Rheological properties of ca2+-gels of partially methylesterified polygalacturonic acid: Effect of "mixed" patterns of methylesterification. *Carbohydrate Polymers 88*(1), 37–45.

[41] Pawley, J. B. (2006). *Handbook of biological confocal microscopy: Chapter 1: Foundations of Confocal Scanned Imaging in Light Microscopy* (3 ed.). New York, NY: Springer.

[42] Perera, P. N., M. Schmidt, P. J. Schuck, and P. D. Adams (2011). Blind image analysis for the compositional and structural characterization of plant cell walls. *Analytica Chimica Acta 702*(2), 172–177.

[43] Richter, S., J. Müssig, and N. Gierlinger (2011). Functional plant cell wall design revealed by the raman imaging approach. *Planta 233*(4), 763–772.

[44] Rojas, E. R., S. Hotton, and J. Dumais (2011). Chemically mediated mechanical expansion of the pollen tube cell wall. *Biophysical Journal 101*(8), 1844–1853.

[45] Rottenfusser, R., E. Wilson, and M. W. Davidson. Numerical aperture and resolution.

[46] Schiøtt, M., S. M. Romanowsky, L. Baekgaard, M. K. Jakobsen, M. G. Palmgren, and J. F. Harper (2004). A plant plasma membrane ca2+ pump is required for normal pollen tube growth and fertilization. *Proceedings of the National Academy of Sciences of the United States of America 101*(25), 9502–9507.

[47] Schulte, F., U. Panne, and J. Kneipp (2010). Molecular changes during pollen germination can be monitored by raman microspectroscopy. *Journal of biophotonics 3*(8-9), 542–547.

[48] Séné, C., M. C. McCann, R. H. Wilson, and R. Grinter (1994). Frourier-transform raman and fourier-transform infrared spectroscopy: An investigation of five higher plant cell walls and their components. *PLANT PHYSIOLOGY 106*(4), 1623–1631.

[49] Seymour, G. B. and J. P. Knox (Eds.) (2002). *Pectins and their manipulation*. Sheffield biological sciences. Oxford and Boca Raton, FL: Blackwell and Published in U.S. and Canada only by CRC Press.

[50] Shimanouchi, T. (1977). Tables of molecular vibrational frequencies: Consolidated volume ii. *J. Phys. Chem. Ref. Data 6*(3), 993–1102.

[51] Shodor Education Foundation, Inc. Forensic science workshop: Vibrational frequencies of ethylene.

[52] Smilauer, P. and J. Leps (2013). *Multivariate Analysis of Ecological Data using Canoco 5*.

[53] Smith, E. and G. Dent (2005). *Modern Raman spectroscopy: A practical approach*. Hoboken, NJ: J. Wiley.

[54] Stoddart, R. W., I. P. Spires, and K. F. Tipton (1969). Solution properties of polygalacturonic acid. *The Biochemical journal 114*(4), 863–870.

[55] Ström, A., P. Ribelles, L. Lundin, I. Norton, E. R. Morris, and Williams, Martin A K (2007). Influence of pectin fine structure on the mechanical properties of calcium-pectin and acid-pectin gels. *Biomacromolecules 8*(9), 2668–2674.

[56] Sundar Raj, A. A., S. Rubila, R. Jayabalan, and T. V. Ranganathan (2012). A review on pectin: Chemistry due to general properties of pectin and its pharmaceutical uses. *Open Access Scientific Reports 1*(12).

[57] Synytsya, A., J. Copíková, P. Matejka, and V. Machovic (2003). Fourier transform raman and infrared spectroscopy of pectins. *Carbohydrate Polymers 54*(1), 97–106.

[58] Taylor, R. L. and H. E. Conrad (1972). Stoichiometric depolymerization of polyuronides and glycosaminoglycuronans to monosaccharides following reduction of their carbodiimide-activated carboxyl group. *Biochemistry 11*(8), 1383–1388.

[59] Thygesen, L. G., M. M. Løkke, E. Micklander, and S. B. Engelsen (2003). Vibrational microspectroscopy of food. raman vs. ft-ir. *Trends in Food Science & Technology 14*(1-2), 50–57.

[60] Tibbits, C. W., A. J. MacDougall, and S. G. Ring (1998). Calcium binding and swelling behaviour of a high methoxyl pectin gel. *Carbohydrate Research* (310), 101–107.

[61] Tukhvatullin, F. H., A. Jumaboev, U. N. Tashkenbaev, A. Tursunkulov, and A. Shaymanov (1998). The shape and width of the 818 cm-1 raman band of propan-2-ol in solutions. *Journal of Raman Spectroscopy 29*(12), 1027–1029.

[62] Turrell, G. and J. Corset (©1996). *Raman microscopy: Developments and applications*. London and San Diego: Academic Press.

[63] Winning, H., N. Viereck, L. Nørgaard, J. Larsen, and S. B. Engelsen (2007). Quantification of the degree of blockiness in pectins using 1h nmr spectroscopy and chemometrics. *Food Hydrocolloids 21*(2), 256–266.

[64] Winning, H., N. Viereck, T. Salomonsen, J. Larsen, and S. B. Engelsen (2009). Quantification of blockiness in pectins-a comparative study using vibrational spectroscopy and chemometrics. *Carbohydrate Research 344*(14), 1833–1841.

[65] Winship, L. J., G. Obermeyer, A. Geitmann, and P. K. Hepler (2010). Under pressure, cell walls set the pace. *Trends in plant science 15*(7), 363–369.

[66] Winship, L. J., G. Obermeyer, A. Geitmann, and P. K. Hepler (2011). Pollen tubes and the physical world. *Trends in plant science 16*(7), 353–355.

[67] Witec GmbH. Confocal raman configuration.

[68] Witec GmbH (2014). Project four plus: Help file.

[69] Yapo, B. M. and K. L. Koffi (2013). Utilisation of model pectins reveals the effect of demethylated block size frequency on calcium gel formation. *Carbohydrate Polymers 92*(1), 1–10.